BENEMÉRITA UNIVERSIDAD AUTÓNOMA DE PUEBLA

INSTITUTO DE FÍSICA “LUIS RIVERA TERRAZAS”

“TRANSPORT PROPERTIES IN LÉVY-TYPE DISORDERED STRUCTURES”

TESIS

QUE PARA OBTENER EL GRADO DE

MAESTRO EN CIENCIAS (FÍSICA)

PRESENTA:

LUIS ALBERTO RAZO LÓPEZ

ASESOR(ES):

DR. JOSÉ ANTONIO MÉNDEZ BERMÚDEZ

DR. VÍCTOR ARTURO GOPAR SÁNCHEZ

No. de CVU: 861575

ENERO 2020

BENEMÉRITA UNIVERSIDAD AUTÓNOMA DE PUEBLA

Instituto de Física "Ing. Luis Rivera Terrazas"

Transport properties in Lévy-type disordered structures

TESIS

QUE PARA OBTENER EL GRADO DE

MAESTRO EN CIENCIAS (FÍSICA)

PRESENTA

Luis Alberto Razo López

Asesores: Dr. José Antonio Méndez Bermúdez & Dr. Víctor Arturo Gopar Sánchez

Invierno 2020

Transport properties in Lévy-type disordered structures

Tesis que para obtener el grado de Maestro en Cierncias (Física)
presenta

Luis Alberto Razo López

Instituto de Física "Ing. Luis Rivera Terrazas"
Benemérica Universidad Autónoma de Puebla

A mi patria,
A mi familia,
A ellas...

Acknowledgments

Antes que nada quiero decir que vivo infinitamente en deuda con todas las personas aquí mencionadas así como con muchas otras que por motivos de memoria no estarán. De igual modo, gracias a todos. Como dice el rapero Ajax: “Esto es por los mios y por mí, pa’ que mañana sea feliz al ver mis huellas mi muy querido hijo, que mis manos se fronten en orgullo a lo que hicieron, que mi boca sonria por aquello que dijo...” Comento que si esta parte de la tesis está en español es para facilidad de expresión mía y de entendimiento vuestro.

Primero quiero agradecer a la familia Razo López. Comenzando por mi padre, Miguel Mauricio Razo Jiménez, quién siempre ha sido un profesor para mí. A mi madre, Leticia López Salas, por imprimir en mí todo el amor del mundo. A ambos, gracias por los valores morales y éticos, por el conocimiento y sobre todo por el apoyo, el amor y la cercania con la que viven cada momento. Agradezco a mis hermanos, Miguel Eduardo Razo López y Mauricio Alejandro Razo López, porque como dijo Borges, la amistad de hermanos no necesita frecuencia, solo está ahí, y ustedes saben y yo sé, que siempre hemos estado juntos. Uno no escoge a su familia, sencillamente no puede, nacemos de ellos, vivimos de ellos, con ellos y para ellos. Agradezco a ustedes por aceptarme como soy, como he sido y como seré. Agradezco que, aunque no comulguen con mis ideas, su respeto ha sido la base de mis principios más fuertes. Finalmente agradezco que es debido a todos ustedes hoy vivo enamorado de la vida.

Agradezco primero a Susana Plascencia Orozco, quién me ha acompañado muy de cerca desde hace ya algunos años. Niña, sos mi mejor amiga y espero que eso se mantenga mucho tiempo más, gracias por esas tardes de chicas pegados al teléfono. Ahora sí escribí tus apellidos. A Carlos Antonio Gómez Peralta, por el apoyo incondicional y la lucidez para interpretar mi vida y apoyarme en cada tremenda babosada que se me ha ocurrido. A Andrea Alejandra Arenales Franco, quien la vida convirtio en una de las personas más cercana a mi persona, gracias por apoyarme y aconsejarme, sabes que siempre estaré aquí para ti. Quiero agradecer también a Jesús Aldair Pantoja Gonzalez y a Jhony Ariel Herrera Mendoza por el apoyo, las burlas, los memes y las largas tardes discutiendo problemas que quizá aún no terminamos de entender. Gracias por las alitas que olian como mi pelo y las *shalshishitash* a la Honduras.

Agradezco a la familia Ramírez Ascencio, pues me brindaron mucho apoyo, comprensión y amor.

A ustedes por poner tantas esperanzas y sueños en mí, gracias. Especialmente, sabes que eres vos Sabina quién siempre vivirá en mi corazón. Gracias por haberme amado y haberme dejado amarte. Gracias por permanecer en mis recuerdos como uno de los grandes amores que he tenido y tendré en la vida. Sin ti yo no sería quien soy. Del mismo modo, este trabajo ha sido culminado gracias a Cynthia Getsemaní, chula, vos me enseñaste a amar y compartimos tantas cosas juntos que solo puedo recordarte con una sonrisa en el rostro. Como habrá notado el lector más adelantado, este parrafo está fuertemente relacionado con la dedicatoria, siendo las dos niñas antes mencionadas a las que aún fuera de mis recuerdos puedo mirar a los ojos y decirles firmemente que las amo y que siempre lo haré. Agradezco a todas las mujeres que por corto o largo tiempo han abrazado mi ser con su comprensión y amor. Quizá haya nombres que no valga la pena poner, pero ustedes saben que a mi modo, las quiero. Quiero agradecer a Shelvy Dibanhi Cáceres por haber aparecido en mi vida y darme el aliento que necesité en esos momentos duros, gracias por ser firme en tus decisiones. Finalmente y con todo el amor que mi ser puede sentir en este momento, agradezco a María José Cisneros, señorita, vos sabes y siempre sabrás lo que pienso de ti y lo mucho que te he admirado desde la primera vez que te ví, gracias por mostrarme que la luz de mi corazón no tiene límites y que aún bajo las peores adversidades ésta debe brillar con fuerza. Sabes que lograrás tus sueños y que cumplirás tus metas, sabes que siempre serás especial para mí. Y si he de agradecerte algo en particular, fue por todo el amor que cargaba tu mirada la última vez que nos vimos. Agradezco por lo que paso y por lo que no, quizá nos nos volvamos a ver jamás, tal vez siempre nos preguntemos que habría pasado si hubiesemos fluido más traquilamente o si los tiempos nos hubieran permitido correspondernos a la vez. Al menos yo me pregunto que habría pasado si mi corazón hubiese estado libre de orgullo. Una cosa es segura, mi alma sonrie cuando pienso en ti y eso jamás va a cambiar. Por cierto, extraño mucho los cuentos y poemas nocturnos. Te escribo aquí porque no puedo hacerlo por otro medio, "tal vez yo no tenga razones de peso y el aire se lleva lo que estoy diciendo"[1].

Agradezco a todos mis compañeros y amigos que a lo largo de estos 7 años de física me han acompañado. Especialmente agradezo a Javier, Samantha, Pastor, Lupe, Ándres, David, Christian, Paquito, Jordan, Misael, Irigamí, Aquacarlos, Cezar, Dayana, Yessica, Alejandra, Marilú, Diana y Osvaldo quienes estuvieron conmigo estos últimos dos años. Agradezco a Carlos, Cesar, Arturo, Rafael, Norman, Irma, Anaid, Juan Pablo, Kaleb, Esli, Rodrigo, Ilse, Nazareth, Celicia, Kevin, Zack, Silvana, Isaac, Noel, Edson, Fernando, y Benjamín por ser las personas con las que he crecido y que me han permitido aprender de ellas desde mi inicio en esto. A mis amigos personales que nada tienen que ver con la ciencia Oscar, Tico, Ezequiel, Alberto, Juan, Hagel y Tote. A la gente que jamás he visto y posiblemente jamás veré en mi patría Santiago, Daniel Martín, Daniel Sucerquia, William, David, Evelyn, Francesca, Francesco, Fabio, Mohammand, Harris, Salomon, Debasish, Mehrdad, Gabriel, Prianka, Sina, Gabriele, Christian, Charlotte, Romain, Mathis, Yanel y Amanda. Gracias y mucho exito a todos.

[1] El día que hacía más viento que nunca - Carlos Sadness

Este trabajo no habría sido posible sin mis asesores, que más que jefes, hoy veo como amigos muy cernanos. Agradezco a José Antonio Méndez Bermúdez y a Víctor Arturo Gopar Sánchez por la paciencia, el conocimiento y sobre todo por la confianza al brindarme la oportunidad de trabajar con ustedes. Agradezco cada corrección hecha a este trabajo así como a los resultados obtenidos. Agradezco también a mis amigos y anteriores asesores Thomas Gorin y Rafael Méndez. Especialmente agradezco a Víctor Domínguez quien es uno de mis amigos más cercanos, gracias por abrirme los ojos a la vida continuamente. A sí mismo, creo que debo gran parte de mi ánimo y felicidad actual a Fabrice Mortessagne, con quien espero poder desarrollar todo mi potencial en Niza. A todos ustedes, mil gracias. Así mismo, agradezco a Antonio Fernandez y a John Franco por su apoyo en este y otros trabajos. También, agradezco a los Dres. Luca Celardo, Mauricio Torres y Alfredo Díaz por las valiosas correcciones hechas a este trabajo.

Finalmente agradezco a todos los profesores que han brindado su tiempo para que el conocimiento pueda ser construido en mí. Han sido 7 años muy duros pero gracias a todos ustedes, hoy puedo asegurar que amo lo que hago. Agradezco a la Universidad de Guadalajara donde forjé la primera etapa de mi carrera. Al Instituto de Física "Luis Rivera Terrazas" y a la Benemérica Universidad Autónoma de Puebla, donde este posgrado ha sido culminado. A CONACYT por financiar los gastos correspondientes a este posgrado. Así mismo, agradezco al ICTP y en especial a Matteo Marsilli y a Andrea Gambassi por las oportunidades brindadas para visitar su centro de investigación en Italia. Agradezco a la Universidad de Zaragagoza por habarme recibido tan bien durante mi corta estancia la cual espero repetir pronto. Finalmente, agradezco de antemano a la Université Côte D'Azur donde espero terminar mi educación.

Contents

Abstract

In this work, we study (numerically, analytically and experimentally) wave transport properties in disordered media. Particularly, we are interested in systems with a disorder characterized by Lévy-type distributions. These distributions show a slow decay of their tails, thus the first and second moments may diverge.

The inevitable presence of imperfections and impurities contained in natural systems represent a source of disorder. Considering wave transport, these impurities lead to a random behavior to the scattering process, so that transmission and reflection become random quantities which accept a statistical analysis. We pay special attention to the average transmission, transmission distribution functions, and time delay distributions. Before studying Lévy-type disordered structures, we will analyze statistical properties in standard disordered systems which are characterized by distributions with well defined moments. This kind of disorder leads to the Anderson localization phenomena. Afterward, the anomalous localization problem, *i.e.* the Lévy problem, will be considered.

The main goal of this thesis work is to understand the behavior of delay times in Levy-type disordered structures. The importance of this quantity is that it measures how long a wave takes inside a given system. It was defined by Wigner as the derivative of the phase shift respect to the energy after a wave has interacted with a target system. Despite the large number of works about delay times in standard disordered systems, this problem remains unsolved in some aspects. Also, we do not know any work which considers this quantity in Lévy structures. Specifically, a theoretical characterization of delay times is contrasted against numerical simulations. Finally, a comparison between both results and experimental measurements is performed.

Resumen

En este trabajo estudiamos de forma numérica, analítica y experimental las propiedades de transporte en sistemas desordenados. Particularmente estamos interesados en estructuras cuyo desorden se caracteriza por distribuciones de tipo Lévy. Estas distribuciones muestran un decaimiento lento en sus colas por lo que su primer y segundo momento pueden diverger.

La presencia de imperfecciones e impurezas contenidas en los sistemas físicos reales representa una inevitable fuente de desorden. Hablando de transporte ondulatorio, estas impurezas producen un comportamiento aleatorio del proceso de dispersión, lo que convierte a cantidades como la transmisión y la reflexión en cantidades aleatorias. Esto genera que tengamos que recurrir a un enfoque estadístico para el correcto análisis de estos problemas. En este trabajo prestamos especial atención a cantidades como el promedio de la transmisión, funciones de distribución de la transmisión y funciones de distribución del tiempo de retardo. Antes de estudiar las estructuras con desorden de Lévy, analizaremos las propiedades estadísticas de sistemas con desorden estándar, *i.e.* desorden generado por funciones de distribución con momentos bien definidos. Este tipo de desorden genera el fenómeno de localización de Anderson. Posteriormente, el problema de localización anómala, *i.e.* el problema de Lévy, será presentado.

El principal objetivo de este trabajo de tesis es entender el comportamiento del llamado tiempo de retardo en sistemas desordenados de tipo Lévy. La importancia de esta cantidad yace en que ésta mide cuanto tiempo permanece una onda dentro de algún sistema. Ésta fue definida por Wigner como la derivada del cambio de fase con respecto a la energía después de la interacción de una onda con un blanco determinado. A pesar del gran número de trabajos referentes al tiempo de retardo en estructuras con desorden estándar, este problema aún permanece abierto en ciertos aspectos. Además, no tenemos conocimiento de algún trabajo que considere el tiempo de retardo en alambres desordenados con desorden de Lévy. Específicamente, la caracterización teórica de los tiempos de retardo es contrastada con simulaciones numéricas. Posteriormente, una comparación entre ambos resultados y uno experimental es llevada a cabo.

I

Introduction

What if my dreams don't become reality?
Is my life just a big mistake?
Will I be happy for the times I had?
Would I reconsider recalculate?
In Flames (Wallflower)

Wave transport through disordered media is a fundamental topic in physics and has been widely investigated. Given the generality of this phenomenon, classical or quantum waves can be treated similarly. Particularly, one of the most studied problems is the Anderson localization [1, 2, 3], which is characterized by a strong, *i.e.* exponential, spatial localization of waves. This phenomenon is triggered by the destructive interference of the waves inside a disordered system.

On the other hand, it is known that some one-dimensional disordered systems may present another kind of localization different than Anderson localization. It has been shown that the use of stable distributions to induce disorder produces wave localization different than Anderson localization [4, 5, 6, 7, 8, 9, 10]. This special case of localization is known as *anomalous localization*.

Stable distributions, also known as Lévy distributions, are characterized by a slow decay [11]. Specifically, if we choose x as a Lévy random variable, it is known that its distribution function has the form $p(x) \sim 1/x^{\alpha+1}$ for $x \gg 1$ and $0 < \alpha < 2$. Here, α is named the stable parameter and determines the decay of the distribution. Also, the first statistical moment diverges in all the α-domain while the second moment diverges for $\alpha < 1$. Those distributions have been used to explain diverse phenomena in biology [12] and economy [13], among other fields.

The first experimental observation of anomalous localization in Lévy disordered systems was performed by Barthelemy *et al.* [4] using photonic structures named *Lévy glasses*. Motivated by this experiment, a theory to mathematically explain the transport phenomena through one-dimensional Lévy disordered systems was developed considering electrons [6] and, later, using classical electromagnetic waves [8]. Finally, a photonic waveguide was constructed using dielectric scatterers placed according to a Lévy distribution [10]. That experiment proved the previous results about the transmission coefficient distribution but other important quantities, like delay times, have not been studied yet.

The concept of delay times was proposed by Wigner [14] and they measure how long a wave takes to be reflected by a scatterer to come back to its starting point. It other words, the delay time τ measures how much time a wave spends inside a system. Mathematically, it is defined as the derivative of the phase shift η respect to the energy E

$$\tau \propto \frac{\mathrm{d}\eta}{\mathrm{d}E}.$$

Nowadays, delay times in disordered media have been extensively investigated considering Anderson localization [15, 16, 17, 18, 19]. However, some questions about this problem remain unsolved. It is important to stress that we do not know about studies that consider delay times in Lévy disordered structures. Motivated by this, we propose to investigate, theoretically and numerically, delay times in this kind of systems. These results will be contrasted with experimental measurements.

The main goal of this thesis is to study the statistical properties of wave transport in disordered media. Specifically, we are interested in delay times through Lévy-structures. Thus, the following specific objectives have been proposed.

- The study of transmission in Anderson disordered structures.
- The study of delay times in Anderson disordered structures.
- The study of transmission in Lévy-type disordered structures.
- The study of delay times in Lévy-type disordered structures.
- The comparison between the theoretical and numerical results with the corresponding experimental data.

This work is organized as follows. Chapter 1 presents the two main ingredients of our numerical simulations: a physical model based on electrodynamics and the mathematical formalism of the transfer and scattering matrices. Additionally, Fabry-Perot resonances, photonic crystals, as well as the time delay, will be presented and briefly discussed. In Chapter 2, the general ideas about Anderson localization will be shown. First, the one-parameter scaling theory and transmission distributions are presented. Then, we will focus on the delay time problem. The main result of this chapter is a new approximated distribution for delay times in finite systems.

The anomalous localization problem, or Lévy problem, will be analyzed in Chapter 3. As an introduction, some details about stable distributions will be presented and then, we will use them to construct Lévy-disordered structures. The properties of the transmission coefficient will be studied later. Finally, delay times in this kind of systems will be analyzed. The analysis of delay times will open a discussion about the homogeneity of the disorder inside the system which will result in two different kinds of structures characterized by Lévy disorder. In the final Chapter, experimental results will be compared with the theoretical results presented in Chapters 2 and 3. Finally, the conclusions of this work and future prospectives will be discussed.

As a complement of this Thesis, Appendix A will present some results on Anderson structures with absorption. In Appendix B, numerical results for the ballistic regime using standard disorder are shown. Appendix C contains a set of complementary figures.

1

Basic concepts

Fear leads to anger,
anger leads to hate,
hate leads to suffering.
Master Yoda to Anakin
(Star Wars Episode I: The Phantom Menace)

Abstract

In this chapter, we present the two principal ingredients of our numerical model which are the transfer matrix method and the photonic model. Specifically, the transfer matrix method is applied to obtain the transport quantities from an electromagnetic model. Finally, a brief introduction of the time delay is shown.

Transfer and scattering matrices

One of the most popular mathematical treatments to work with any wave transport process is the *transfer matrix method* which is closely related to the *scattering matrix method*. To explain how this method works, we consider a one-dimensional system[1] with a potential $V(x)$ in the region $x_a < x < x_b$. Notice that this potential can represent a change of medium in the electromagnetic case. For a wave function ψ, the transfer matrix relates the left-hand amplitudes with the right-hand amplitudes. The scattering matrix allows expressing the coefficients of the waves coming from the potential in terms of the coefficients of the waves that enter in the potential. We write

$$\psi_L = \psi_L^+ + \psi_L^-, \qquad \psi_R = \psi_R^+ + \psi_R^-, \tag{1.1}$$

where the subscripts L and R refer to the left and right side of the potential, respectively. Likewise, the superscripts $+$ and $-$ label the direction of the wave. A diagram of this process is shown in figure 1.1.

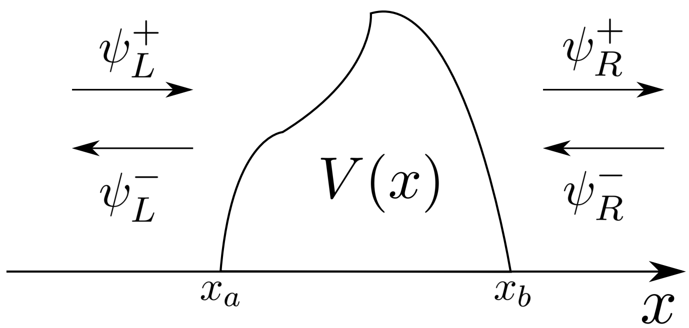

Figure 1.1: Diagram of a one-dimensional scattering system. The arrows show how the waves are moving with respect to the potential $V(x)$.

It can be seen that for two or more potentials, the associated final matrix can be computed by multiplying the corresponding transfer matrices of each potential. Since we are considering one-dimensional systems, the scattering and transfer matrices are 2×2 matrices. For the transfer matrix $\mathbf{M}$ we write

$$\begin{pmatrix} \psi_R^+ \\ \psi_R^- \end{pmatrix} = \begin{pmatrix} M_{11} & M_{12} \\ M_{21} & M_{22} \end{pmatrix} \begin{pmatrix} \psi_L^+ \\ \psi_L^- \end{pmatrix},$$

while the scattering matrix $\mathbf{S}$ has the form

$$\begin{pmatrix} \psi_L^- \\ \psi_R^+ \end{pmatrix} = \begin{pmatrix} S_{11} & S_{12} \\ S_{21} & S_{22} \end{pmatrix} \begin{pmatrix} \psi_L^+ \\ \psi_R^- \end{pmatrix}. \tag{1.2}$$

Additionally, the elements of the $\mathbf{M}$ and $\mathbf{S}$ matrices are related as follows

$$\mathbf{M} = \begin{pmatrix} \frac{S_{21}S_{12}-S_{11}S_{22}}{S_{12}} & \frac{S_{22}}{S_{12}} \\ -\frac{S_{11}}{S_{12}} & \frac{1}{S_{12}} \end{pmatrix}, \qquad \mathbf{S} = \begin{pmatrix} -\frac{M_{21}}{M_{22}} & \frac{1}{M_{22}} \\ \frac{M_{11}M_{22}-M_{12}M_{21}}{M_{22}} & \frac{M_{12}}{M_{22}} \end{pmatrix},$$

where the coefficients of both matrices are, in general, complex numbers.

[1]In this work, we only consider one-dimensional systems, but a generalization of these methods have been studied in [20] considering quasi-one-dimensional systems.

Transmission and reflection amplitudes

Consider an incoming wave interacting with the potential only from the right side, $\psi_L^+ = 0$, the scattering matrix (1.2) becomes

$$\psi_L^- = S_{12}\psi_R^-, \qquad\qquad \psi_R^+ = S_{22}\psi_R^-,$$

where S_{12} and S_{22} are called *transmission amplitude* t and *reflection amplitude* r, respectively. Similarly, we can choose the left side as the incident side, $\psi_R^- = 0$, to obtain the t' and r' amplitudes

$$\psi_L^- = S_{11}\psi_L^+, \qquad\qquad \psi_R^+ = S_{21}\psi_L^+,$$

so that, the scattering matrix is written as

$$\mathbf{S} = \begin{pmatrix} r' & t \\ t' & r \end{pmatrix}. \tag{1.3}$$

Moreover, the transmission and reflection amplitudes can be written in terms of the transfer matrix coefficients in the form

$$\begin{aligned} t &= \frac{1}{M_{22}}, & r &= \frac{M_{12}}{M_{22}}, \\ t' &= \frac{M_{11}M_{22} - M_{12}M_{21}}{M_{22}}, & r' &= -\frac{M_{21}}{M_{22}}, \end{aligned} \tag{1.4}$$

where both, t' and r', are related with t and r for systems where specific properties and symmetries are presented. Finally, the transmission and reflection coefficients are defined as [20]

$$T = |t|^2, \qquad \text{and} \qquad R = |r|^2,$$

as well as for the t' and r' components where we have

$$T' = \left|t'\right|^2, \qquad \text{and} \qquad R' = \left|r'\right|^2.$$

Now, some properties of these coefficients will be discussed.

Symmetries of the system

Symmetries generally reduce analytical computations and provide some powerful options to test numerical simulations in a first instance. One of the most typical symmetries is the time-reversal symmetry, which will be presented after we show the behavior of a system that conserves the current.

Conservation of the current

By multiplying the one-dimensional Schrödinger equation with solution $\psi(x)$ by $\psi^*(x)$ and integrating on the interval where the potential lies, we get

$$\mathrm{i}\hbar \int_{x_a}^{x_b} \psi^* \frac{\partial \psi}{\partial t} \mathrm{d}x = -\frac{\hbar^2}{2m} \int_{x_a}^{x_b} \psi^* \frac{\partial^2 \psi}{\partial x^2} \mathrm{d}x + \int_{x_a}^{x_b} \psi^* V(x) \psi \mathrm{d}x. \tag{1.5}$$

Then, we subtract from equation (1.5) its complex conjugate to obtain

$$\frac{\partial}{\partial t}\int_{x_a}^{x_b}\psi^*\psi \mathrm{d}x = \int_{x_a}^{x_b}\frac{\partial j(x)}{\partial x}\mathrm{d}x + \frac{1}{\mathrm{i}\hbar}\int_{x_a}^{x_b}\left[\psi^* V(x)\psi - \psi V^*(x)\psi^*\right]\mathrm{d}x\,, \tag{1.6}$$

where $j(x)$ is called the current density in the x direction and is defined as [21]

$$j(x) = \frac{\mathrm{i}\hbar}{2m}\left[\psi(x)\frac{\partial\psi^*(x)}{\partial x} - \psi^*(x)\frac{\partial\psi(x)}{\partial x}\right].$$

From equation (1.6), we can observe that if $V(x)\in\mathbb{R}$ the third integral vanishes. The general case where $V(x)\in\mathbb{C}$ corresponds to systems with absorption or gain which are presented numerically in Appendix A. Also, the first integral represents the change in charge density with respect to time for $x_a < x < x_b$. In this work we focus on systems that are independent of time, then this integral must vanish. Afterward, equation (1.6) becomes

$$\int_{x_a}^{x_b}\frac{\partial j(x)}{\partial x}\,\mathrm{d}x = j(x_b) - j(x_a) = 0, \tag{1.7}$$

which is the flux conservation condition through the scattering region. For a plane wave $\psi^\pm = A\mathrm{e}^{\pm\mathrm{i}kx}$, we have

$$j_\pm = \pm\frac{\hbar k}{2}|A|^2 = \pm\frac{\hbar k}{2}|\psi^\pm|^2.$$

By substituting this in equation (1.7) and considering $j_{L,R} = j^+_{L,R} + j^-_{L,R}$ and equation (1.1), we get

$$\begin{pmatrix}\psi_R^{+*} & \psi_L^{-*}\end{pmatrix}\begin{pmatrix}\psi_R^+\\ \psi_L^-\end{pmatrix} = \begin{pmatrix}\psi_L^{+*} & \psi_R^{-*}\end{pmatrix}\begin{pmatrix}\psi_L^+\\ \psi_R^-\end{pmatrix},$$

$$\begin{pmatrix}\psi_L^{-*} & \psi_R^{+*}\end{pmatrix}\mathbf{S} = \begin{pmatrix}\psi_L^{+*} & \psi_R^{-*}\end{pmatrix}, \qquad \text{or} \qquad \begin{pmatrix}\psi_L^{-*} & \psi_R^{+*}\end{pmatrix} = \begin{pmatrix}\psi_L^{+*} & \psi_R^{-*}\end{pmatrix}\mathbf{S}^\dagger,$$

so that

$$\mathbf{S}\mathbf{S}^\dagger = \mathbb{1},$$

where $\mathbb{1}$ is the 2×2 unitary matrix. This finally implies

$$T + R = 1 \qquad \text{and} \qquad |\det(\mathbf{S})| = 1.$$

Time-reversal symmetry

For a system with time-reversal symmetry, the wave function becomes

$$\psi(x) \to \psi^*(x),$$

which for the particular case of a planar wave corresponds to the same wave propagating in the opposite direction. In this frame, ψ_L^{-*} and ψ_R^{+*} are the incident waves, thus the expression (1.2) and its conjugate are

$$\begin{pmatrix}\psi_L^{+*}\\ \psi_R^{-*}\end{pmatrix} = \mathbf{S}\begin{pmatrix}\psi_L^{-*}\\ \psi_R^{+*}\end{pmatrix} \qquad \text{and} \qquad \begin{pmatrix}\psi_L^{-*}\\ \psi_R^{+*}\end{pmatrix} = \mathbf{S}^*\begin{pmatrix}\psi_L^{+*}\\ \psi_R^{-*}\end{pmatrix},$$

then,

$$\mathbf{S}\mathbf{S}^* = \mathbb{1},$$

which, together to the current conservation condition, allows concluding that $\mathbf{S}$ is symmetric. Hence, from equation (1.3) it can be seen that $t = t'$. Additionally, for the transfer matrix we have

$$\begin{pmatrix} 0 & 1 \\ 1 & 0 \end{pmatrix} \begin{pmatrix} \psi_R^{+*} \\ \psi_R^{-*} \end{pmatrix} = \mathbf{M} \begin{pmatrix} 0 & 1 \\ 1 & 0 \end{pmatrix} \begin{pmatrix} \psi_L^{+*} \\ \psi_L^{-*} \end{pmatrix} \qquad \text{and} \qquad \begin{pmatrix} \psi_R^{+*} \\ \psi_R^{-*} \end{pmatrix} = \mathbf{M}^* \begin{pmatrix} \psi_L^{+*} \\ \psi_L^{-*} \end{pmatrix},$$

and finally,

$$\mathbf{M} = \begin{pmatrix} M_{11} & M_{12} \\ M_{12}^* & M_{11}^* \end{pmatrix} \qquad \text{and} \qquad \det(\mathbf{M}) = 1.$$

As we can observe, the importance of these characteristics lies in they allow easily computing transport quantities for a complex system.

Note that these properties of the transfer and dispersion matrices are general and can be applied to both classical or quantum waves. For simplicity, we have used a quantum approach and some considerations, like plane waves, to show these properties, although they can be proved using different formalisms. Now, we will present another formalism which admits an easier experimental perform.

Electromagnetic model

Consider a layer of width l, permittivity ϵ_2 and permeability μ_2 which lies between two different and semi-infinite media with permittivities (ϵ_1, ϵ_3) and permeabilities (μ_1, μ_3). For simplicity, the electric field is always chosen perpendicular to the surfaces. A diagram of this process is shown in the figure 1.2.

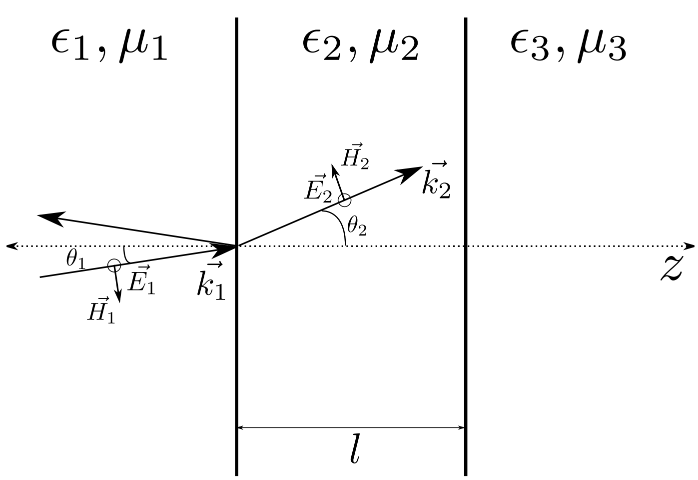

Figure 1.2: Diagram of a one-dimensional layered system. The arrows indicate the wave direction. The process will be repeated in the interface between medium 2 and medium 3.

The coefficients of the electromagnetic field in medium 3 can be written in terms of the field in medium 1. Then, the field in medium 3 is given in terms of three transfer matrices as

$$\begin{pmatrix} E_3^+ \\ E_3^- \end{pmatrix} = \mathbf{M}_{23} \begin{pmatrix} \mathrm{e}^{\mathrm{i}k_{2z}l} & 0 \\ 0 & \mathrm{e}^{-\mathrm{i}k_{2z}l} \end{pmatrix} \mathbf{M}_{12} \begin{pmatrix} E_1^+ \\ E_1^- \end{pmatrix},$$

where $\mathbf{M}_{23}$ and $\mathbf{M}_{12}$ are the transfer matrices from medium 2 to medium 3 and from medium 1 to medium 2, respectively, and k_{2z} is the wavenumber inside the layer in the z-axis. It can be observed that the second transfer matrix produces phase change for the planar wave. Also, the coefficients of the first and third transfer matrices are given by the Fresnel equations.

Transfer-matrix coefficients

According to [22], the Fresnel equations are derived from the properties of the electromagnetic field through an interface. Considering that the wave moves from medium 1 to medium 2, the equations for the electric field are

$$E' = \frac{2n_1 \cos\theta_1}{n_1 \cos\theta_1 + \frac{\mu_1}{\mu_2}\sqrt{n_2^2 - n_1^2 \sin^2\theta_1}} E \qquad \text{and} \qquad E'' = \frac{n_1 \cos\theta_1 - \frac{\mu_1}{\mu_2}\sqrt{n_2^2 - n_1^2 \sin^2\theta_1}}{n_1 \cos\theta_1 + \frac{\mu_1}{\mu_2}\sqrt{n_2^2 - n_1^2 \sin^2\theta_1}} E,$$

where E' is the reflected component and E'' is the transmitted one. In order to find all the coefficients of the transfer matrix, we consider a wave coming from medium 1 to medium 2 and another one moving from medium 2 to medium 1. Then, the other two components are in terms of the reflected and transmitted waves as it is shown in figure 1.3.

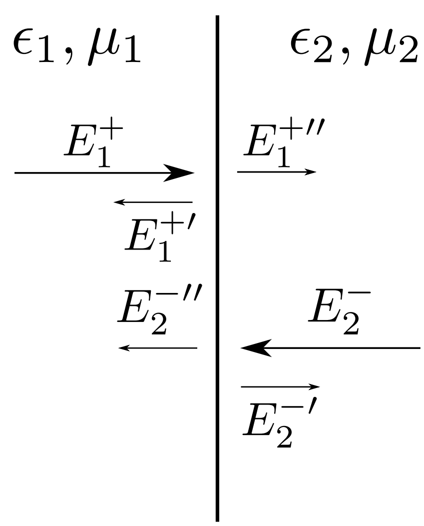

Figure 1.3: Diagram of the two main components of the electric field and their reflected and transmitted components.

This analysis allows writing

$$E_2^+ = E_1^{+\prime\prime} + E_2^{-\prime} \qquad \text{and} \qquad E_1^- = E_2^{-\prime\prime} + E_1^{+\prime}.$$

By substituting here the Fresnel equations and consider that $k_i = n_i\omega/\mathrm{c}$, the transfer matrix is given by

$$\mathbf{M}_{12} = \frac{1}{2}\begin{pmatrix} 1+z_{12} & 1-z_{12} \\ 1-z_{12} & 1+z_{12} \end{pmatrix}, \tag{1.8}$$

with $z_{12} = \mu_2 k_{1z}/\mu_1 k_{2z}$ and $k_{iz} = k_i \cos\theta_i$. Since the transfer matrix $\mathbf{M}_{23}$ is constructed in the same way, it can be obtained from (1.8) by replacing z_{12} by z_{23}. By multiplying the three transfer matrices we find

$$\begin{aligned}
M_{11} &= \frac{1}{2}(1+z_{13})\cos k_{2z}l + \frac{\mathrm{i}}{2}(z_{12}+z_{23})\sin k_{2z}l,\\
M_{12} &= \frac{1}{2}(1-z_{13})\cos k_{2z}l + \frac{\mathrm{i}}{2}(z_{23}-z_{12})\sin k_{2z}l,\\
M_{21} &= \frac{1}{2}(1-z_{13})\cos k_{2z}l - \frac{\mathrm{i}}{2}(z_{23}-z_{12})\sin k_{2z}l,\\
M_{22} &= \frac{1}{2}(1+z_{13})\cos k_{2z}l - \frac{\mathrm{i}}{2}(z_{12}+z_{23})\sin k_{2z}l.
\end{aligned}$$

For simplicity, in this work, we consider two alternated non-magnetic materials, thus $z_{13} = 1$ and $\mu_1 = \mu_2$. Then, the coefficients are written as

$$\begin{aligned}
M_{11} &= \cos k_{2z}l + \frac{\mathrm{i}}{2}\left(\frac{k_{2z}}{k_{1z}} + \frac{k_{1z}}{k_{2z}}\right)\sin k_{2z}l,\\
M_{12} &= \frac{\mathrm{i}}{2}\left(\frac{k_{2z}}{k_{1z}} - \frac{k_{1z}}{k_{2z}}\right)\sin k_{2z}l,\\
M_{21} &= -\frac{\mathrm{i}}{2}\left(\frac{k_{2z}}{k_{1z}} - \frac{k_{1z}}{k_{2z}}\right)\sin k_{2z}l,\\
M_{22} &= \cos k_{2z}l - \frac{\mathrm{i}}{2}\left(\frac{k_{2z}}{k_{1z}} + \frac{k_{1z}}{k_{2z}}\right)\sin k_{2z}l.
\end{aligned} \tag{1.9}$$

Fabry-Perot resonances

By substituting (1.9) in (1.4) the transmission coefficient can be written as

$$T = \frac{1}{1+\frac{1}{4}\left(\frac{k_{2z}}{k_{1z}} - \frac{k_{1z}}{k_{2z}}\right)^2 \sin^2 k_{2z}l},$$

which is equal to 1 when $k_{2z}l = m\pi$ for $m \in \mathbb{Z}$ where $\mathbb{Z}$ corresponds to the set of integer numbers. Remember that the field inside the layer consists of a wave coming from the right and other coming from the left. Resonances appear when all the waves have the same phase. Then, the resonant frequencies are given by

$$\frac{\omega l}{\mathrm{c}}\sqrt{\epsilon_2}\cos\theta_2 = m\pi.$$

Finally, we can write the frequency in terms of the incident angle as

$$\omega_m = \frac{cm\pi}{l\sqrt{\epsilon_1}}\frac{1}{\sqrt{\epsilon_2/\epsilon_1 - \sin^2\theta_1}}.$$

Notice that the resonant frequencies exist only for $\epsilon_2 > \epsilon_1 \;\forall\, \theta_1$. For $\epsilon_2 < \epsilon_1$ there is a critical angle θ_c which determines if the wave produces a resonant effect or it is bounded inside the layer. The resonance process is called *Fabry-Perot resonance* and a graph of this is shown in figure 1.4 for three different values of the angle of incidence.

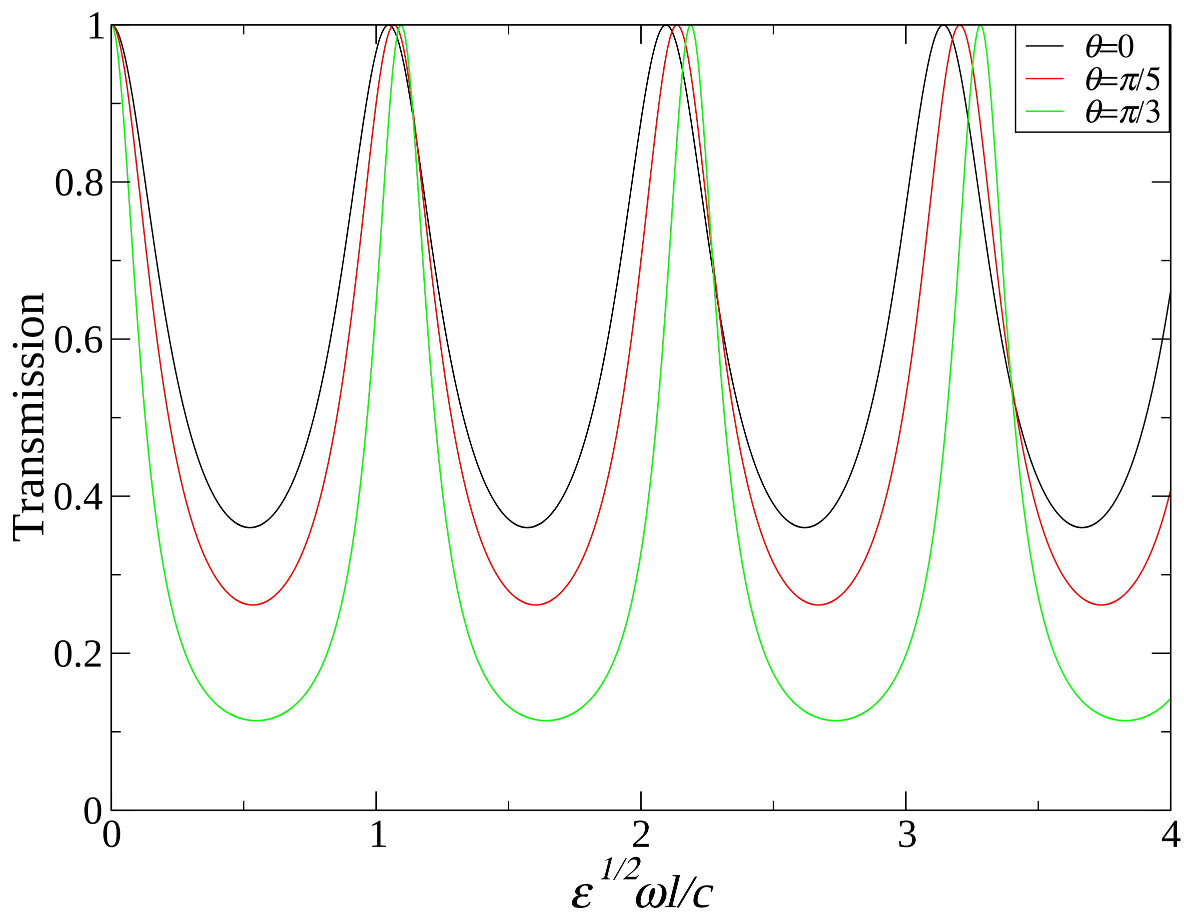

Figure 1.4: Transmission coefficient of a wave moving through a dielectric layer. The maximums of the coefficient are called *Fabry-Perot resonances*. In this case, the parameters are $n_1 = 1$, $n_2 = 3$, $\theta_1 = 0$ (black line), $\theta_1 = \pi/5$ (red line), $\theta_1 = \pi/3$ (green line), and $l = 1$. The frequency is measures in dimensionless units $\omega l/\mathrm{c}$.

A similar effect appears when a finite number of layers are added to the system. In that case, the number of resonances increases and produces two different behaviors, as will be shown below.

Photonic crystal

A photonic crystal is a layered medium which has a periodic structure in a finite or infinite array [20]. The system is composed by two materials, a and b, with different thickness, l_a and l_b, and different refraction indices, n_a and n_b, respectively. A diagram of a photonic system is shown in figure 1.5.

With the purpose of computing the transmission coefficient, we start by calculating the transfer matrix for a pair of layers,

$$\mathbf{M}_{ab} = \begin{pmatrix} \mathrm{e}^{\mathrm{i}k_a l_a} & 0 \\ 0 & \mathrm{e}^{-\mathrm{i}k_a l_a} \end{pmatrix} \mathbf{M}_b, \tag{1.10}$$

where the components of $\mathbf{M}_b$ are given by (1.9). Thus, the transfer matrix which describes a system with N pairs of layers can be written as the product of N matrices with the form of (1.10), *i.e.*,

$$\mathbf{M} = \mathbf{M}_{N,ab}\mathbf{M}_{N-1,ab}\cdots\mathbf{M}_{2,ab}\mathbf{M}_{1,ab} = \mathbf{M}_{ab}^{N}, \tag{1.11}$$

since the N matrices are exactly the same.

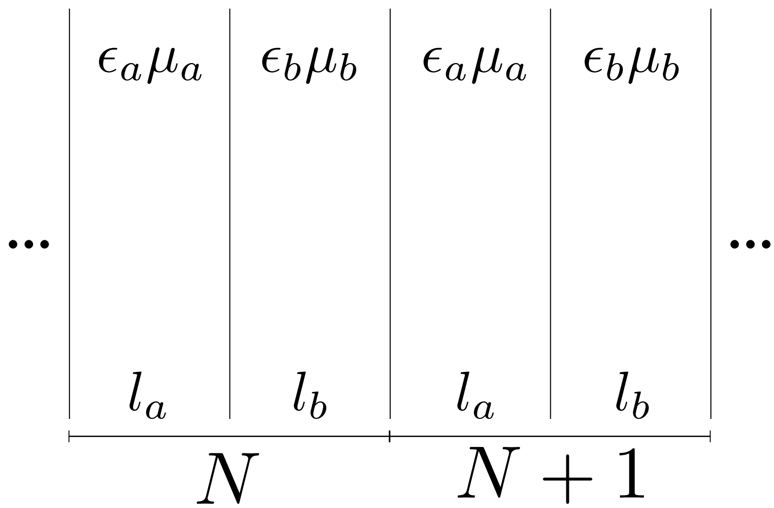

Figure 1.5: Diagram of an infinite photonic crystal formed by two different media. The figure shows the pair of layers labeled as N and $N+1$.

Quarter stack frequency

The natural frequency of the system ω_0 can be defined as [20]

$$\omega_0 n_a l_a = \frac{\pi}{2}\mathrm{c}.$$

By choosing ω/ω_0 as the new variable, the arguments of the sine and cosine functions in the components of each transfer matrix, equation (1.9) and (1.10), become

$$k_{az}l_a = \frac{\pi}{2}\frac{\omega}{\omega_0}\cos\theta_a \qquad \text{and} \qquad k_{bz}l_b = \frac{\pi}{2}\frac{\omega}{\omega_0}\frac{n_b l_b}{n_a l_a}\cos\theta_a.$$

where it can be observed that one of them, $k_{az}l_a$, does not depend on the length of the layers while the other one, $k_{bz}l_b$, just depends on the ratio between both lengths. Notice that this change of variable only works in the periodic case and it is given in terms of the layer thickness of one of the media. If we choose a system whose frequency is ω_0, then

$$k_a l_a = 2\pi\frac{l_a}{\lambda_a} = \frac{\pi}{2},$$

so,

$$l_a = \frac{\lambda_a}{4}.$$

This kind of systems are called *quarter stack layered medium* given the thickness of the layer is exactly a quarter of the wavelength.

Band structure

In order to shown the transmission coefficient in terms of the frequency, equation (1.11) has been numerically evaluated. The total transfer matrix is computed as a multiplication of N transfer matrices whose coefficients are given by the electromagnetic model. This kind of evaluation is the cornerstone of our numerical work, *i.e.* each ensemble elements in the numerical simulations presented in this Thesis is developed in the same way.

The graphs of the transmission coefficient in terms of the frequency of a photonic crystal are shown in figure (1.6) where we can observe two different behaviors. First, we observe frequency regions where the transmission is different from zero, these regions are called *transmission bands*. On the other hand, there are regions where the transmission coefficient equals zero, those are called *gaps*.

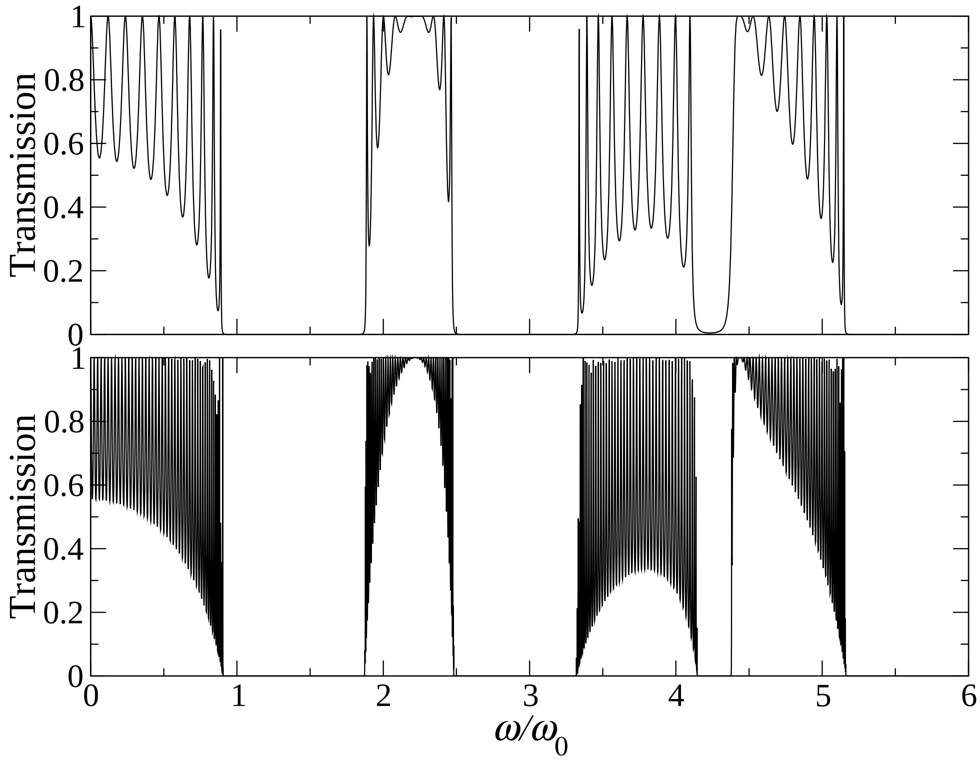

Figure 1.6: Transmission coefficient as a function of the frequency for a photonic crystal. In both cases, the thickness of the layers, the refraction indices and the incident angle are $2l_b = l_a$, $n_a = n_b/2$ and $\theta_a = \pi/3$, respectively. ω_0 corresponds to the quarter stack frequency. The top (bottom) panel shows a graph for $N = 10$ ($N = 50$).

The band structure is representative of layered systems and it is produced when the system is periodic.

Delay time

The first study about delay times was developed by Wigner [14] in 1955 who considered a particle interacting with a scatterer. According to [14], the derivative of the phase shift with respect to the energy can be interpreted as the time that takes a particle be reflect in a scattering process. Explicitly, the reflection delay time is given by [23]

$$\tau_R = \hbar \frac{\mathrm{d}\eta}{\mathrm{d}E}, \tag{1.12}$$

where η is the phase shift of the reflection amplitude and E denotes the energy of the incident particle. Note that for our electromagnetic model, the equation (1.12) can be written in terms of the wave frequency

$$\tau_R = \frac{\mathrm{d}\eta}{\mathrm{d}\omega}.$$

In order to understand the definition (1.12) given by Wigner [14], we present an example below.

A small example

Suppose a traveling plane wave $\mathrm{e}^{-\mathrm{i}k(x-L)}$ in a semi-infinite one-dimensional system where a finite potential is placed at $x = L$. The system is closed at the origin $x = 0$ by an infinite potential barrier while it is open at the other side. A diagram of the system can be observed in figure 1.7.

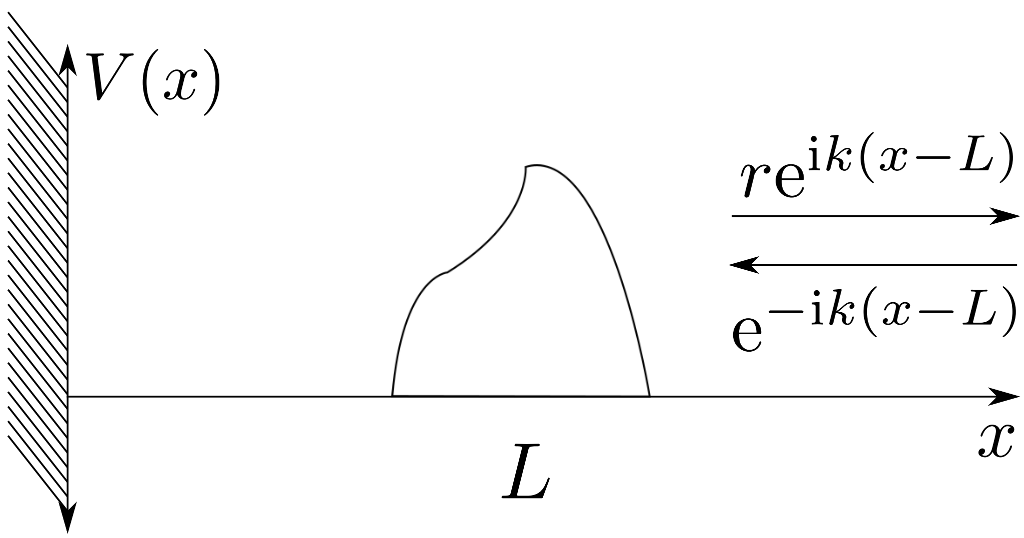

Figure 1.7: Diagram of a semi-infinite one-dimensional scattering system. The arrows show how the waves are moving with respect to the potential $V(x)$.

Since everything is reflected by the barrier, the scattering matrix becomes a 1×1 matrix whose unique element is the reflection amplitude r. Thus, r can be written as

$$r = \mathrm{e}^{\mathrm{i}\eta},$$

where η the corresponding phase of this amplitude and $|r|^2 = 1$. Then, the phase of the reflected wave function becomes

$$\theta = \mathrm{i}[k(x-L) + \eta].$$

By supposing a stationary phase with respect to the wavenumber k we get

$$\frac{\mathrm{d}\theta}{\mathrm{d}k} = \mathrm{i}\left[(x - L) + \frac{\mathrm{d}\eta}{\mathrm{d}k}\right] = 0, \tag{1.13}$$

where k can be written as a function of the energy

$$k = \frac{E}{v_g \hbar}. \tag{1.14}$$

Here, v_g is the group velocity. By substituting Eq. (1.14) into Eq. (1.13) it is obtained

$$x = L - \tau_R v_g, \qquad \text{with} \qquad \tau_R = \frac{\mathrm{d}\eta}{\mathrm{d}E}\hbar,$$

Thus, the wave is spatially retarded by $\tau_R v_g$ where τ_R is interpreted as the delay time.

2

Standard disorder (Anderson localization)

Justicia eterna son tus testimonios;

dame inteligencia, y viviré.

Salmo 119 144

Abstract

In this chapter, we focus on the study of disordered systems whose disorder distribution is characterized by a finite mean and a finite variance. Specifically, we are interested in transmission distributions and time delay distributions. In relation to delay times, a new approximation for finite systems in the localized regime is presented and tested.

Dimensionless length

The first incursion to the study of disordered systems was made by Anderson considering an infinite one-dimensional lattice [1]. In that work, the sense of disorder was introduced as the randomness of the impurities inside a given medium. The main result of the analysis was the discovery of a strong spatial, *i.e.* exponentially, localization of the wave function ψ. That means the diffusion of the wave takes place via jumps between localized sites. A diagram of the Anderson model is shown in figure 2.1. We write

$$|\psi| \propto \mathrm{e}^{x/l},$$

where l is called *mean free path* and represents the total decay distance of a superposition of waves inside a medium.

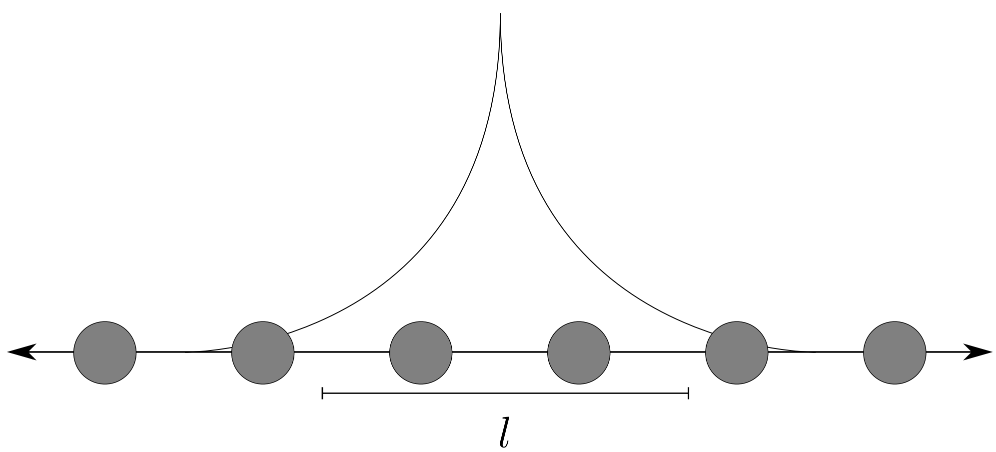

Figure 2.1: Simplified diagram of the Anderson model. Each gray circle represents an impurity. In the real case, the distance between any two impurities is random, as well as each impurity can have a random size.

Finite systems: transport regimes

It can be seen that the mean free path is fixed for the same amount of disorder. Thus, a natural question is how the transport properties are modified in the presence of a finite system of length L? To answer this it is necessary to call a new variable named *dimensionless length* which is defined as

$$s = \frac{L}{l}, \tag{2.1}$$

and measures the system in terms of the mean free path. Using this quantity two different transport regimes can be defined. Those are

- *Ballistic regime:* It is characterized by $s \ll 1$ which means the system length is smaller than the mean free path. Thus, the system is almost transparent and any wave can cross it without being reflected. As a consequence, the disordered sample is characterized by a transmission coefficient close to 1 and a reflection coefficient close to 0. A diagram of a disordered system in the ballistic regime is shown in figure 2.2.

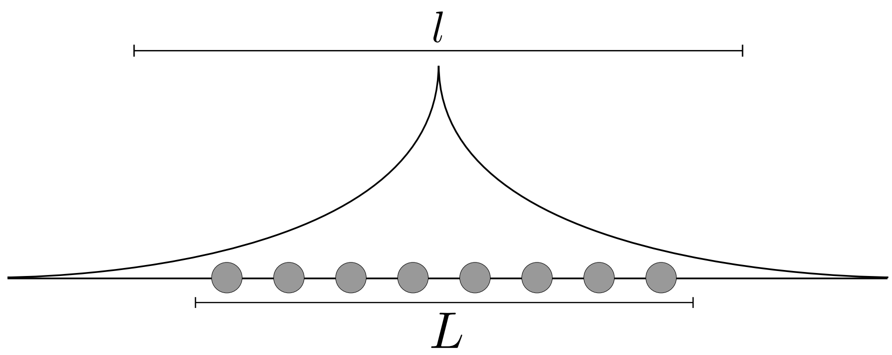

Figure 2.2: Simplified diagram of the Anderson model in the ballistic regime.

- *Localized regime:* It is characterized by $s \gg 1$ which means that the system length is greater than the mean free path. Thus, the waves cannot cross without being strongly scattered. As a consequence, those structures present a transmission coefficient close to 0 and a reflection coefficient close to 1. A diagram of a disordered system in the localized regime is shown in figure 2.3.

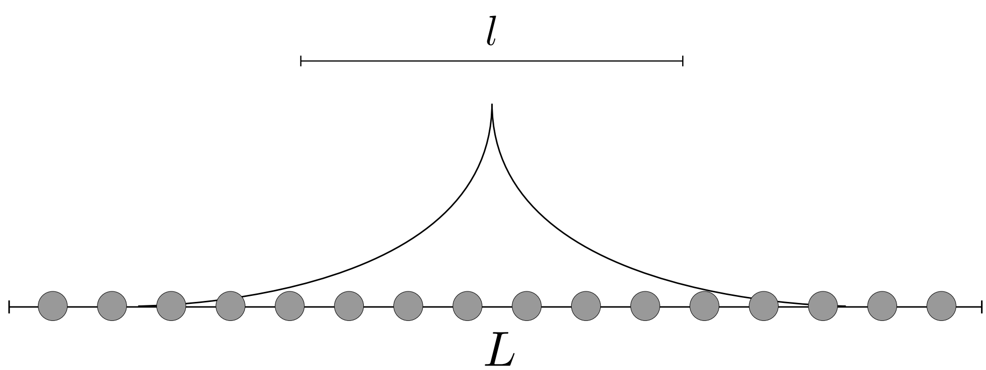

Figure 2.3: Simplified diagram of the Anderson model in the localized regime.

Additionally, there is a crossover region characterized by $s \sim 1$. There, any values of T between 0 and 1 can be obtained with the same probability [20].

Transmission probability density distribution

To find how the transmission probability density distribution evolves with the length of the system we assume the system in the *dense-weak-scattering limit* [24]. This means that the waveguide contains a very large number of weak scatterers, *i.e.*, $\lambda_0 \ll l$ where λ_0 is the wavelength relative to the wave frequency.

Fokker-Plank equation

The probability distribution of the transmission coefficient obeys a differential equation which has been obtained in [24, 25, 26, 27] using different methods. According to those authors, this distribution corresponds to the solution of a Fokker-Plank equation which, for a one-dimensional system, can be written in terms of λ as

$$\frac{\partial p(\lambda)}{\partial s} = \frac{\partial}{\partial \lambda}\left[\lambda(1+\lambda)\frac{\partial p(\lambda)}{\partial \lambda}\right],$$

here, s is the dimensionless length and λ is the radial variable of the transfer matrix in the polar representation

$$\mathbf{M} = \begin{pmatrix} \sqrt{1+\lambda}\mathrm{e}^{\mathrm{i}\phi_1} & \sqrt{\lambda}\mathrm{e}^{\mathrm{i}\phi_2} \\ \sqrt{\lambda}\mathrm{e}^{-\mathrm{i}\phi_2} & \sqrt{1+\lambda}\mathrm{e}^{-\mathrm{i}\phi_1} \end{pmatrix},$$

where ϕ_1 and ϕ_2 are the phases of each complex coefficient. Then, λ is expressed in terms of T as

$$\lambda = \frac{1-T}{T}.$$

The solution for $p(T)$ is given in [28] in terms of quadratures by the expression

$$p(T) = \frac{s^{-3/2}\mathrm{e}^{-s/4}}{\sqrt{2\pi}T^2}\int_{y_0}^{\infty} \mathrm{d}y \, \frac{y\mathrm{e}^{-y^2/4s}}{\sqrt{\cosh y + 1 - 2/T}}, \tag{2.2}$$

with $y_0 = \operatorname{arccosh}(2/T - 1)$. Notice that the probability density function only depends on the variable T and the dimensionless length s. That means that all the properties of the distribution are completely determined by the dimensionless parameter s. A simpler form of equation (2.2) was reported in [9] and is written as

$$p(T) = C\frac{\left[\operatorname{arccosh}(1/\sqrt{T})\right]^{1/2}}{T^{3/2}(1-T)^{1/4}}\mathrm{e}^{-(1/s)\operatorname{arccosh}^2(1/\sqrt{T})}, \tag{2.3}$$

where C is a normalization constant. As it is shown, the parameter s is crucial to define and understand the properties of each regime and, additionally allows computing the probability density function of T. The relation between s and T is the cornerstone of the *one-parameter scaling theory.*

One-parameter scaling theory

The distribution of $\ln T$ can be computed from (2.2). It is given by

$$T \to \ln T \quad \Longrightarrow \quad p(\ln T) = Tp(T),$$

where it is found that the average of $\langle \ln T \rangle$ is precisely the dimensionless length (2.1)

$$\langle \ln T \rangle = -s. \tag{2.4}$$

Remember that T can be easily obtained numerically from the transfer matrix or measured experimentally. Also, knowing the length of the system and its dimensionless length, equation (2.4) allows a direct measurement of the amount of disorder. In this sense, equation (2.4) allows characterizing any disordered system given its mean free path, *i.e.* its amount of disorder.

In order to continue using the electromagnetic model shown in Chapter 1, numerical simulations of a disordered system whose length is fixed was developed. The result of this simulation is shown in figure 2.4 for 6 different configurations. In three of them, we keep the frequency constant while the angle of incidence changes. Similarly for the others which keep the incidence angle constant while the frequency changes. The randomness in the simulations is introduced by choosing the thickness of the layers as random variables. Even though this simulation considers Gaussian random variables, the same results can be obtained by using any random variable which is characterized by a finite mean and a finite variance. All the simulations shown in this chapter were developed using Gaussian variables with mean μ and standard deviation σ.

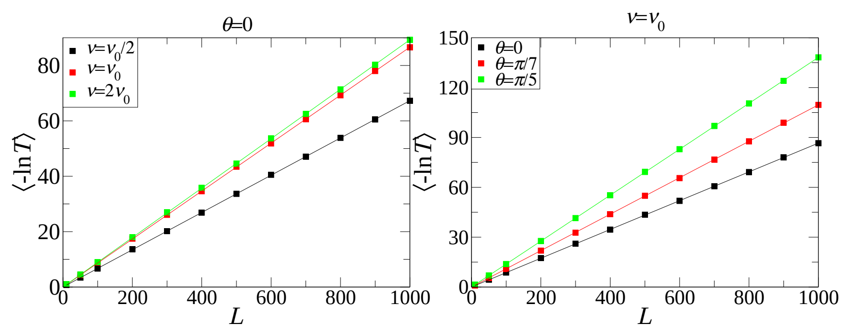

Figure 2.4: The average $\langle -\ln T\rangle = s$ as a function of the system size L for one-dimensional layered structures conformed by two different media (symbols). The thickness of each layer is given by the absolute value of a Gaussian random variable characterized by $\mu = 0$ and $\sigma = 1$. The parameters are $n_a = 1.4$, $n_b = 2.4$ and $\nu_0 = 7.5$ GHz. In the right [left] panels we keep the frequency [incident angle] constant while the incident angle [frequency] changes. The solid lines are fittings of the data with Eq. (2.1). Each symbol was calculated using 10^4 ensemble realizations.

In general, the amount of disorder depends on the difference between the refraction indices, the angle of incidence, the energy of the wave as well as the thickness of the scatterers. Figure 2.4 also shows how the amount of disorder depends on two of these parameters, ν and θ.

Finally, we compare equation (2.3) with numerical simulations in figure 2.5. The two transport regimes are presented in that figure: the upper left panel shows the probability distribution function $p(T)$ in the ballistic regime and the lowers panels show the PDF $p(\ln T)$ in the localized regime. Note that the upper right panel shows the PDF $p(T)$ in the crossover region. Also, the lower panels show the log-normal behavior of the transmittance in the limit $L \gg l$.

Delay time

Additionally to the definition of the time delay given by Wigner [14] and presented in Chapter 1, Smith [23] defined the delay time of a system in terms of the lifetime matrix,

$$\mathbf{Q} = \mathrm{i}\hbar\mathbf{S}^* \frac{\mathrm{d}\mathbf{S}}{\mathrm{d}E},$$

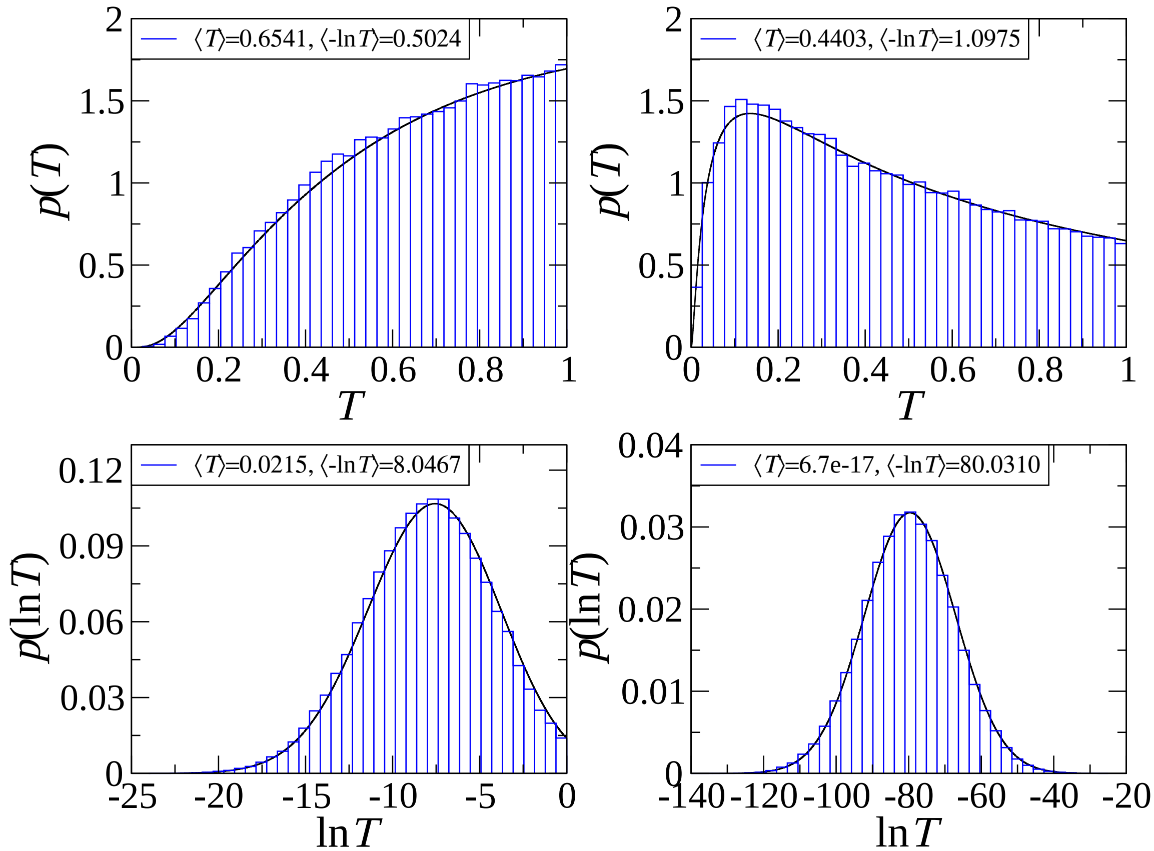

Figure 2.5: The probability density functions $p(T)$ [upper] and $p(\ln T)$ [lower] for one-dimensional layered structures conformed by two different media (histograms). The thickness of each layer is given by the absolute value of a Gaussian random variable characterized by $\mu = 0$ and $\sigma = 1$. The parameters are $n_a = 1.4$, $n_b = 2.4$, $\nu = 7.5$ GHz and $\theta = 0$. Both, $\langle T\rangle$ and $\langle -\ln T\rangle$, are shown in each panel in order to identify the transport regime. The solid black line is the theoretical prediction (2.3). Each histogram was calculated using 10^5 ensemble realizations. A good agreement between theory and numerical simulations is observed.

where $\mathbf{Q}$ is called *lifetime matrix* or *delay time matrix* and $\mathbf{S}$ is the scattering matrix. Then, the elements $Q_{i,j}$ of $\mathbf{Q}$ correspond to the delay times of the system

$$\mathbf{Q} = \begin{pmatrix} \tau_{R'} & \tau_T \\ \tau_{T'} & \tau_R \end{pmatrix}.$$

Here $\tau_{R'}$, τ_T and $\tau_{T'}$ correspond to the delay times of the r', t and t' amplitudes, respectively.

The existence of negative delay times has been discussed widely in [29, 30, 31]. Negative delay times do not contradict the principle of causality and have been related to the distortion of the wave, even when the wave does not appear distorted.

Mathematically, negative delay times appear in a natural way if the scattering matrix is written in terms of the transmission coefficient and the determinant of the matrix [19]

$$\mathbf{S} = \mathrm{e}^{\mathrm{i}\phi_F/2} \begin{pmatrix} \sqrt{1-T}\mathrm{e}^{\mathrm{i}\rho} & \mathrm{i}\sqrt{T}\mathrm{e}^{-\mathrm{i}\chi} \\ \mathrm{i}\sqrt{T}\mathrm{e}^{\mathrm{i}\chi} & \sqrt{1-T}\mathrm{e}^{-\mathrm{i}\rho} \end{pmatrix}, \tag{2.5}$$

where ϕ_F represents the global phase of the system which is called *Friedel phase*. Here, ρ is the asymmetry phase and χ is named magnetic phase which can be removed by a gauge transformation. Note that the phases of r and r' are given by $\eta_r = \phi_F/2+\rho$ and $\eta_{r'} = \phi_F/2-\rho$, respectively. It is clear that if $\Delta\rho > \Delta\phi_F/2 > 0$ then $\Delta\eta_{r'} < 0$. Hence, the delay time is negative in this case and it is common where the reflection phase changes suddenly. Similarity, for $\Delta\phi_F/2 > 0 > \Delta\rho$ with $|\Delta\rho| > |\Delta\phi_F/2|$ where $\Delta\eta_r < 0$.

Now that the basic aspects of delay times have been presented, the statistical methods required to describe a disordered system may be introduced. We will concentrate on the distribution functions and the average of this quantity.

Disorder in the half-line

Delay times in disordered systems have been studied from two different approaches. The first approach considers a Fokker-Planck equation for the probability density function of delay times [15, 32]. This approach relates the problem of transport through a disordered structure with the exponential Brownian motion problem. The second approach is based on the definition of the delay time matrix [17, 33]. It is important to note that the second approach works in the localized regime, specifically on the study of very long systems; while the first approach leads to a general solution. Right now, we concentrate on the first approach and the second one will be presented later.

The problem of a quantum particle moving through a disordered medium was solved in [15]. The most important assumption to reach the solution is to consider disorder in the half-line. This means that for a one-dimensional system, the region of interest lies on $0 < x < L$, where L is the length of the disordered system and it is semi-closed. Thus, at $x = 0$, the system becomes impenetrable by means of an infinite potential. Hence, the scattering matrix becomes an 1×1 matrix whose unique element is the reflection amplitude, *i.e.*, the reflection coefficient is $R = 1$. A diagram of the half-line problem is shown in figure 2.6.

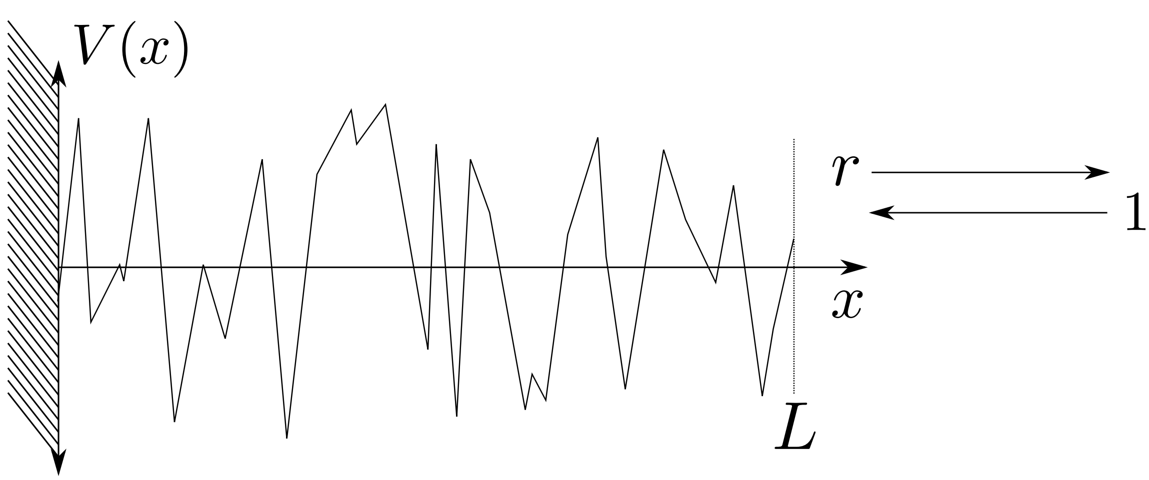

Figure 2.6: Diagram of the half-line problem. The system is closed at $x = 0$ by an infinite wall and it is open at $x = L$.

For the half-line scattering problem, the probability density function of delay times obeys a Fokker - Planck equation which is written as

$$\frac{\partial p(\tau_R)}{\partial L} = \frac{\partial}{\partial \tau_R}\left[\left(\frac{2}{\gamma}-2\right)p(\tau_R)\right] + \frac{2}{\gamma}\frac{\partial}{\partial \tau_R}\tau_R\frac{\partial}{\partial \tau_R}\tau_R p(\tau_R), \tag{2.6}$$

where γ is called *scattering time* and represents the time that the wave takes to move a distance equivalent to two mean free paths. Hence, this quantity can be written as $\gamma = 2l/v_g$, where v_g is the group velocity. The solution of (2.6), considering $L \to \infty$[1], is

$$p(\tau_R) = \frac{\gamma}{\tau_R^2}\mathrm{e}^{-\gamma/\tau_R}. \tag{2.7}$$

Notice that the relations between the scattering time and the mean free path allow writing (2.7) in terms of the dimensionless length s. A comparison between equation (2.7) and numerical simulations is shown in figure 2.7[2].

In figure 2.7 the amount of disorder remains the same in each graph while the length of the system changes for each of these examples. Also, the discrepancies between the theoretical curve and numerical simulations increase when s decreases, *i.e.*, when L decreases or l increases. Given that γ is determined by the amount of disorder, it can be measured from numerical simulations. Then, the comparisons in figure 2.7 do not contain any free parameter.

From figure 2.7 can be observed that negative delay times vanish for larges s though they are presented in any open system. However, equation (2.7) does not predict negative delay times.

The Fokker-Plank equation, eq. (2.6), also corresponds to the description of an exponential Brownian motion with drift [15, 32, 34] where the existence of the complete solution allows computing all the moments of this distribution [15, 19]. The calculation of $\langle\tau\rangle$ from equation (2.7) leads to divergence for all γ, but according to Ref. [15, 19], the average of the delay time diverges linearly with the length of the system

$$\langle\tau_R\rangle \propto L. \tag{2.8}$$

Numerical simulations have been performed to test this equation; they can be observed in figure 2.8.

From figure 2.8, it can be observed that $\langle\tau_R\rangle$ does not depend on the frequency ν nor the angle of incidence θ. The non-dependence on the energy $E = \hbar\omega$ of the delay time average in a disordered system has been discussed in [35]. The data analysis of figure 2.8 also allows finding the constant of proportionality of equation (2.8) which is the inverse of the group velocity

$$\langle\tau_R\rangle = \frac{L}{v_g}. \tag{2.9}$$

That means, the average of the reflection delay time corresponds to the time spent to reach the middle of the waveguide and come back to the initial point.

[1] See [15], equation (12) for the complete solution.

[2] All graphs shown in this chapter have been normalized to help visualization.

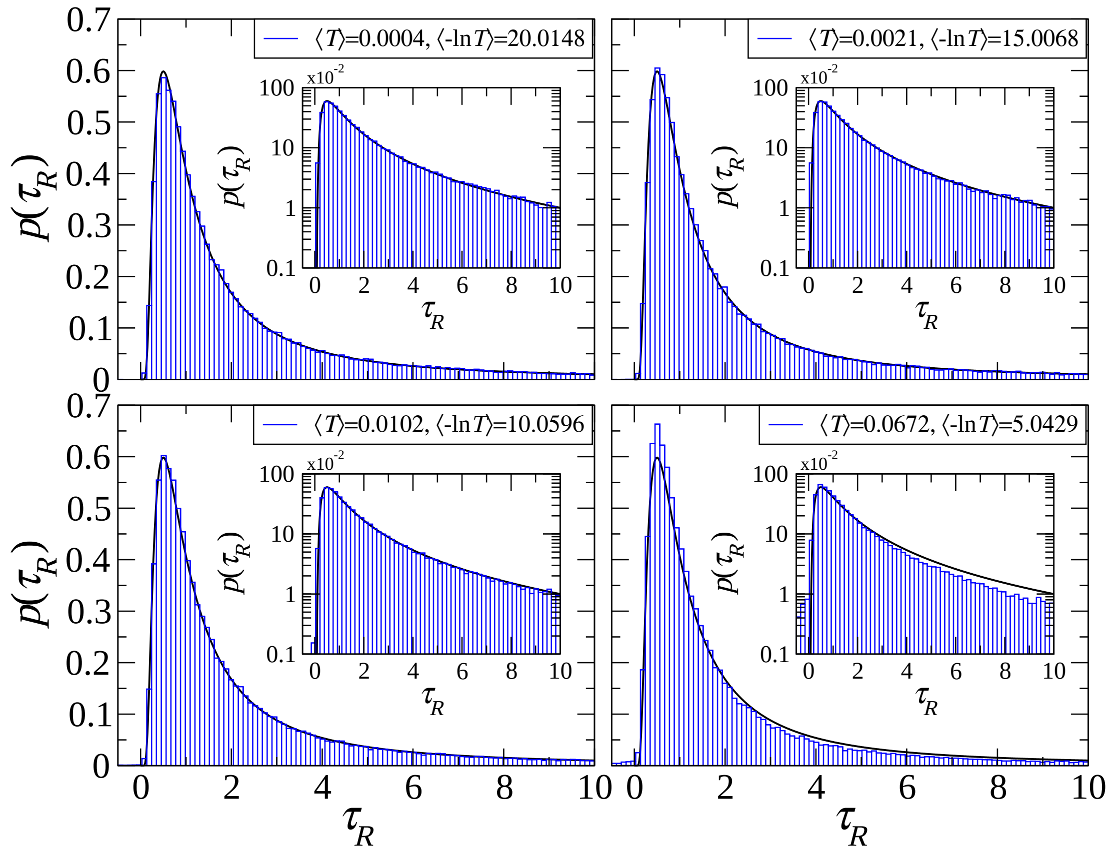

Figure 2.7: The probability density function $p(\tau_R)$ for one-dimensional layered structures conformed by two different media (histograms). The thickness of each layer is given by the absolute value of a Gaussian random variable characterized by $\mu = 0$ and $\sigma = 1$. The parameters are $n_a = 1.4$, $n_b = 2.4$, $\nu = 7.5$ GHz and $\theta = 0$. Both, $\langle T \rangle$ and $\langle -\ln T \rangle$, are shown in each panel in order to identify the transport regime. The inset of each panel presents the same histogram of the main panel in semi-log scale. The solid black line is the theoretical prediction (2.7). Each histogram was calculated using 10^5 ensemble realizations. A good agreement between theory and numerical simulations is observed but the discrepancies increase when s decreases. Here, we considered the change of variable $\tau_R/\gamma \Rightarrow \tau_R$.

Notice that for an open system with homogeneous disorder the reflection delay times τ_R and $\tau_{R'}$ are expected to be statistically identical, even when $r \neq r'$. This characteristic does not depend on the transport regime but only on the homogeneity of the disorder.

For the localized regime, it is important to note that the wave almost does not enter into the system. Then, the scattering waves coming from the left and the right do not interact. Thus, we can conclude that τ_R and $\tau_{R'}$ are statistical independents in this regime. But, when s decreases and both waves enter into the system, thus τ_R and $\tau_{R'}$ become correlated variables.

Independent random reflections

Another important question we can explore is how long a wave takes to go through all the system and leave it by the opposite side. The quantity which measures this time is called *transmission delay time* and it is defined by the derivative of the phase shift of the transmission amplitude with respect to

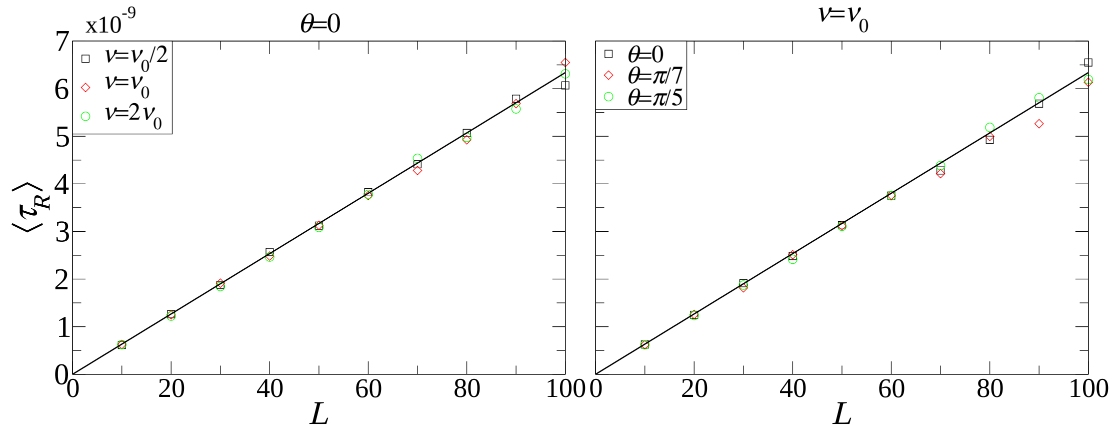

Figure 2.8: The average $\langle \tau_R \rangle$ as a function of the system size L for one-dimensional layered structures conformed by two different media (symbols). The thickness of each layer is given by the absolute value of a Gaussian random variable characterized by $\mu = 0$ and $\sigma = 1$. The parameters are $n_a = 1.4$, $n_b = 2.4$ and $\nu_0 = 7.5$ GHz. In the right [left] panel we keep the frequency [incident angle] constant while the incident angle [frequency] changes. The solid lines are given by Eq. (2.9). Each symbol was calculated using 2×10^4 ensemble realizations. This graph does not contain any normalization over τ_R.

the energy. As the reflection delay time, the transmission delay time can be expressed as a derivative with respect to the frequency for the electromagnetic case. In order to describe the distribution of this quantity, it is possible to obtain a relationship from the condition of unitarity of the scattering matrix [18] which can be written as

$$\tau_T = \frac{\tau_R + \tau_{R'}}{2}, \tag{2.10}$$

and is valid for all transport regimes. This relation does not depend on the disorder nor its homogeneity.

We know that the probability density function of a sum of independent random variables is given by the integral of their joint distribution. As we mentioned before, in the localized regime, both variables are independent. Hence, the joint distribution is

$$p(\tau_R, \tau_{R'}) = p(\tau_R)p(\tau_{R'}). \tag{2.11}$$

Then, the probability density function of τ_T can be written as

$$p(\tau_T) = \int_0^{\tau_T} p(\tau_R)p(2\tau_T - \tau_R)\, \mathrm{d}\tau_R\,, \tag{2.12}$$

whose solution was obtained analytically by Schomerus [18] and has the form

$$p(\tau_T) = \frac{\gamma^2}{\tau_T^3} \mathrm{e}^{-\gamma/\tau_T} \left[K_0\left(\frac{\gamma}{\tau_T}\right) + K_1\left(\frac{\gamma}{\tau_T}\right)\right]. \tag{2.13}$$

Here, K_0 and K_1 represent the modified Bessel functions of the second kind. Numerical simulations have been performed to compare our numerical model against this result and they are shown in figure 2.9.

As in figure 2.7, in all graphs we keep the mean free path constant while the length changes. Note that the discrepancies between equation (2.13) and numerical simulations increase when s decreases.

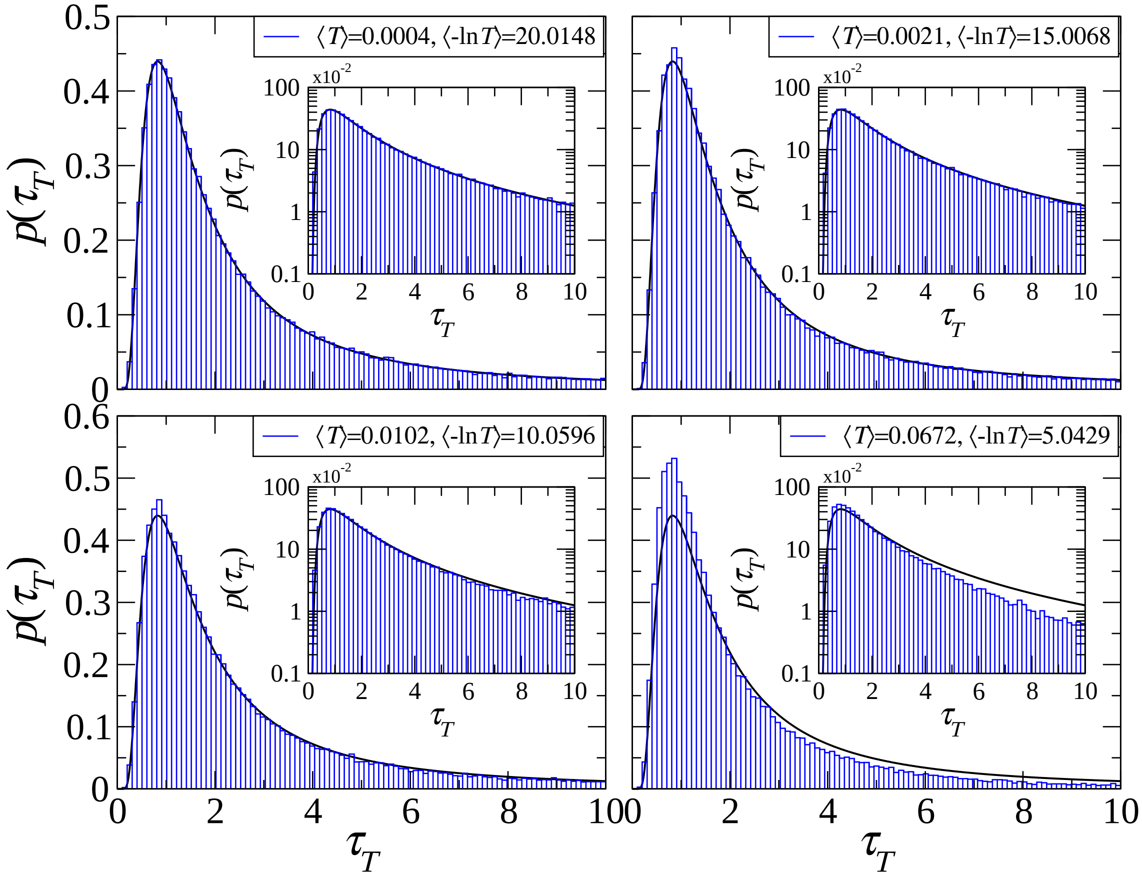

Figure 2.9: The probability density function $p(\tau_T)$ for one-dimensional layered structures conformed by two different media (histograms). The thickness of each layer is given by the absolute value of a Gaussian random variable characterized by $\mu = 0$ and $\sigma = 1$. The parameters are $n_a = 1.4$, $n_b = 2.4$, $\nu = 7.5$ GHz and $\theta = 0$. Both, $\langle T \rangle$ and $\langle -\ln T \rangle$, are shown in each panel in order to identify the transport regime. The inset of each panel presents the same histogram of the main panel in semi-log scale. The solid black line is the theoretical prediction (2.13). Each histogram was calculated using 10^5 ensemble realizations. A good agreement between theory and numerical simulations is observed but the discrepancies increase when s decreases. Here, we considered the change of variable $\tau_T/\gamma \Rightarrow \tau_T$.

That is because equation (2.9) is just an approximation for very long systems that do not work for systems whose transmission coefficient is finite $T > 0$. Also, it is supposed that the reflection delay times are independent between them but this is not true near the ballistic regime. Since both waves, the one which comes from the right and the other which comes from the left, penetrate the system a lot, they do interact. Then, τ_R and $\tau_{R'}$ are increasingly correlated when s decreases and equation (2.11) does not hold.

Finally, from equation (2.10) and assuming that τ_R and $\tau_{R'}$ are identically distributed for this kind of disorder, it can be found that $\langle \tau_R \rangle = \langle \tau_{R'} \rangle = \langle \tau_T \rangle$. Then, from (2.9)

$$\langle \tau_T \rangle = \frac{L}{v_g}, \tag{2.14}$$

which is shown in figure 2.10. Here, equation (2.14) is interpreted as the time that a wave takes to cross all the structure.

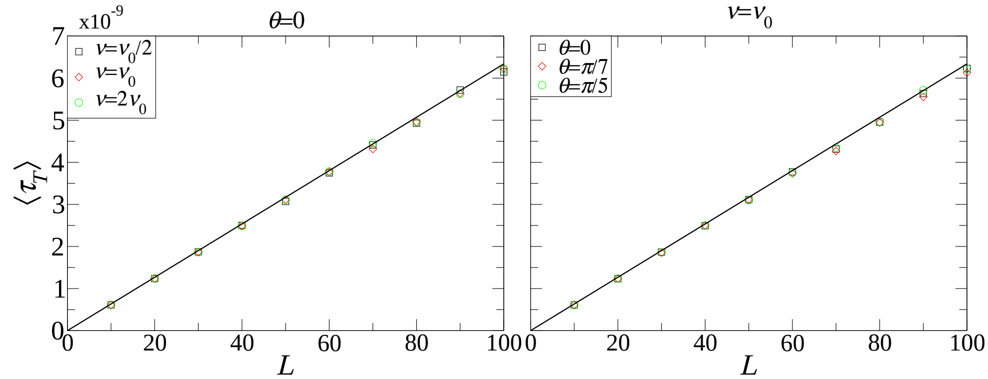

Figure 2.10: The average $\langle \tau_T \rangle$ as a function of the system size L for one-dimensional layered structures conformed by two different media (symbols). The thickness of each layer is given by the absolute value of a Gaussian random variable characterized by $\mu = 0$ and $\sigma = 1$. The parameters are $n_a = 1.4$, $n_b = 2.4$ and $\nu_0 = 7.5$ GHz. In the right [left] panel we keep the frequency [incident angle] constant while the incident angle [frequency] changes. The solid lines are given by Eq. (2.14). Each symbol was calculated using 2×10^4 ensemble realizations. This graph does not contain any normalization over τ_T.

Systems with finite transmission

We have seen that equation (2.7) works well in the localized regime, however, our main interest lies in obtaining an expression that works better than this one near the ballistic regime $s \sim 1$. In [17, 33] expression (2.7) has been obtained considering small absorption. Those works consider an imaginary frequency shift given by the rate $1/\tau_0$ where τ_0 is a constant related to the absorption[3]. That allows writing the reflection coefficient as

$$rr^\dagger = r_0 \left[1 - \frac{1}{\tau_0} \mathbf{Q} \right] r_0^\dagger. \tag{2.15}$$

Here, r represents the reflection amplitude after the frequency shift, r_0 the reflection amplitude before the frequency shift and $\mathbf{Q}$ the lifetime matrix.

As we can observe, the first term on the right-hand of equation (2.15) represents the reflection coefficient without absorption and the second one represents the losses produced by the absorption. Remember that even though the system is open on both sides, the transmission coefficient vanishes. We can use expression (2.15) considering our system has reflection "losses" due to the finite transmission. Then, the reflection coefficient in terms of the delay time is given by

$$R = 1 - \frac{\tau_R}{\tau_0}, \tag{2.16}$$

where the distribution of the reflection coefficient for a one-channel system with time-reversal symmetry has the form [17, 18, 33, 36]

$$p(\lambda) \propto \mathrm{e}^{-\gamma\lambda/\tau_0}, \tag{2.17}$$

with $\lambda = R/(1-R) \geq 0$. By substituting (2.16) into (2.17) we obtain the probability density function

$$p(\tau_R) = \frac{\gamma}{2 - \mathrm{e}^{-\gamma/\tau_0}} \frac{1}{\tau_R^2} \mathrm{e}^{-\frac{\gamma}{\tau_0}\left| \frac{\tau_0 - \tau_R}{\tau_R} \right|}. \tag{2.18}$$

[3]In our case, this constant will be related to another characteristic of the system which will be identified numerically.

Where it can be observed that for systems whose reflection coefficient is near to 1, $\lambda \to 1/(1-R)$, expression (2.7) is recovered from (2.17).

In order to find τ_0, numerical simulations were performed and they can be seen in figure 2.11. Figure 2.11 also shows the comparison between both distributions for the reflection delay time, eqs. (2.7) and (2.18). It is observed that the behavior of equation (2.7) is numerically recovered from equation (2.18) when $T \to 0$.

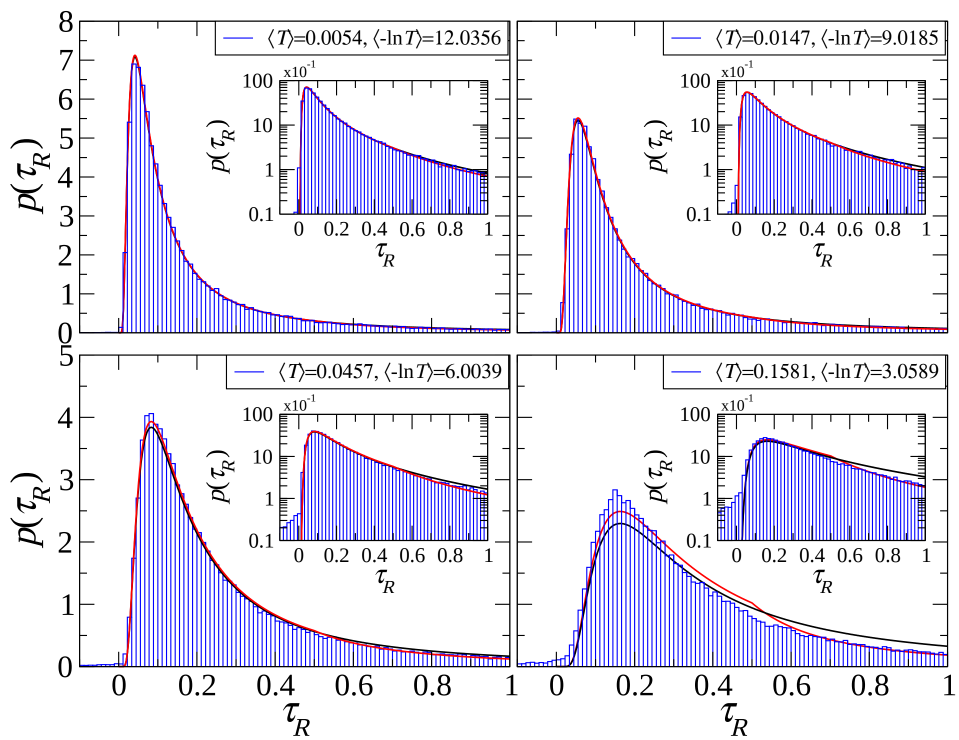

Figure 2.11: The probability density function $p(\tau_R)$ for one-dimensional layered structures conformed by two different media (histograms). The thickness of each layer is given by the absolute value of a Gaussian random variable characterized by $\mu = 0$ and $\sigma = 1$. The parameters are $n_a = 1.4$, $n_b = 2.4$, $\nu = 7.5$ GHz and $\theta = 0$. Both, $\langle T \rangle$ and $\langle -\ln T \rangle$, are shown in each panel in order to identify the transport regime. The inset of each panel presents the same histogram of the main panel in semi-log scale. The solid black [red] line is the theoretical prediction (2.7) [(2.18)] with $\tau_0 = \langle \tau_R \rangle$. Each histogram was calculated using 10^5 ensemble realizations. A good agreement between theory and numerical simulation is observed. Here, we considered the change of variable $v_g \tau_R / 2L \Rightarrow \tau_R$.

It can be observed that the distribution (2.18) works better than the distribution (2.7) for systems whose transmission coefficient does not vanish. Also, from the numerical simulations, it can be concluded that τ_0 represents the mean of the delay time distribution. Notice that both quantities, γ and τ_0, can be measured from the numerical simulations or experimentally. In this way, all theoretical curves can be generated without free parameters. Assuming that $\tau_0 = \langle \tau_R \rangle$ and making the change of variable $\tau_R / \langle \tau_R \rangle \Rightarrow \tau_R$ distribution (2.18) can be written as

$$p(\tau_R) = \frac{1}{2 - e^{-2/s}} \frac{2}{s \tau_R^2} e^{-\frac{2}{s}\left|\frac{1}{\tau_R} - 1\right|}, \tag{2.19}$$

which shows that the statistics are completely determined by the dimensionless length s.

From figure 2.11, it can be observed that the number of negative delay times increases when s decreases. Even though distribution (2.18) improves the agreement with the numerical results, it is important to note that this distribution does not explain negative delay times either.

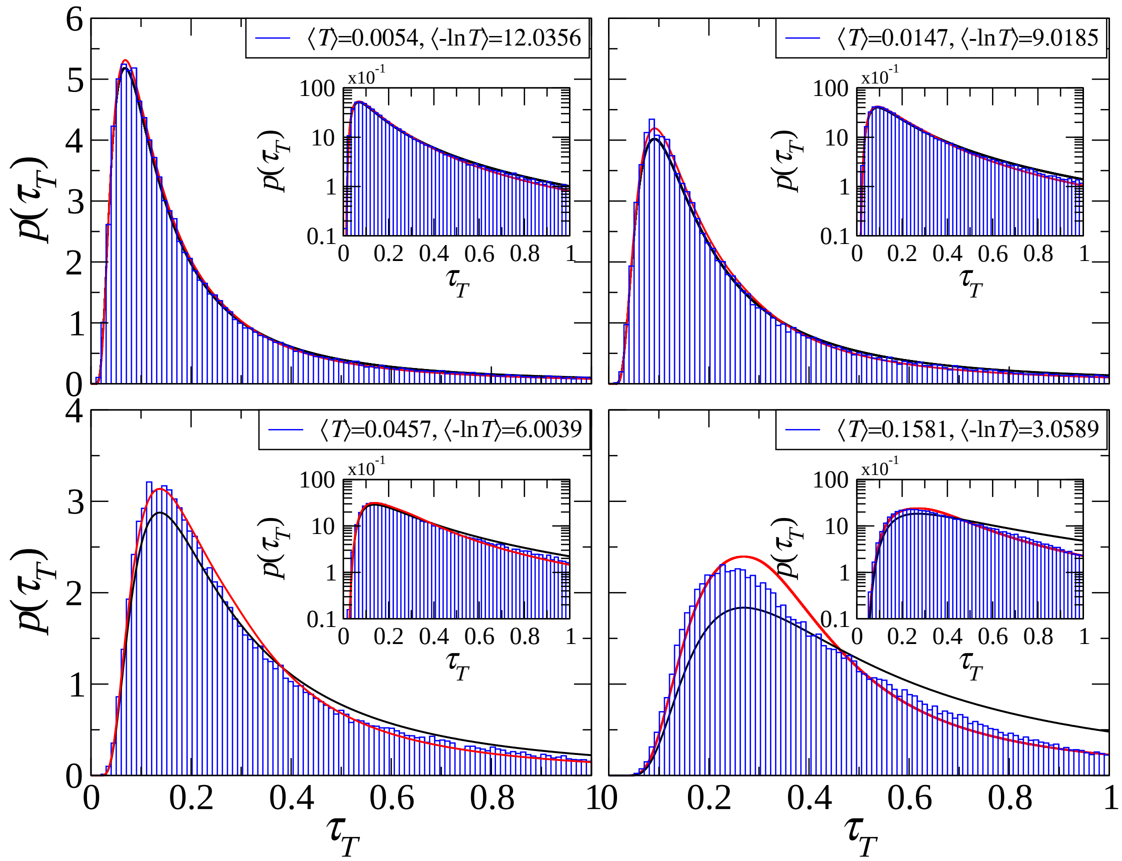

Figure 2.12: The probability density function $p(\tau_T)$ for one-dimensional layered structures conformed by two different media (histograms). The thickness of each layer is given by the absolute value of a Gaussian random variable characterized by $\mu = 0$ and $\sigma = 1$. The parameters are $n_a = 1.4$, $n_b = 2.4$, $\nu = 7.5$ GHz and $\theta = 0$. Both, $\langle T\rangle$ and $\langle -\ln T\rangle$, are shown in each panel in order to identify the transport regime. The inset of each panel presents the same histogram of the main panel in semi-log scale. The solid black [red] line is the theoretical prediction (2.12) taking $p(\tau_R)$ as (2.7) [(2.18)] with $\tau_0 = \langle \tau_T\rangle$. Each histogram was calculated using 10^5 ensemble realizations. A good agreement between theory and numerical simulation is observed. Here, we considered the change of variable $v_g\tau_T/2L \Rightarrow \tau_T$.

The distribution of τ_T can be obtained from the convolution (2.12) of the distributions of τ_R and $\tau_{R'}$. The comparison is shown in figure 2.12. We have to stress that equation (2.10) is valid in all regimes, but equation (2.11) holds for very long systems when τ_R and $\tau_{R'}$ are not correlated. Despite τ_R and $\tau_{R'}$ are not independent variables, both distributions shows a good agreement with the numerical data. Finally, it can be observed that distribution (2.18) works better than (2.7), especially at the tail of the distribution.

In addition to the results presented in this chapter, the transport properties of structures with absorption are presented in Appendix A. Also, delay times in the ballistic regime are studied in Appendix B.

3

Disorder in Lévy structures (Anomalous localization)

I'm not afraid to bleed,
but I won't do it for you,
a star among the hypocrites
the melody of our time.
In Flames (Dead end)

Abstract

In this chapter, structures whose disorder cannot be characterized by a finite mean or finite variance are presented and discussed. First, some properties of stable distributions are shown. Then, those distributions are used to construct disordered systems whose transmission properties are studied. Next, the statistical distribution of delay times is characterized.

Stable distributions

As mentioned in the previous chapter, the characteristics of the Anderson localization phenomena and the one-parameter scaling theory can be applied to any system whose disorder is given in terms of a random variable with finite mean and finite variance. But, what happens if the distribution which generates the disorder does not have these properties? Such distributions are called *stable distributions* or *Lévy-type distributions* and are characterized by long tails, *i.e.*, for large x, the probability density function becomes

$$p(x) \sim \frac{1}{x^{1+\alpha}}, \tag{3.1}$$

where α is the *stability parameter* and satisfies $0 < \alpha < 2$ [11]. This parameter determines the shape and decay of the distribution. Notice the first moment of the distribution diverges in this domain, but the second moment just does it for $\alpha < 1$. In addition to α, the shape of Lévy distributions is determined by a skewness parameter β where $-1 < \beta < 1$. In general, β is related with the symmetry of the distribution. This means, for $\beta = 1$ all the distribution lies on the x positive axis.

It is important to remark that stable distributions allow defining a *generalized central limit theorem*, *i.e.*, a sum of a large number of random variables without finite mean and finite variance lead to a Lévy distribution.

Simulation of Lévy distributions

Numerically, a Lévy random number characterized by α and $\phi_0(\alpha, \beta)$ can be obtained using [11]

$$y(\alpha, \beta) = \frac{\sin[\alpha(\phi + \phi_0)]}{(\sin\phi)^{1/\alpha}} \left(\frac{\cos[\phi - \alpha(\phi + \phi_0)]}{W} \right)^{1/\alpha - 1} \qquad \text{for} \qquad \alpha \neq 1, \tag{3.2}$$

where ϕ is an uniform random number in the interval $(-\pi/2, \pi/2)$ and W is exponentially distributed with mean 1. Particularly, if $\beta = 1$ and $\alpha < 1$, $\phi_0 = \pi/2$, also if $\beta = 0 \; \forall \; \alpha$, then $\phi_0 = 0$ and finally, if $\alpha = 2$ and $\beta = 0$, $\phi_0 = 0$ and the Box-Müller algorithm for Gaussian variables applies [37]. Figure 3.1 shows four different examples of Lévy distributions for different α-values in the symmetric case $\beta = 0$. Even though equation (3.2) does not define the values of the random variable for $\alpha = 1$, there is a result which considers $\beta = 0$:

$$y(1, 0) = \tan(\phi).$$

The distribution generated by these specific parameters is called *Cauchy distribution* and it is one of the very special cases which have an analytical probability density function. This density function can be written as

$$q_{1,0}(x) = \frac{1}{\pi(1 + x^2)}.$$

Another important example of these special cases is when $\alpha = 1/2$ and $\beta = 1$ where the PDF becomes

$$q_{1/2,1}(x) = \frac{1}{\sqrt{2\pi}} \mathrm{e}^{1/2x} x^{-3/2},$$

and it is named *Lévy distribution*. For all the other values of α and β, the PDF must be computed numerically.

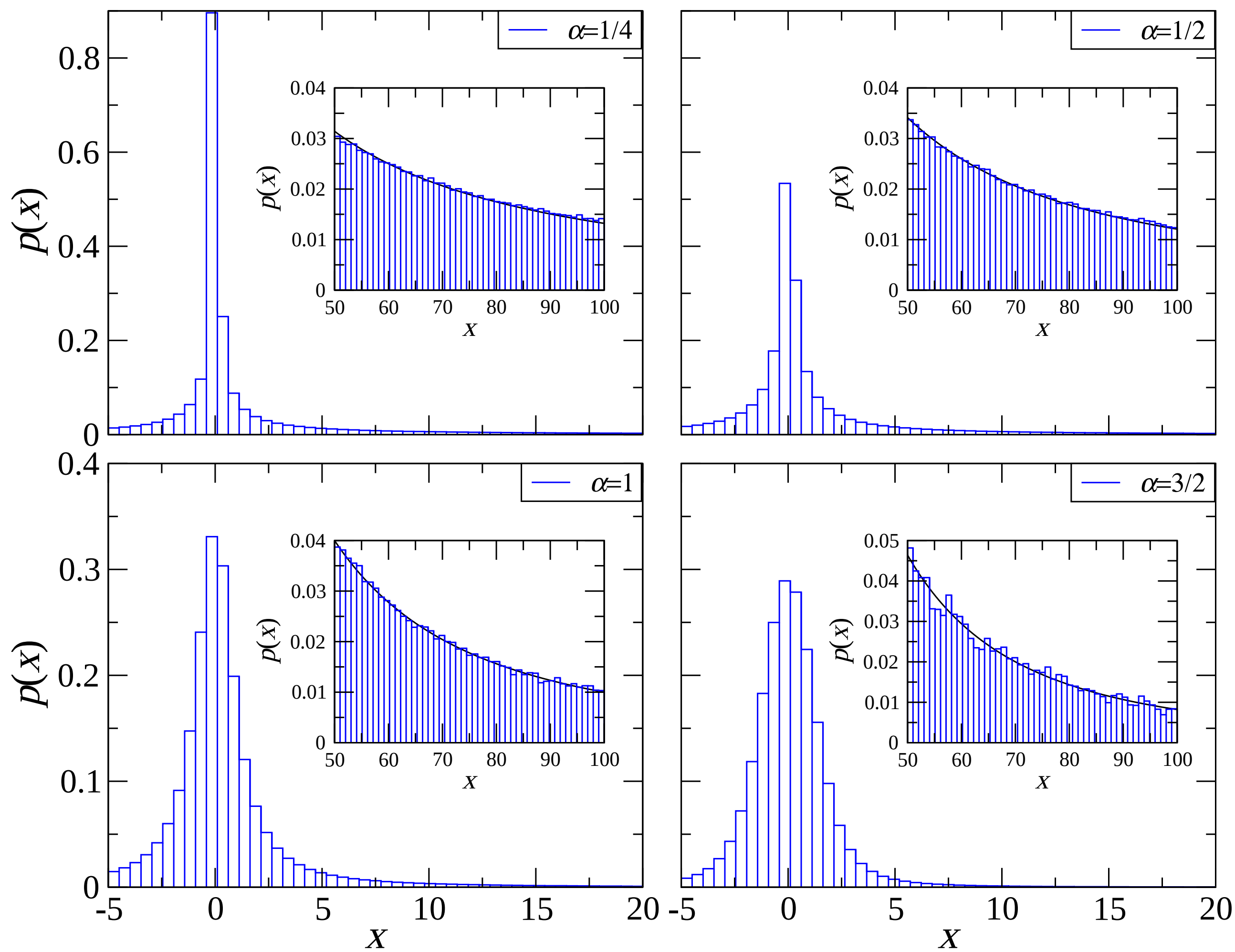

Figure 3.1: Lévy-type probability density functions for four different stability parameters and $\beta = 0$. The inset of each panel shows part of the tail of the distribution, the solid black line is equation 3.1. Each histogram was calculated using 10^7 ensemble realizations.

Transport using Lévy disorder

Stable distributions have been used in different and diverse fields of science [11, 12, 13]. Considering wave transport based on Lévy flights, new disordered media named *Lévy glasses* have been created and their transport properties were measured [4]. These media are composed of microspheres of glass whose diameters are characterized by a Lévy distribution. Motivated by these experimental works, the first theoretical studies related with these distributions were developed in [5, 6, 38], where it was found that the behavior of the average of the dimensionless conductance is given by

$$\langle -\ln T \rangle \propto \begin{cases} L^{\alpha} & \text{for} \quad 0 < \alpha < 1 \\ L & \text{for} \quad \alpha \geq 1 \end{cases} . \tag{3.3}$$

In contrast to the Anderson localization and the one-parameter scaling theory where $\langle -\ln T \rangle$ grows linearly with L, Lévy disorder induces an α dependence in $\langle -\ln T \rangle$ for $0 < \alpha < 1$. It is important to mention that, even though $\langle -\ln T \rangle$ depends linearly on L for $\alpha \geq 1$, the statistical properties are not described by the one-parameter scaling theory. Since the fluctuations in the transmission coefficient are larger than those considered in the Anderson theory. Equation (3.3) has been compared with our numerical simulations and the result is shown in figure 3.2 for four different values of α and three different sets of parameters. Similar figures can be found in the Appendix C.

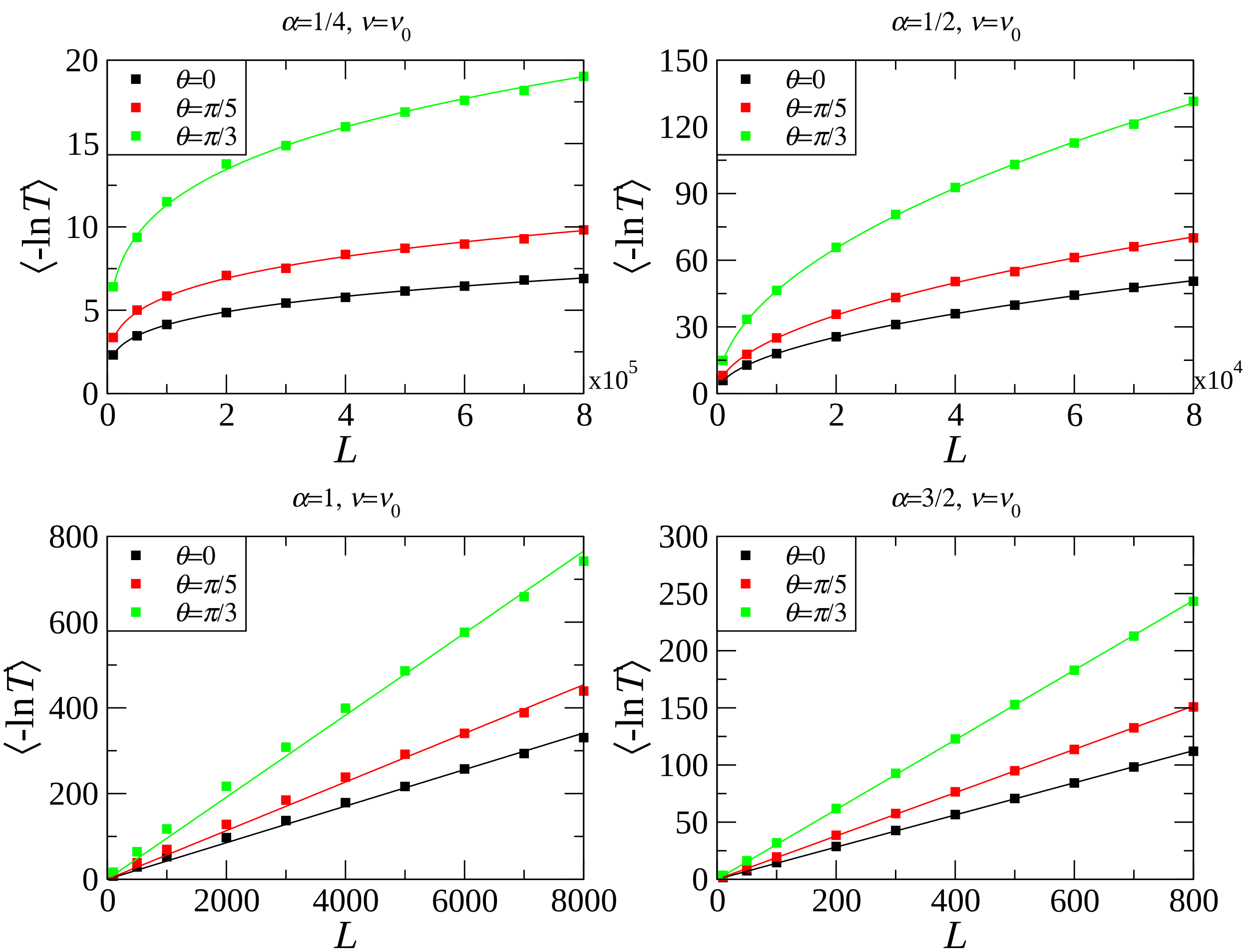

Figure 3.2: The average $\langle -\ln T \rangle$ as a function of the system size L for one-dimensional layered structures conformed by two different media, one inside another (symbols). The thickness of the layers is $l_b = 0.25$ cm while the distance between them is given by the absolute value of a Lévy random variable characterized by α and $\beta = 0$. The parameters are $n_a = 1$, $n_b = \sqrt{4.4}$ and $\nu_0 = 8.5$ GHz. In each panel we keep the frequency constant while the incident angle changes. The solid lines are fittings of the data with Eq. (3.3). Each symbol was calculated using 10^4 ensemble realizations.

Coexistence region

We have to stress that the disorder is introduced to the system by the thickness of the layers which are chosen as random variables. Since we are working on a finite structure of length L the fluctuations in the number of scatterers are large. Thus, in order to find the probability density function for a Lévy-disordered system, these fluctuations must be considered. The final form of the PDF for an ensemble with $\langle -\ln T\rangle = \xi$ was found in [6] and can be written as

$$p_\xi(T) = \int_0^\infty p_{s(\alpha,\xi,x)}(T) q_{\alpha,1}(x)\,\mathrm{d}x\,, \tag{3.4}$$

where the dimensionless length is defined as a function of α as $s = \xi/(2x^\alpha I_\alpha)$ with $I_\alpha = 1/2\int_0^\infty x^{-\alpha} q_{\alpha,1}(x)\,\mathrm{d}x$. Also, $q_{\alpha,1}(x)$ represents the PDF of an α-stable distribution supported on the x positive semiaxis and $p_{s(\alpha,\xi,x)}(T)$ is given by equation (2.3).

Average transmission $\langle T\rangle$

First, from equation (3.4) the mean transmission $\langle T\rangle$ can be computed as a function of the system length L. The behavior of $\langle T\rangle$ has been studied before in [8] where it has been found that

$$\langle T\rangle \propto L^{-\alpha} \qquad \text{for} \qquad 0 < \alpha < 1. \tag{3.5}$$

A comparison of this equation with numerical simulations is shown in figure 3.3 for two different values of α. Also, equation (3.5) can be contrasted with the exponential decay of $\langle T\rangle$ with L for the standard Anderson localization.

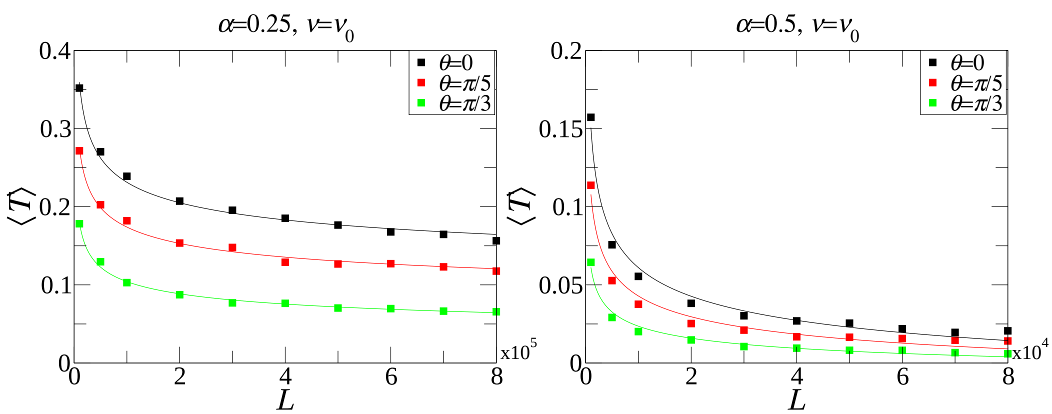

Figure 3.3: The average $\langle T\rangle$ as a function of the system size L for one-dimensional layered structures conformed by two different media, one inside another (symbols). The thickness of the layers is $l_b = 0.25$ cm while the distance between them is given by the absolute value of a Lévy random variable characterized by α and $\beta = 0$. The parameters are $n_a = 1$, $n_b = \sqrt{4.4}$ and $\nu_0 = 8.5$ GHz. In each panel we keep the frequency constant while the incident angle changes. The solid lines are fittings of the data with Eq. (3.5). Each symbol was calculated using 10^4 ensemble realizations.

Transmission distribution

Finally, one can compute the complete distribution of T where the integral (3.4) must be evaluated numerically. Notice that equation (3.4) only depends on ξ and α. In figure 3.4 we present a comparison between the theoretical result and numerical simulations for two different values of α. Also, insets show the transmission distribution for the Anderson localization problem with the value of $\langle -\ln T\rangle$.

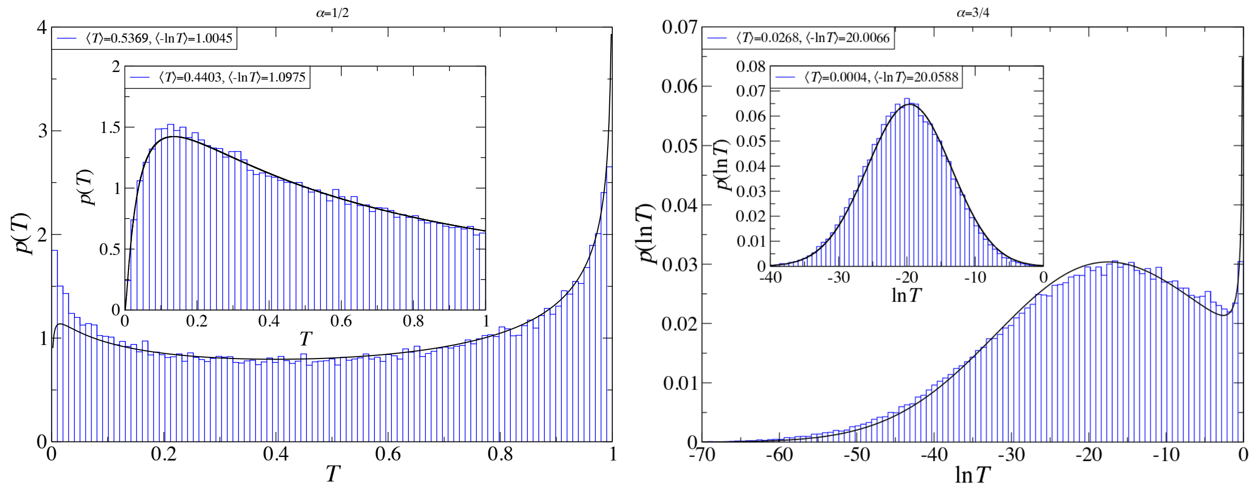

Figure 3.4: The probability density functions $p(T)$ [left] and $p(\ln T)$ [right] for one-dimensional layered structures conformed by two different media, one inside another (histograms). The thickness of the layers is $l_b = 0.05$ cm [left] and $l_b = 0.5$ cm [right] while the distance between them is given by the absolute value of a Lévy random variable characterized by $\alpha = 1/2$ [left], $\alpha = 3/4$ [right] and $\beta = 0$. The parameters are $n_a = 1.4$, $n_b = \sqrt{4.4}$, $\nu = 7.5$ GHz and $\theta = 0$. Both, $\langle T\rangle$ and $\langle -\ln T\rangle$, are shown in each panel in order to identify the transport regime. The solid black line is the theoretical prediction (3.4) with $p_s(T)$ the PDF (2.3). Inset: The probability density functions $p(T)$ [left] and $p(\ln T)$ [right] for one-dimensional layered structures conformed by two different media (histograms). The thickness of each layer is given by the absolute value of a Gaussian random variable characterized by $\mu = 0$ and $\sigma = 1$. The parameters are $n_a = 1.4$, $n_b = 2.4$, $\nu = 7.5$ GHz and $\theta = 0$. The solid black line is the theoretical prediction (2.3). Each histogram was calculated using 10^5 ensemble realizations. A good agreement between theory and numerical simulations is observed.

Note that the PDF in the left panel of Fig.3.4 shows two peaks at $T \sim 0$ and $T \sim 1$. This behavior is related to the coexistence of ballistic and localized regimes. From the right panel, it can be seen that the log-normal behavior of $p(\ln T)$ characteristic of the Anderson localization in the localized regime does not appear anymore for Lévy-type disorder *i.e.* the distribution of the logarithm of the transmission is not a Gaussian. More figures are available in Appendix C. This numerical result has been implemented experimentally and it is discussed in [10].

Delay time

Since the thickness of the layers in the multilayer structure we consider is given as a Lévy random variable, the fluctuations in the number of scatterers in each structure of length L are large. Then, systems with a small number of scatterers can be found with a larger probability than in the standard disorder problem. To show how the delay times are affected by Lévy disorder, figure 3.5 shows a comparison of delay time PDFs of structures with standard disorder and Levy-type disorder using two different values of α. The average $\langle -\ln T\rangle$ has been kept constant for the three numerical simulations shown in figure 3.5.

Notice the PDFs of delay times corresponding to Lévy structures (red and green histograms) present long tails as compared to the PDFs of delay times for structures with standard disorder (blue histograms) for the same $\langle -\ln T \rangle$. Due to the coexistence of the ballistic and localized regimes in Lévy disordered systems, long tails can be interpreted as a consequence of the delocalization of the wave. Also, from the upper panels of figure 3.5, it is observed that τ_R and $\tau_{R'}$ are not statistically identical for the Lévy disordered structures. The differences in the statistics of τ_R and $\tau_{R'}$ in Lévy-disordered structures (red and green histograms) can be contrasted with the Anderson case (blue histogram) where τ_R and $\tau_{R'}$ are identically distributed.

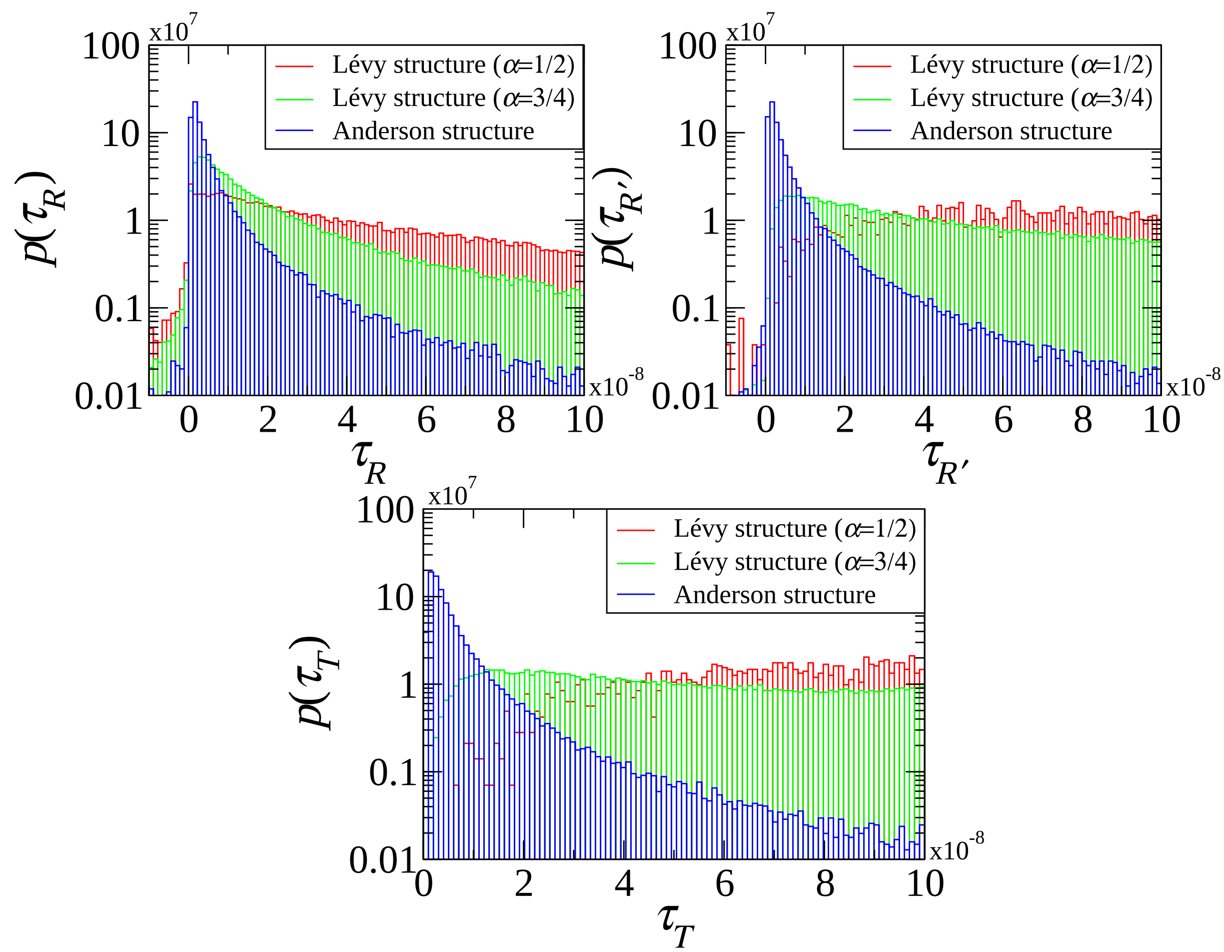

Figure 3.5: The probability density function $p(\tau_R)$ [upper left], $p(\tau'_R)$ [upper right] and $p(\tau_T)$ [lower] for one-dimensional layered structures conformed by two different media, one inside another (histograms). The thickness of the layers is $l_b = 0.25$ cm while the distance between them is given by the absolute value of a Lévy random variable characterized by $\alpha = 1/2$ (red histogram), $\alpha = 3/4$ (green histogram) and $\beta = 0$ and by the absolute value of a Gaussian random variable characterized by $\mu = 0$ and $\sigma = 1$ (blue histogram). The parameters are $n_a = 1.4$, $n_b = \sqrt{4.4}$, $\nu = 7.5$ GHz, $\theta = 0$ and $\langle -\ln T \rangle \sim 10$. Each histogram was calculated using 10^5 ensemble realizations.

Inhomogeneity of the system

In order to understand the statistical differences between τ_R and $\tau_{R'}$ in Lévy disordered systems, we have to call the concept of homogeneity. Numerically, Lévy structures are constructed by adding layers from the left. Since the probability of obtaining a large random number from the random generator is lower than the probability to obtain a small number, the left side of the system has a larger density of scatterers as compared to the right side. As a consequence, a wave coming from the right penetrates deeper than a wave coming from the left. In other words, the left incoming wave is reflected before the right traveling wave producing the statistical differences between the reflection delay times. Notice that an important part of the scattering process takes place near the edges of the waveguide. We have called these structures as *inhomogeneous*.

"*Homogeneous*"[1] structures can be constructed looking for the "equilibrium" in the number of scatterers, especially close to the borders of the structures. Numerically, two inhomogeneous independent systems are grown, one from the left and the other from the right. Later, both structures are coupled by the side which is supposed to have the lowest density of scatterers. Then, the final structure is expected to contain a similar density of layers close to the edges. A comparison between homogeneous and inhomogeneous systems is shown in figure 3.6 for $\alpha = 1/2$ where $\langle -\ln T\rangle$ is constant for both ensembles. The $\alpha = 3/4$ case as well as figure 3.5 corresponding to the homogeneous problem are included in Appendix C.

Figure 3.6 shows that delay times are sensitive to the internal structure. As we have commented before, the differences between τ_R and $\tau_{R'}$ are tuned by how deeper the wave penetrates inside the system. Also, from figure 3.6, it is observed that the differences in the statistics of reflection delay times vanish by constructing structures whose density of scatterers is homogeneous near the borders, even if the structure is not completely homogeneous. The differences in the statistics of both structures are more notable looking at the random variables $\tau_{R'}$ and τ_T. For the statistics of τ_R, it can be seen that inhomogeneous structures present a faster decay with respect to the "homogeneous" systems.

The density of layers can produce other interesting phenomena. Figure 3.6 shows a local maximum at $\tau_R \sim 1$, $\tau_{R'} \sim 1$ and $\tau_T \sim 1/2$ for the "homogeneous" case. The position of these peaks has been identified numerically in terms of the parameters of the system as

$$\tau_{R,\max} = \frac{2L}{v_g}, \qquad \tau_{R',\max} = \frac{2L}{v_g} \qquad \text{and} \qquad \tau_{T,\max} = \frac{L}{v_g},$$

for reflection and transmission delay times, respectively. Notice that delay times in figure 3.6 have been normalized using the value of $\tau_{R,\max}$. The normalization sets the maximum to 1 for the reflection delay times as well as to 1/2 for the transmission delay times. The localization of this peak is related to the finite size of the structure. For τ_R and $\tau_{R'}$, the peak is given by the waves which are reflected by the last scatterers on the opposite side to the incident side. On the other hand, $\tau_{T,\max}$ measures the time that a wave takes to cross the structure without being scattered. In fact, $\tau_{R,m} = 2\tau_{T,\max}$ because the wave crosses the system twice if it is reflected by the last scatterers while the transmission delay time measures the time a wave takes to cross the system and is transmitted to the other side. Notice that the PDFs of τ_R for inhomogeneous structures do not show this peak due to the low density of scatterers on the opposite side of the structure.

[1]Despite we called these structures as "homogeneous", this kind of structures are not completely homogeneous due to the Lévy disorder.

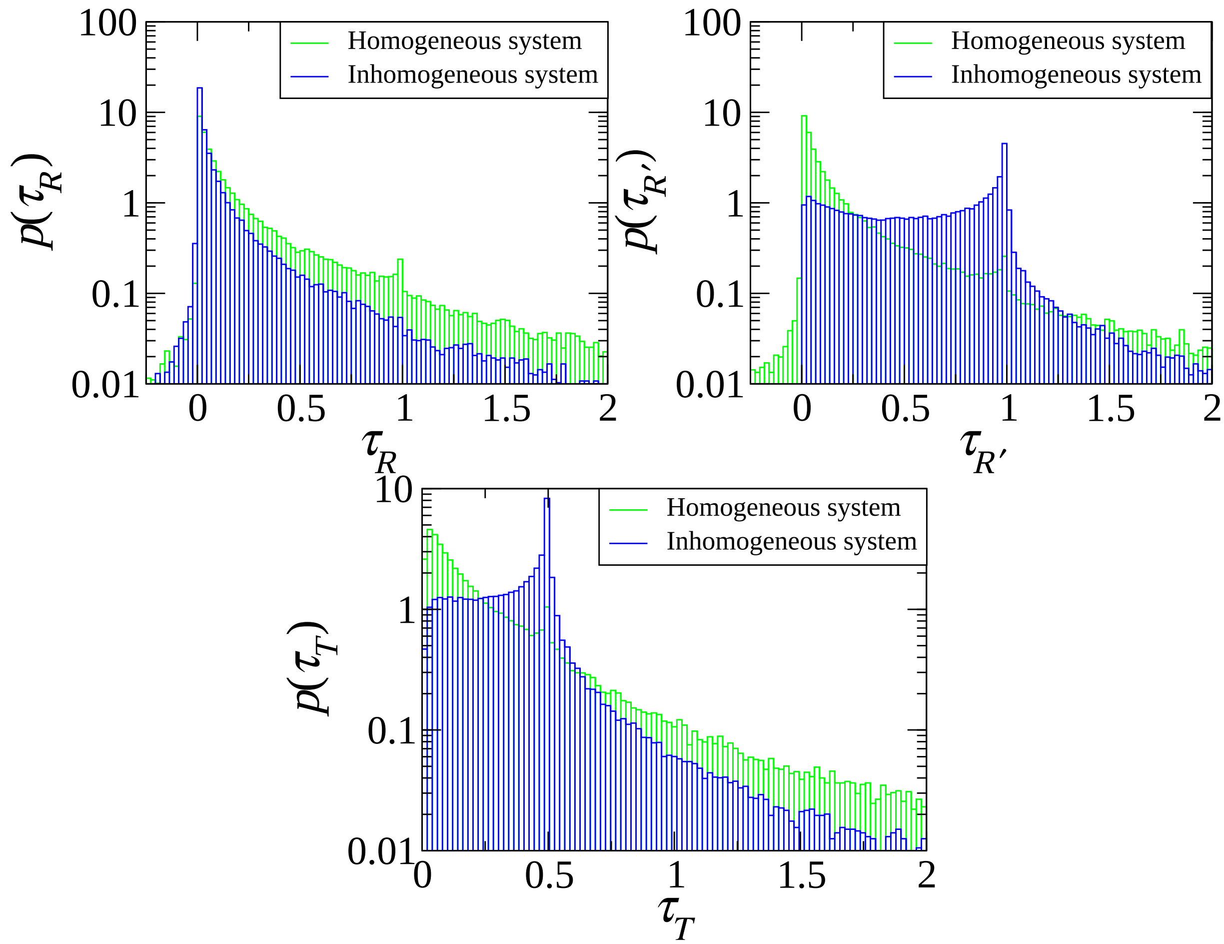

Figure 3.6: The probability density function $p(\tau_R)$ [upper left], $p(\tau'_R)$ [upper right] and $p(\tau_T)$ [lower] for one-dimensional layered structures conformed by two different media, one inside another (histograms). The thickness of the layers is $l_b = 0.25$ cm while the distance between them is given by the absolute value of a Lévy random variable characterized by $\alpha = 1/2$ and $\beta = 0$ for both systems, homogeneous (green histograms) and inhomogeneous (blue histograms). The parameters are $n_a = 1.4$, $n_b = \sqrt{4.4}$, $\nu = 7.5$ GHz, $\theta = 0$ and $\langle -\ln T\rangle \sim 10$. Each histogram was calculated using 10^5 ensemble realizations.

Homogeneous disorder

In order to describe the behavior of the probability density function of the delay times in Lévy structures, an expression similar to (3.4) can be used. We write

$$p_\xi(\tau_R) = \int_0^\infty p_s(\tau_R) q_{\alpha,1}(x)\, \mathrm{d}x\,, \tag{3.6}$$

where the dimensionless length has the form $s = \xi/(2x^\alpha I_\alpha)$ with I_a defined by $I_\alpha = 1/2\int_0^\infty x^{-\alpha} q_{\alpha,1}(x)\,\mathrm{d}x$ and $\xi = \langle -\ln T\rangle$. Also, $q_{\alpha,1}(x)$ represents the probability density function of an α-stable distribution supported on the positive semiaxis and $p_s(\tau_R)$ is the distribution for the reflection delay time in the Anderson case.

As we have seen, the coexistence of the ballistic and localized regimes in Lévy-disordered systems produces anomalous localization of the waves. This crossover region in Lévy disordered structures is the reason to use $p_s(\tau_R)$ as the distribution (2.18) in order to find the PDF of delay times. First, distribution (2.18) must be written in terms of the dimensionless length which is a function of the variable of integration x. Then, making the change of variable $\tau_R/\tau_0 \Rightarrow \tau_R$ and putting γ in terms of the dimensionless length s, distribution (2.18) can be written as

$$p(\tau_R) = \frac{1}{2 - \mathrm{e}^{-a/s}} \frac{a}{s} \frac{1}{\tau_R^2} \mathrm{e}^{-\frac{a}{s}\left|\frac{1}{\tau_R} - 1\right|}, \tag{3.7}$$

where a is a fitting constant. Notice that distribution (2.19) is obtained from (3.7) with $a = 2$. Finally, the integral (3.6) is solved numerically and it is shown in comparison with numerical simulations in figure 3.7. Also, the statistics corresponding to $\tau_{R'}$ for $\alpha = 1/2$ and the statistics of τ_R, $\tau_{R'}$ and τ_T for $\alpha = 3/4$ are shown in Appendix C.

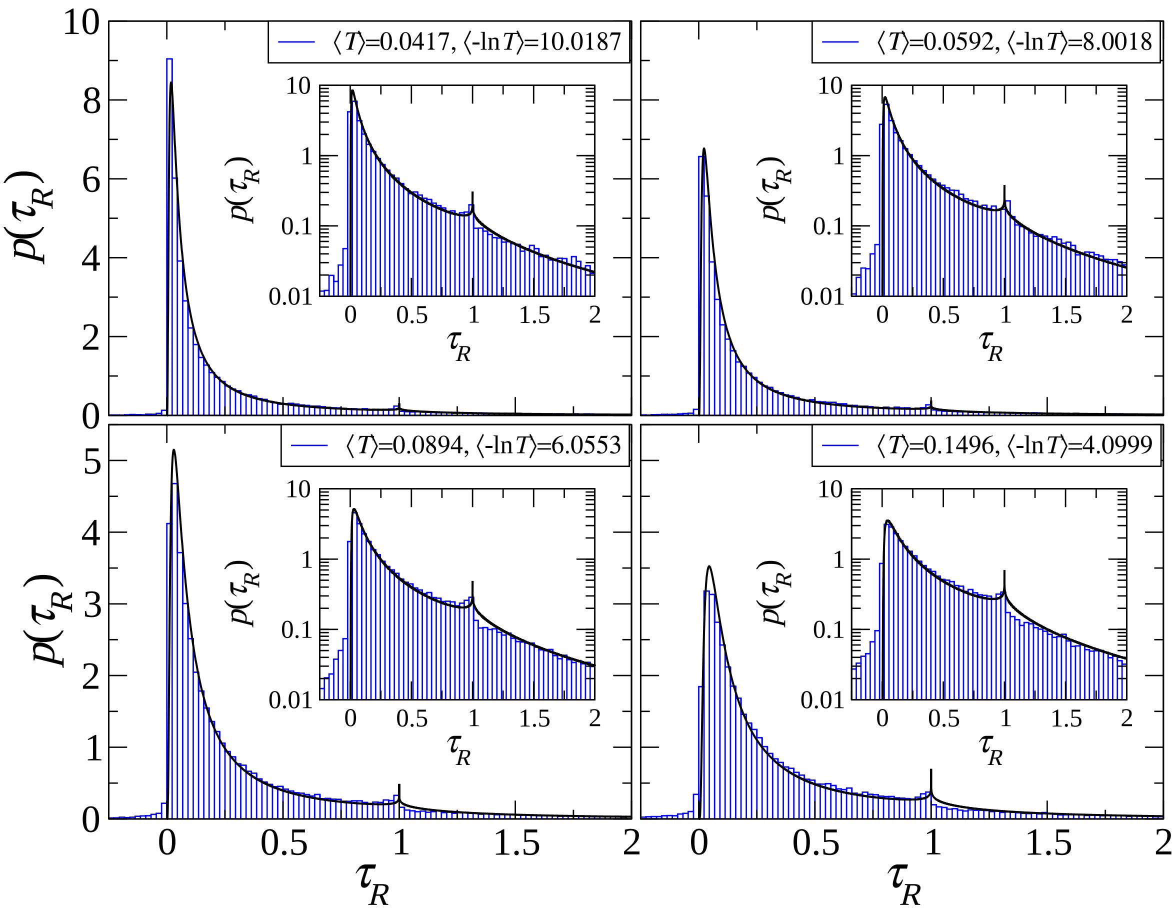

Figure 3.7: The probability density function $p(\tau_R)$ for one-dimensional layered structures conformed by two different media, one inside another (histograms). The thickness of the layers is $l_b = 0.25$ cm while the distance between them is given by the absolute value of a Lévy random variable characterized by $\alpha = 1/2$ and $\beta = 0$. The parameters are $n_a = 1$, $n_b = \sqrt{4.4}$, $\nu = 7.5$ GHz and $\theta = 0$. Both, $\langle T \rangle$ and $\langle -\ln T \rangle$, are shown in each panel in order to identify the transport regime. The inset of each panel presents the same histogram of the main panel in semi-log scale. The solid black line is the theoretical prediction (3.6) with $p_s(\tau_R)$ the PDF (3.7) and $a = \alpha$. Each histogram was calculated using 10^5 ensemble realizations. A good agreement between theory and numerical simulation is observed. Here, we considered the change of variable $v_g\tau_R/2L \Rightarrow \tau_R$.

From figure 3.7, it is observed that the distribution (3.6) with p_s as (3.7) is in good agreement with the numerical simulations. An important result lies on the value of a used to obtain all theoretical curves in figure 3.7, being identified numerically as $a = \alpha$. So that, the statistical properties are completely determined by $\langle -\ln T \rangle$ and α again. With this information, we can perform any theoretical prediction without free parameters.

Now, in order to understand how the average of the delay time changes with the length of the system, numerical simulations have been performed. This comparison can be observed in figure 3.8 considering two different values of α.

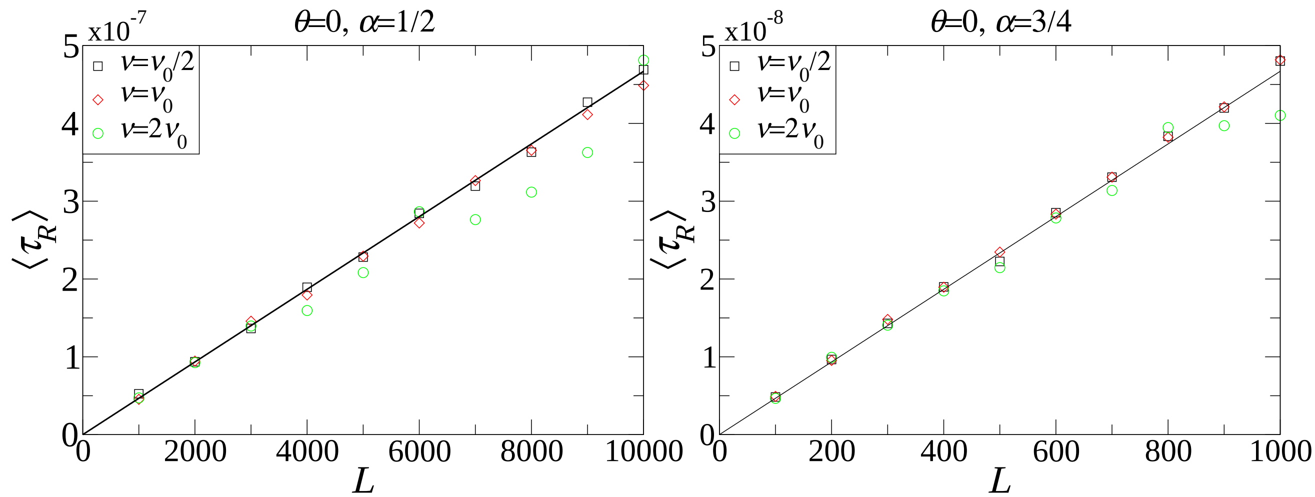

Figure 3.8: The average $\langle \tau_R \rangle$ as a function of the system size L for one-dimensional layered structures conformed by two different media, one inside another (symbols). The thickness of the layers is $l_b = 0.25$ cm while the distance between them is given by the absolute value of a Lévy random variable characterized by $\alpha = 1/2$ [left], $\alpha = 3/4$ [right] and $\beta = 0$. The parameters are $n_a = 1.4$, $n_b = \sqrt{4.4}$, $\nu_0 = 7.5$ GHz and $\theta = 0$. We keep the incident angle constant while the frequency changes. The solid lines are given by Eq. (3.8). Each symbol was calculated using 2×10^4 ensemble realizations. This graph does not contain any normalization over τ_R.

From figure 3.8, we can observe that the average of the reflection delay time depends linearly on L. The constant of proportionality has been identified numerically. Then, we can write

$$\langle \tau_R \rangle = \frac{L}{v_g}, \tag{3.8}$$

where v_g is the group velocity. Equation (3.8) can be interpreted as the time a wave takes to reach the middle of the structure a come back to the incoming edge. In addition to this, the mean of the delay time does not depend on the energy as in the standard Anderson localization. The corresponding figure for $p(\tau_{R'})$ can be found in Appendix C.

Moreover, the PDF of Lévy delay times for transmission can be obtained from equation (2.12). Now, (3.6) is introduced in (2.12) and the integral is solved numerically. The comparison between numerical simulations and the theoretical prediction can be observed in figure 3.9.

Even though the statistics of τ_R are well described by equation (3.6) using (3.7), the numerical simulations for transmission delay times present some discrepancies with respect to the theoretical

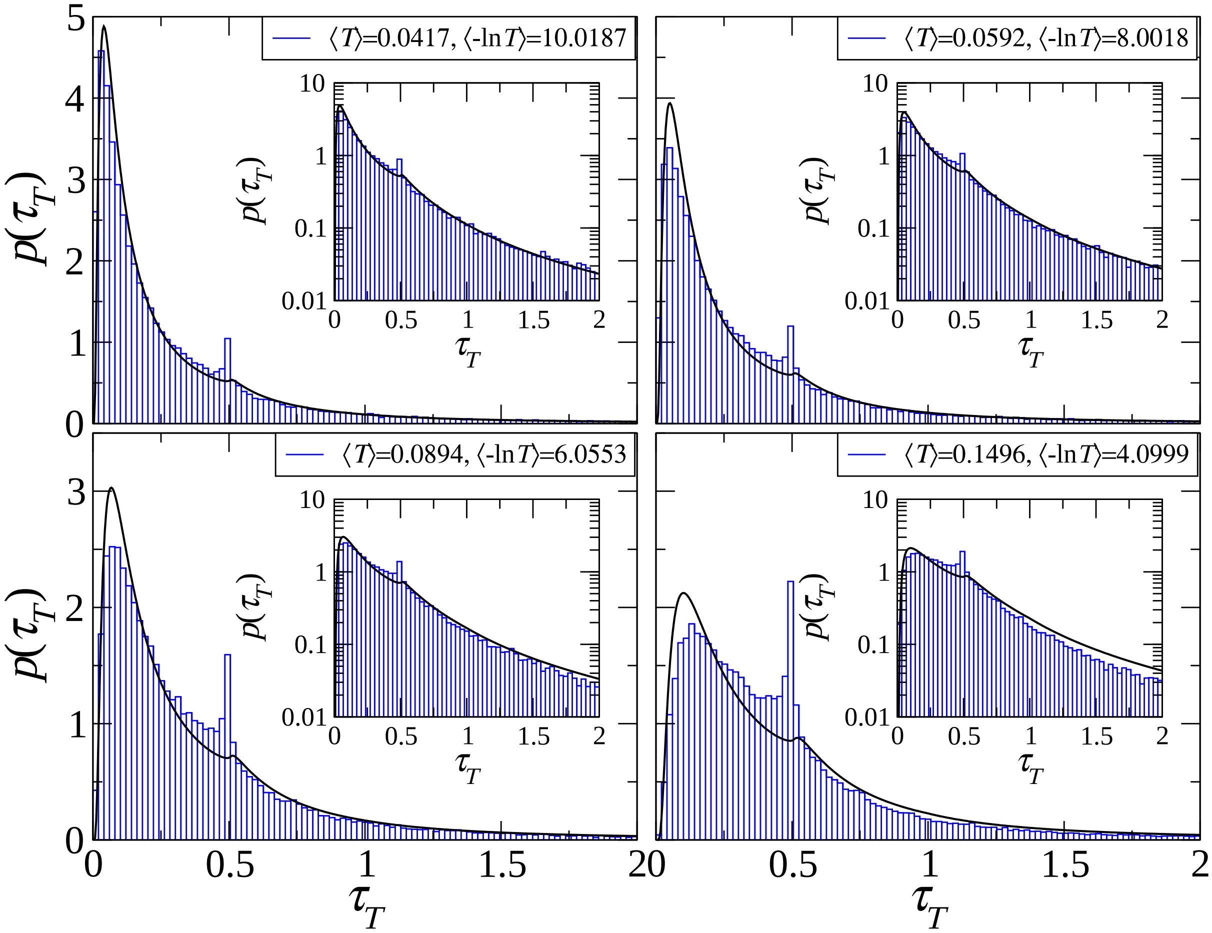

Figure 3.9: The probability density function $p(\tau_T)$ for one-dimensional layered structures conformed by two different media, one inside another (histograms). The thickness of the layers is $l_b = 0.25$ cm while the distance between them is given by the absolute value of a Lévy random variable characterized by $\alpha = 1/2$ and $\beta = 0$. The parameters are $n_a = 1$, $n_b = \sqrt{4.4}$, $\nu = 7.5$ GHz and $\theta = 0$. Both, $\langle T \rangle$ and $\langle -\ln T \rangle$, are shown in each panel in order to identify the transport regime. The inset of each panel presents the same histogram of the main panel in semi-log scale. The solid black line is the theoretical prediction (2.12) with $p(\tau_R)$ and $p(\tau_{R'})$ the PDF (3.6) considering $p_s(\tau_R)$ and $p_s(\tau_{R'})$ as (3.7) and $a = \alpha$. Each histogram was calculated using 10^5 ensemble realizations. A good agreement between theory and numerical simulation is observed. Here, we considered the change of variable $v_g\tau_T/2L \Rightarrow \tau_T$.

prediction. Since Lévy structures can induce a strong interaction between the wave which comes from the left and the wave coming from the right equation (2.12) does not hold. This effect is shown in the lower panels of figure 3.9, where the theoretical prediction is not working regardless of the reflection delay times, which is perfectly described by our theoretical model. This effect is due to the finite size of the structure although, the behavior of the tail shows a good agreement between numerical simulations and theoretical prediction.

Since we are working with "homogeneous" structures the behavior of the average of the transmission delay time can be obtained from (2.9) and (3.8). Then, we have

$$\langle \tau_T \rangle = \frac{L}{v_g}, \tag{3.9}$$

which can be interpreted as the time that a wave takes to cross a structure of length L. Equation (3.9) is shown in comparison with numerical simulations in figure 3.10 where a good agreement is observed.

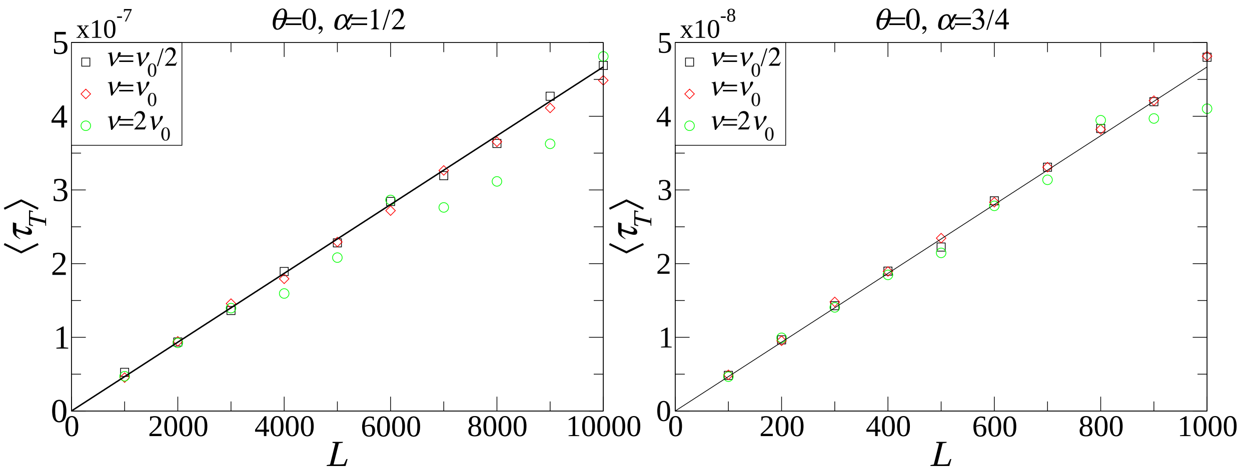

Figure 3.10: The average $\langle \tau_T \rangle$ as a function of the system size L for one-dimensional layered structures conformed by two different media, one inside another (symbols). The thickness of the layers is $l_b = 0.25$ cm while the distance between them is given by the absolute value of a Lévy random variable characterized by $\alpha = 1/2$ [left], $\alpha = 3/4$ [right] and $\beta = 0$. The parameters are $n_a = 1.4$, $n_b = \sqrt{4.4}$, $\nu_0 = 7.5$ GHz and $\theta = 0$. We keep the incident angle constant while the frequency changes. The solid lines are given by Eq. (3.9). Each symbol was calculated using 2×10^4 ensemble realizations. This graph does not contain any normalization over τ_T.

Inhomogeneous disorder

To approach inhomogeneous disorder, we have to use the distribution (3.6) again. As in the "homogeneous" problem, the integral (3.6) must be numerically solved using the distribution (3.7). As can be seen in the upper left panel of figure 3.6, the decay of the PDFs of the homogeneous and inhomogeneous cases presents a different behavior even though $\langle - \ln T \rangle$ is the same in both cases. This means that the constant a in equation (3.7) cannot be equal to α and it is necessary to determine this constant numerically again.

Figure 3.11 shows a comparison between numerical simulations and equation (3.6) with $p_s(\tau_R)$ given by (3.7). Here, $a = \alpha/3$ was used and a good agreement is obtained in the four cases.

A new problem emerges when trying to explain the statistics of $\tau_{R'}$ for inhomogeneous systems. Here the statistics of delay times $\tau_{R'}$ is completely different from the statistics of τ_R. The statistics of $\tau_{R'}$ is explained by the distribution (3.7) by the proper choice of the fitting constant. The comparison between the theoretical model and numerical simulations for $\tau_{R'}$ can be observed in figure 3.12. A good agreement is observed using the distribution (3.6) with p_s as given by equation (3.7). In this figure, the fitting constant $a = 10\alpha$ was used.

Finally, in order to obtain a theoretical prediction for the transmission delay times, we use equation (2.12). The comparison between numerical simulations and theoretical prediction is shown in

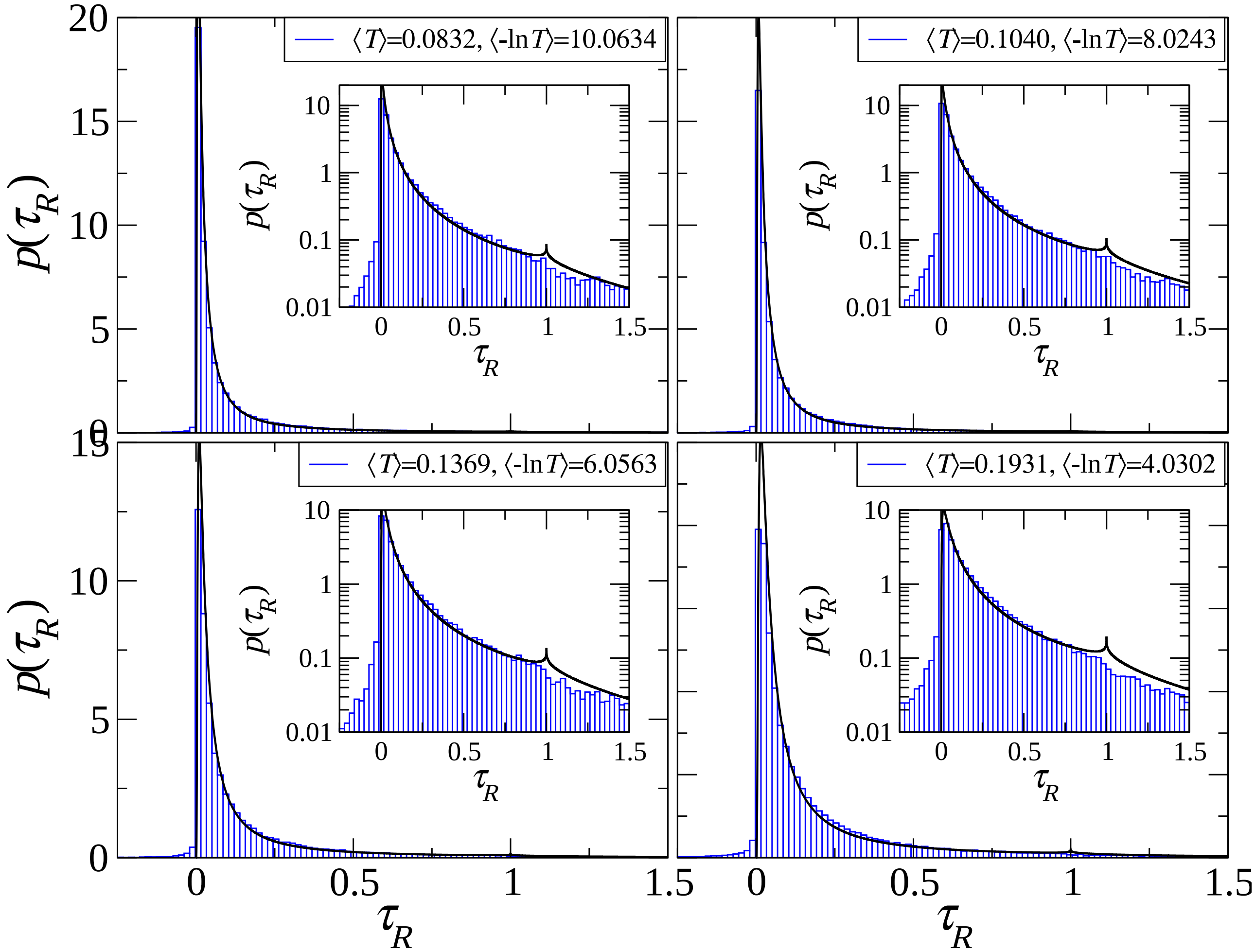

Figure 3.11: The probability density function $p(\tau_R)$ for one-dimensional layered structures conformed by two different media, one inside another (histograms). The thickness of the layers is $l_b = 0.25$ cm while the distance between them is given by the absolute value of a Lévy random variable characterized by $\alpha = 1/2$ and $\beta = 0$. The parameters are $n_a = 1$, $n_b = \sqrt{4.4}$, $\nu = 7.5$ GHz and $\theta = 0$. Both, $\langle T\rangle$ and $\langle -\ln T\rangle$, are shown in each panel in order to identify the transport regime. The inset of each panel presents the same histogram of the main panel in semi-log scale. The solid black line is the theoretical prediction (3.6) with $p_s(\tau_R)$ the PDF (3.7) and $a = \alpha/3$. Each histogram was calculated using 10^5 ensemble realizations. A good agreement between theory and numerical simulation is observed. Here, we considered the change of variable $v_g\tau_R/2L \Rightarrow \tau_R$.

figure 3.13 for different values of $\xi = \langle -\ln T\rangle$. We recall that the theoretical curves given by (2.12) depend on the statistics of τ_R and $\tau_{R'}$ so that they are not expected to describe well the numerical data, however, a good agreement is observed in figure 3.13.

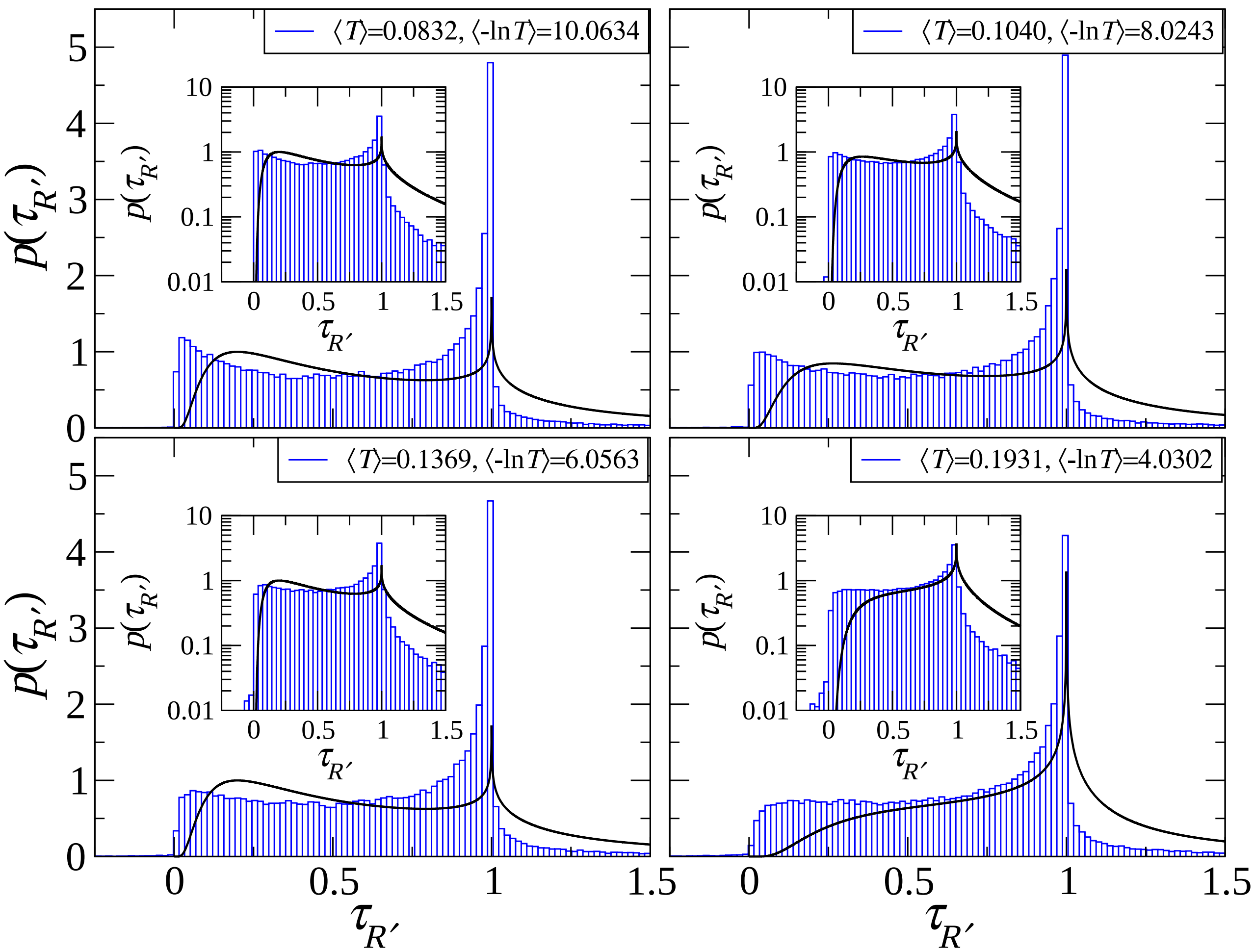

Figure 3.12: The probability density function $p(\tau_{R'})$ for one-dimensional layered structures conformed by two different media, one inside another (histograms). The thickness of the layers is $l_b = 0.25$ cm while the distance between them is given by the absolute value of a Lévy random variable characterized by $\alpha = 1/2$ and $\beta = 0$. The parameters are $n_a = 1$, $n_b = \sqrt{4.4}$, $\nu = 7.5$ GHz and $\theta = 0$. Both, $\langle T \rangle$ and $\langle -\ln T \rangle$, are shown in each panel in order to identify the transport regime. The inset of each panel presents the same histogram of the main panel in semi-log scale. The solid black line is the theoretical prediction (3.6) with $p_s(\tau_R)$ the PDF (3.7) and $a = 10\alpha$. Each histogram was calculated using 10^5 ensemble realizations. A good agreement between theory and numerical simulation is observed. Here, we considered the change of variable $v_g \tau_{R'}/2L \Rightarrow \tau_{R'}$.

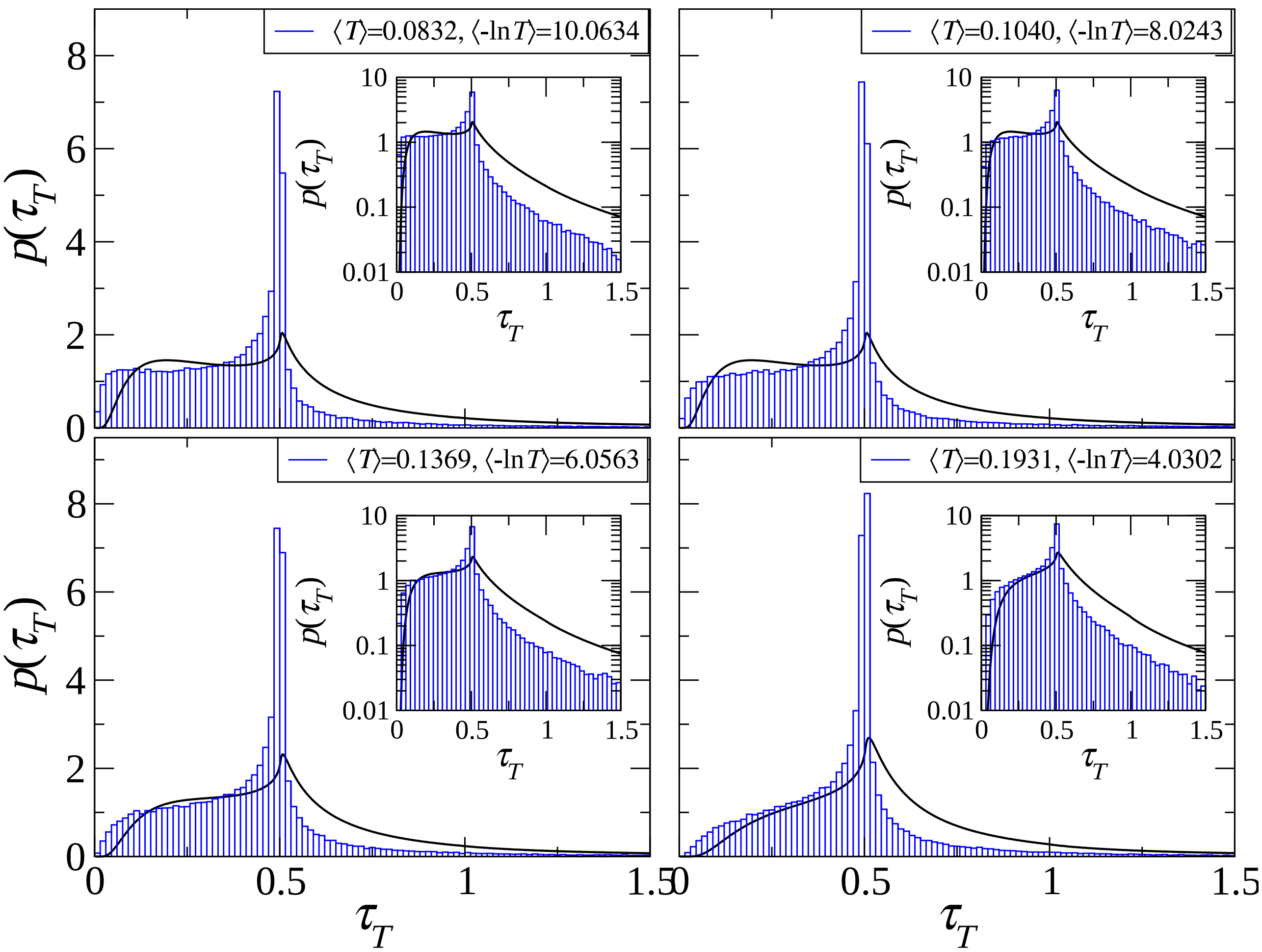

Figure 3.13: The probability density function $p(\tau_T)$ for one-dimensional layered structures conformed by two different media, one inside another (histograms). The thickness of the layers is $l_b = 0.25$ cm while the distance between them is given by the absolute value of a Lévy random variable characterized by $\alpha = 1/2$ and $\beta = 0$. The parameters are $n_a = 1$, $n_b = \sqrt{4.4}$, $\nu = 7.5$ GHz and $\theta = 0$. Both, $\langle T \rangle$ and $\langle -\ln T \rangle$, are shown in each panel in order to identify the transport regime. The inset of each panel presents the same histogram of the main panel in semi-log scale. The solid black line is the theoretical prediction (2.12) with $p(\tau_R)$ and $p(\tau_{R'})$ the PDF (3.6) considering $p_s(\tau_R)$ and $p_s(\tau_{R'})$ as (3.7) with $a = \alpha/3$ and $a = 10\alpha$, respectively. Each histogram was calculated using 10^5 ensemble realizations. A good agreement between theory and numerical simulation is observed. Here, we considered the change of variable $v_g \tau_T / 2L \Rightarrow \tau_T$.

4

Experimental results

Una teoría debe ser despiadada
y se vuelve contra su creador si el creador
no se trata a si mismo con crueldad.

Querer explicar los hechos del espíritu
mediante geodésicas es como pretender
extirpar una angustia con tenazas de dentista.

La gente quiere que le expliquen la pesadilla.
Pero el sueño expresa una realidad de la única
manera en que esa realidad puede expresarse.
Ernesto Sábato (Abbadon: el exterminador)

Abstract

In this chapter, the results obtained in the previous chapters are compared with experimental measurements. First, the experimental setup and the details of the experiment are presented. Then, the comparison between theoretical and experimental delay times is discussed.

Photonic experiment

For Lévy disordered systems, the first experiments were performed by Barthelemy *et al.* [4] using photonic structures named *Lévy glasses*. Those experiments allowed the observation of anomalous localization against Anderson localization. Later, a photonic waveguide was constructed by Fernandez *et al.* [10] and equation (3.4) was proved experimentally for the transmission problem. From the experiment performed by Fernandez *et al.* it is possible to extract measurements of the delay times in Lévy disordered systems. The details of this experiment will be presented bellow.

Experimental setup

The experimental setup consists of a Vector Network Analyzer (R&S®ZVA 24), two standard microwave X-band transitions and an aluminum waveguide of 2 meters length. Inside the waveguide, a set of independent, mobile, dielectric scatterers are placed randomly in three different ways: following a Lévy random variable characterized by $\alpha = 1/2$ and $\alpha = 3/4$ and following a Gaussian random variable characterized by $\mu = 1$ and $\sigma = 0$. Each layer has a complex refraction index of $n = \sqrt{4.4} + \delta\mathrm{i}$ and a thickness of 0.25 cm. Notice that the complex nature of n produces absorption in each slab. Experimentally, the system is built by adding slabs from the left, which results in an inhomogeneous structure. A diagram and a picture of the experimental waveguide are shown in figure 4.1.

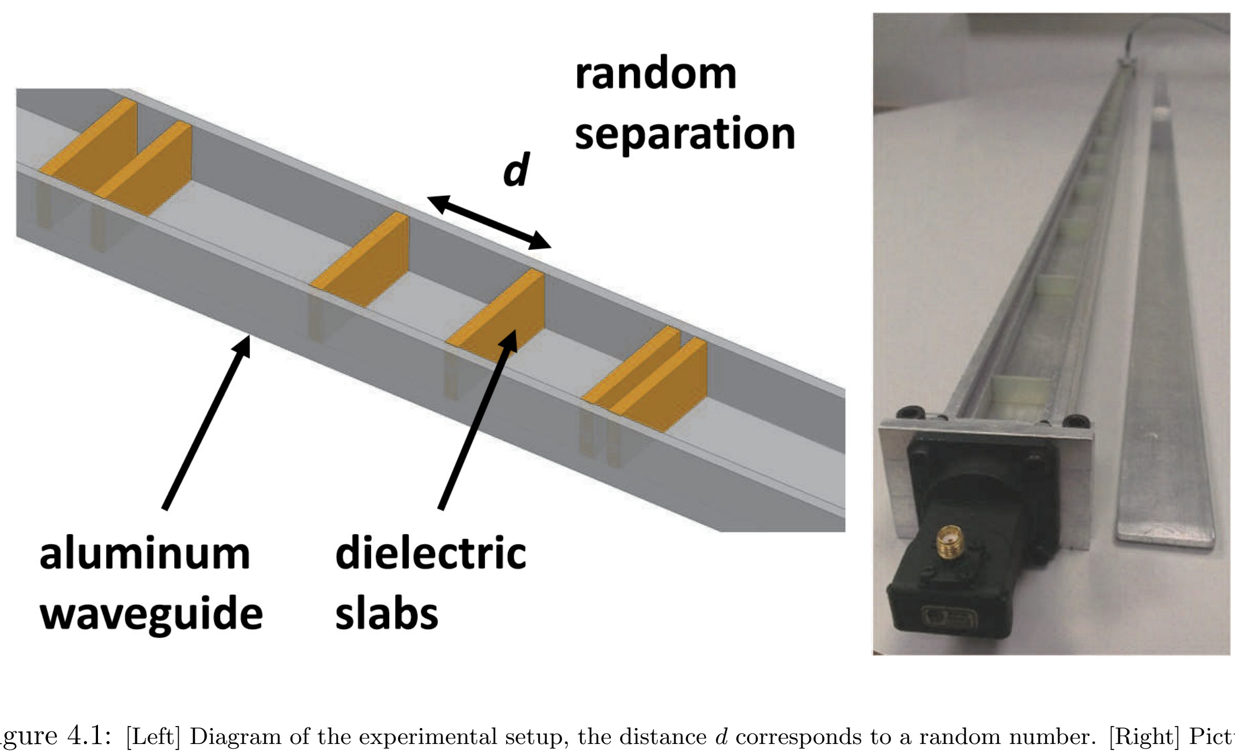

Figure 4.1: [Left] Diagram of the experimental setup, the distance d corresponds to a random number. [Right] Picture of the experimental waveguide. Image taken from [10].

The VNA is equipment using to measure electric networks. Its frequency range goes from 10 MHz to 24 GHz with a resolution of 1 Hz. Experimentally, the VNA generates a signal of frequency ν

and sends it to one of the X-band transitions. Each transition is placed at one of the edges of the waveguide. The wave is induced in the system by the transition and measure by the VNA by means of the second transition in the opposite side of the waveguide. Experimentally, the angle of incidence of the induced wave is $\theta = 0$, as well as the electric field is perpendicular to the surface of the slabs. From the experiment, the components of the scattering matrix were measured. That allows finding the delay times from the definition [14, 23]

$$\tau_R = \frac{\mathrm{d}\eta}{\mathrm{d}\omega},$$

to contrast them with the theoretical model and numerical simulations. Here, η represents the phase shift of the reflection amplitude.

Frequency range

Each ensemble is composed of 135 waveguide realizations obtained by means of moving the dielectric slabs. Each element of the ensemble is measured over a wide frequency range from 8 to 12 GHz with steps of 0.01 GHz. As a consequence, $\langle -\ln T\rangle$ is different for each frequency. Then, a frequency or a range of frequencies must be selected in order to generate a comparison between the theoretical model and numerical simulations. The average $\langle -\ln T\rangle$ as a function of the linear frequency ν are shown in figure 4.2 (black line) for two values of α and the Gaussian case. Also, figure 4.2 presents the selected frequency window (red line).

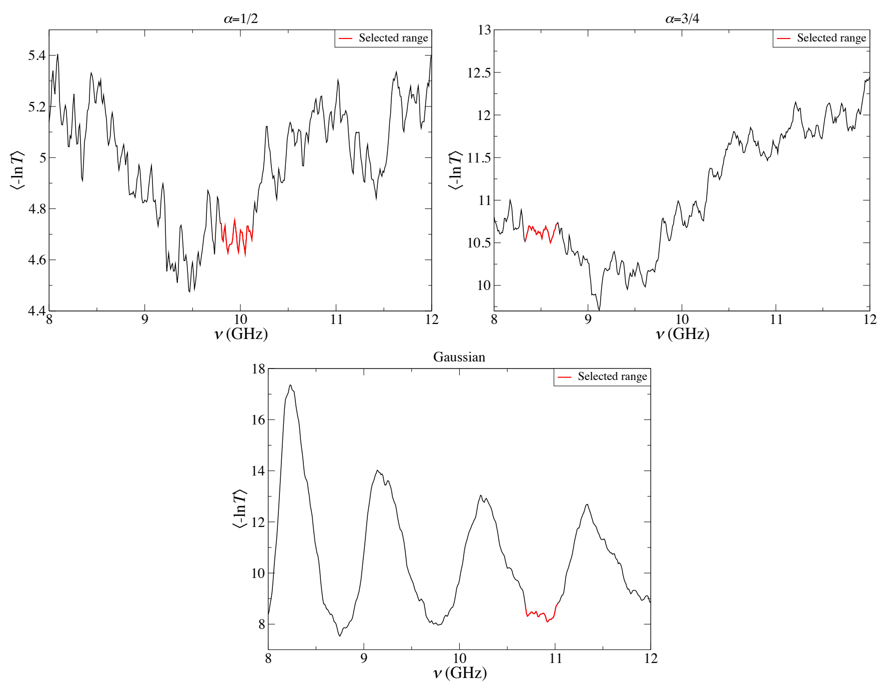

Figure 4.2: The average $\langle -\ln T\rangle$ as a function of the frequency ν in the measured frequency range for the experimental system (black line). The red line is the selected frequency range in each case. For Lévy disorder, we considered two values of α: $\alpha = 1/2$ [upper left] and $\alpha = 3/4$ [upper right]. Also, we considered Gaussian disorder [lower panel].

The center of the chosen frequency windows are: $\nu = 9.96$, $\nu = 8.5$ and $\nu = 10.86$ GHz for the $\alpha = 1/2$, $\alpha = 3/4$ and Gaussian cases, respectively. The corresponding values of $\langle -\ln T\rangle$ are: $\langle -\ln T\rangle = 4.69$, $\langle -\ln T\rangle = 10.62$ and $\langle -\ln T\rangle = 8.3888$ for the $\alpha = 1/2$, $\alpha = 3/4$ and Gaussian cases, respectively. The width of each frequency window is $\Delta\nu = 0.34$ GHz and it allows taking a total of 4590 delay time measurements.

Results

In figure 4.3, we show three panels with the experimental distributions of τ_R. These panels also show the corresponding numerical simulations and theoretical predictions.

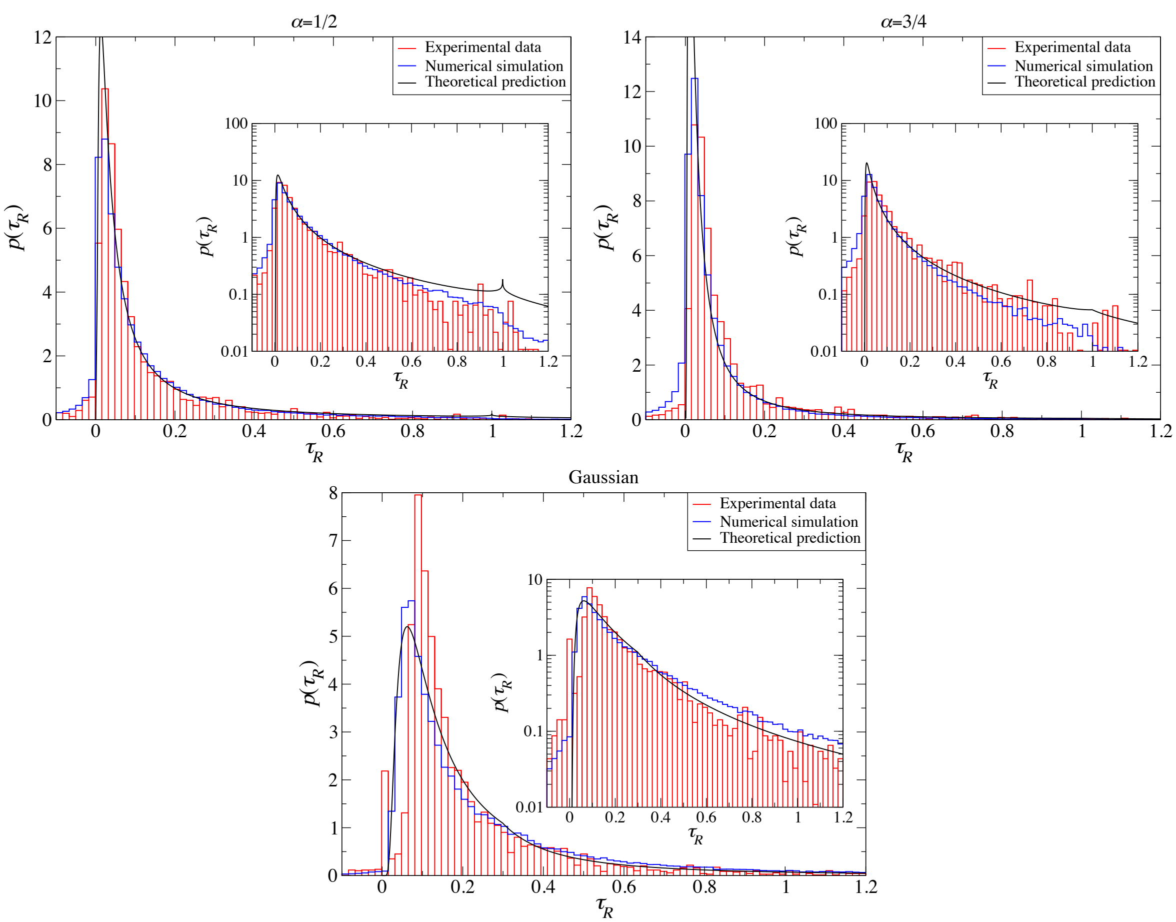

Figure 4.3: The probability density function $p(\tau_R)$ for: the experimental system (red histograms) and numerical simulations for one-dimensional layered structures conformed by two different media, one inside another (blue histograms). The thickness of the layers is $l_b = 0.25$ cm while the distance between them is given by the absolute value of a Lévy random variable characterized by $\alpha = 1/2$ [upper left], $\alpha = 3/4$ [upper right] and a Gaussian random variable characterized by $\mu = 0$ and $\sigma = 1$ [lower]. The parameters are $n_a = 1$, $n_b = \sqrt{4.4} + \delta\mathrm{i}$, $\theta = 0$. Each histogram was calculated using 10^5 ensemble realizations. The inset of each panel presents the same histogram of the main panel in semi-log scale. The solid black line is the theoretical prediction (3.6) with $p_s(\tau_R)$ the PDF (3.7) and $a = \alpha/3$ [upper panels] and the PDF (3.7) [lower panel]. A good agreement between theory, numerical simulation and the experimental data is observed. Here, we considered the change of variable $v_g\tau_R/2L \Rightarrow \tau_R$.

For numerical simulations, the parameters of the experimental system were used. The frequency is chosen as the center of the selected frequency window, the angle of incidence $\theta = 0$, the length $L = 200$ cm and the refraction index $n = \sqrt{4.4} + \delta\mathrm{i}$. Then, the only free parameter in the simulation corresponds to the imaginary part of the reflection index of the slabs. Thus, the characterization of this value was performed. Numerically, the imaginary part of the refraction index is tuned to reach the experimental value of $\langle -\ln T \rangle$. δ was identified as $\delta = 0.0716 \pm 0.044$.

The theoretical predictions for the Lévy-disordered structures were obtained from equation (3.6)

$$p_\xi(\tau_R) = \int_0^\infty p_s(\tau_R) q_{\alpha,1}(x)\,\mathrm{d}x\,,$$

where is $p_s(\tau_R)$ given by Eq. (3.7)

$$p_s(\tau_R) = \frac{1}{2 - \mathrm{e}^{-a/s}} \frac{a}{s} \frac{1}{\tau_R^2} \mathrm{e}^{-\frac{a}{s}\left|\frac{1}{\tau_R} - 1\right|}. \tag{4.1}$$

Here, s is a function of $\xi = \langle -\ln T \rangle$ and has the form $s = \xi / 2 I_\alpha x^\alpha$, where $I_\alpha = 1/2 \int_0^\infty x^{-\alpha} q_{\alpha,1}(x)\,\mathrm{d}x$ and $q_{\alpha,1}(x)$ is the probability density functions of an α-stable distribution supported on the x positive semiaxis. Also, $\xi = \langle -\ln T \rangle$ is given by the experiment. Since we are working on inhomogeneous structures, the fitting constant is different to α and it was numerically identified as $a = \alpha/3$. The theoretical curve for the Gaussian disordered structures was obtained using the distribution (4.1), where the fitting constant a is given by the average of the delay time distribution. Even though a good agreement in the three cases, the discrepancies between the experimental data and the theoretical curves are attributed to the losses by absorption as well as problems of modeling inhomogeneous structures.

Finally, an experimental comparison between delay times in Lévy disordered systems characterized by $\alpha = 3/4$ and the delay times in Gaussian structures was performed. First, we have to select a frequency window where $\langle -\ln T \rangle$ is equal in both systems. A graph of the selected window is shown in the left panel of figure 4.4.

The center of the selected frequency window is $\nu = 11.27$ GHz with a width of $\Delta\nu = 0.14$. The width of this frequency window provides 1890 delay time measurements. Here, $\langle -\ln T \rangle \sim 12$ and $\Delta \langle -\ln T \rangle \sim 1$ GHz.

The probability density function $p(\tau_R)$ is shown in the right panel of figure 4.4. Also, the theoretical predictions are obtained from equation (3.6) with (3.7) as $p_s(\tau_R)$ for the Lévy disordered structures characterized by $\alpha = 3/4$ and by Eq. (2.19) for the Gaussian disorder structures. A good agreement is observed in each case, however, some discrepancies between the histograms and the theoretical curves are observed because of the absorption and problems of modeling the statistics in inhomogeneous structures.

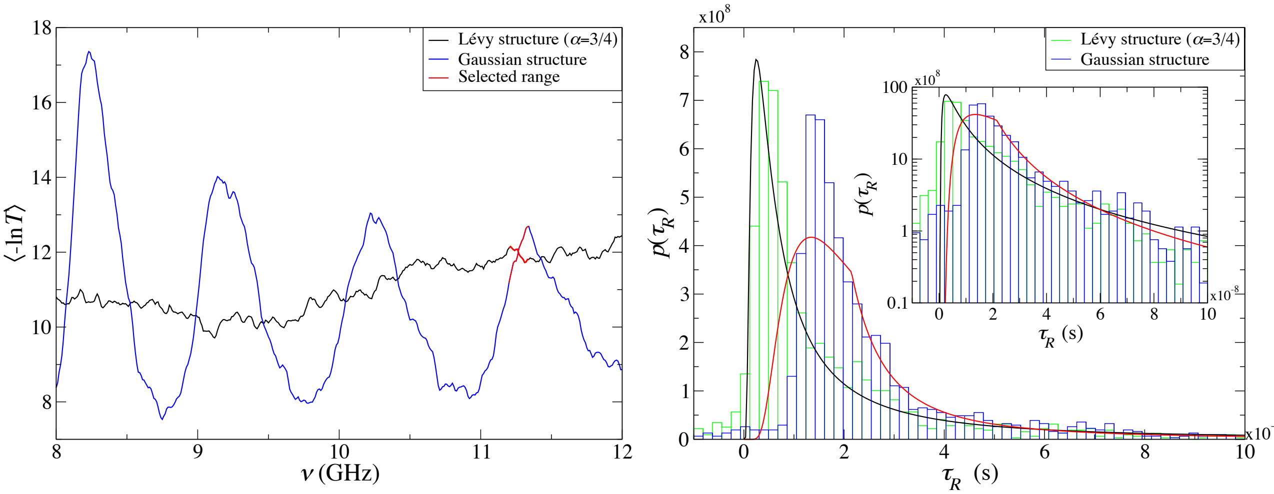

Figure 4.4: Left: The average $\langle -\ln T\rangle$ as a function of the frequency ν in the measured frequency range for the experimental system (black [Lévy disorder] and blue [Gaussian disorder] solid lines). The red solid line is the selected frequency range. Right: The probability density function $p(\tau_R)$ for the experimental system (histograms). The inset of each panel presents the same histogram of the main panel in semi-log scale. The solid black line is the theoretical prediction (3.6) with $p_s(\tau_R)$ the PDF (3.7) and $a = \alpha/3$ and the solid red line is the PDF (3.7). A good agreement between the theory the experimental data is observed.

Conclusions

A la mañana siguiente,
por un resto de piedad de la suerte,
amanecía muerto.
Horacio Quiroga (Estefanía)

In this thesis studies of wave transport in disordered media have been performed. Specifically, two different kinds of disordered structures were studied. First, the standard model of localization, also named *Anderson model*, whose disorder is characterized by PDFs with finite moments. The second one was the anomalous localization problem, or *Lévy problem*, where the disorder is characterized by PDFs with slow decay which may be characterized by the absence of finite mean and finite variance.

First, we have studied the mathematical formalism of the transfer and scattering matrices and a physical model based on electromagnetic dispersion. Together, the model and the formalism allowed developing numerical simulation which was the cornerstone of this work (see Chapter 1). Chapter 1 also presented two illustrative examples of the use of transfer matrices and a brief introduction of the Wigner time delay.

In Chapter 2, the Anderson model of localization for finite and infinite structures was presented. Finite systems leads to two transport regimes and a crossover region: ballistic regime ($s \ll 1$), localized regime ($s \gg 1$) and the coexistence region ($s \sim 1$). Then, the statistical properties of the transmission coefficient in finite waveguides were described. Here, we focused on the functions of the transmission around its average and the probability density functions of the transmission coefficient. Another important quantity that we studied in this chapter was the delay time. For the delay time, the theoretical PDF for large systems was found and tested with numerical simulations. Later, a correction of the theoretical distribution of delay times was developed and proven for short systems with finite transmission $T > 0$. This Chapter presented the behavior of reflection and transmission delay times.

Lévy disordered structures and the coexistence region of the ballistic and localized regimes were presented and studied in Chapter 3. First, stable distributions and some of their properties were shown. Then, the probability density function of the transmission coefficient in Lévy systems was found by considering fluctuations in the number of layers for structures of length L. Then, probability distributions of Lévy structures were contrasted with those for the standard Anderson transmission problem. It was observed that the statistics of the transmission in Lévy disordered systems show large differences with respect to the Anderson problem: fluctuations are larger in Lévy-type disordered systems. For the average of the logarithm of the transmission coefficient as a function of the length of the system L, we have found a power-law dependence $\langle -\ln T \rangle \propto L^{\alpha}$ which should be contrasted with the linear dependence in the Anderson case $\langle -\ln T \rangle \propto L$. Then, by considering the fluctuations of the number of scatterers in finite samples we were able to find Lévy probability density functions from the Anderson PDFs. This powerful algorithm provided a method to work later with the delay time.

For delay times, two different kinds of structures (homogeneous and inhomogeneous) were described. Then, the statistical properties of both structures have been found. Notice that the homogeneous problem is completely described by $\langle -\ln T \rangle$ and α, where α has been found numerically. Also, delay times in Lévy systems were contrasted with the delay times for Anderson structures. Here, we have to stress that the delay times in Lévy structures present a peak which is given by the finite size of the system and does not appear in the Anderson case.

Finally, in Chapter 4 experimental results previously obtained by Fernandez *.et al.* [10] were compared with our theoretical model and the numerical simulations. Here, a good agreement between the three results was observed for two different values of α: $\alpha = 1/2$, $\alpha = 3/4$ and a Gaussian random variable. From the experiment performed by Fernandez *.et al.*, an experimental comparison between Lévy delay times and delay times in Anderson systems was also possible.

Additionally, Appendix A shows some characteristics of system with absorption. Here, the delay time for those structures was characterized by small absorption. Appendix B discussed the statistics of the delay times for systems in the ballistic regime.

Future work

- The problem of transmission delay times in systems without a unitary scattering matrix (absorption and amplification cases) remains unsolved.

- A better statistical description of the statistics in inhomogeneous Lévy-disordered structures is needed.

- Some experiments using homogeneous Lévy structures could be performed to complete the description presented in Chapter 4.

Appendix A

Anderson structures with absorption

Looking down from ethereal skies,
silent crystalline tears I cry,
for all must say their last
goodbye to paradise.
Symphony X (Paradise lost)

Abstract

In this Appendix, a brief discussion of systems with absorption using standard disorder is presented. First, some approaches to mean transmission functions are shown. Later, delay times are studied.

Mean transmission

Since the effects of absorption are inevitable in natural systems, the study of structures with absorption becomes very important. Structures with absorption can be built experimentally and also found in nature. For wave transport, the dimensionless length will grow even if the reflection coefficient decreases. For small absorption, the statistics of delay times become similar to the statistics near the ballistic regime $s \sim 1$ given the "losses" in the reflection coefficient.

Changes in the dimensionless length

It is known that in presence of absorption or amplification, the dimensionless length s grows faster for the same amount of disorder [39, 40][1]. Thus, equation (2.4) is modified to take in count the effects of absorption or amplification and becomes

$$\langle -\ln T \rangle = \left(\frac{1}{l} + |\sigma| \right) L, \tag{A.1}$$

where σ represents the inverse absorption length. For a small absorption, the inverse of the absorption length can be written as

$$\sigma = -2k \operatorname{Im}(\sqrt{1 + \mathrm{i}\delta}), \tag{A.2}$$

where k is the wave number and δ is the imaginary part of the dielectric constant. If $\delta > 0$ absorption effects will be observed while amplifications appears for $\delta < 0$. Note that the sign of the absorption length depends on the sign of δ. It is also important to note that systems with absorption or amplification do not conserve the current, therefore $T + R \neq 1$, as well as equations (A.1) and (A.2) are applicable only for $\delta \ll 1$. A comparison between equation (A.1) and numerical simulations is shown in figure A.1. Here, equation (A.1) is evaluated numerically. Figure A.1 shows 12 different configurations for different frequencies, incident angles and absorption coefficients.

As in the case without absorption, here $\langle -\ln T \rangle$ only depends on the parameters of the system which can be measured experimentally. Then, the importance of equation (A.1) together with equation (A.2) is that they allow measuring the amount of disorder for structures with absorption.

Delay time

We have to recall that equation (2.18) was obtained by considering systems with $R < 1$. Thus, we assume that equation (2.18) can represent the statistics of the reflection delay time in the presence of absorption. In order to use this equation, the mean free path can be obtained from the numerical simulations using relation (A.1). Notice that here it is not expected that $\langle \tau_R \rangle = L/v_g$. The comparison of numerical simulation and the theoretical model is shown in figure A.2. Note that equation (2.18) works very well for small absorption.

[1]The amplification case will not be presented in this work

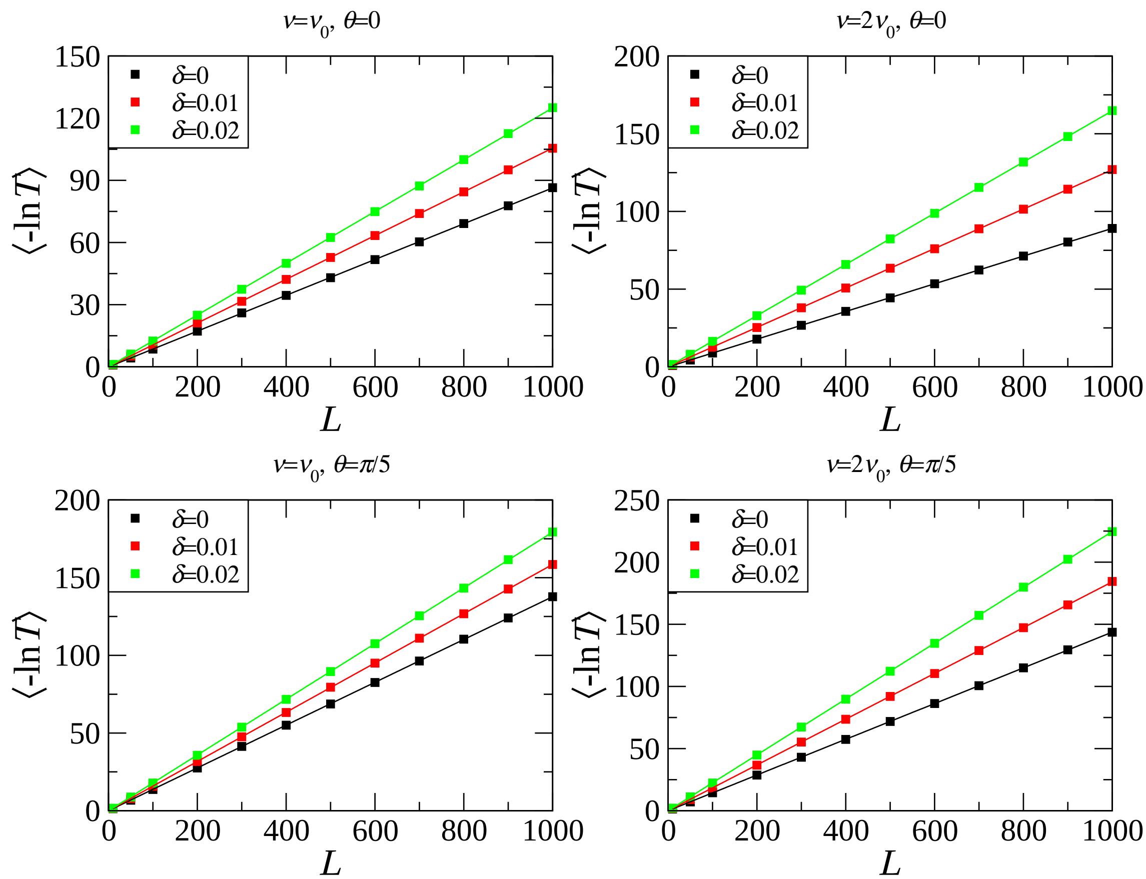

Figure A.1: The average $\langle -\ln T\rangle = s$ as a function of the system size L for one-dimensional layered structures conformed by two different media with absorption (symbols). The thickness of each layer is given by the absolute value of a Gaussian random variable characterized by $\mu = 0$ and $\sigma = 1$. The parameters are $n_a = 1.4$, $n_b = 2.4$ and $\nu_0 = 7.5$ GHz. Each panel presents three different values of the absorption for a given frequency and a given incident angle. The solid lines are fittings of the data with Eq. (A.1). Each symbol was calculated using 10^4 ensemble realizations.

Numerically, the four cases presented in figure A.2 keep the same amount of disorder and the same length while absorption grows. Since equation (2.7) just depends on the amount of disorder, the black solid line remains the same for all cases in figure A.2.

Transmission delay times

Finally, we have to say that relation (2.10) does not hold for systems with absorption or amplification. Remember that this relationship takes into account the unitarity of the scattering matrix which is not preserved if the current conservation is not conserved, even though τ_r and $\tau_{r'}$ are statistically identical and independent. This fact becomes evident in figure A.3 where the average of the reflection delay time and the average of the transmission delay time are shown for two different configurations and three absorption values.

Note that the average $\langle \tau_R\rangle$ grows until saturation limit regardless of the size of the system, while the average $\langle \tau_T\rangle$ keeps its usual behavior shown in systems without absorption, see figure 2.10. From

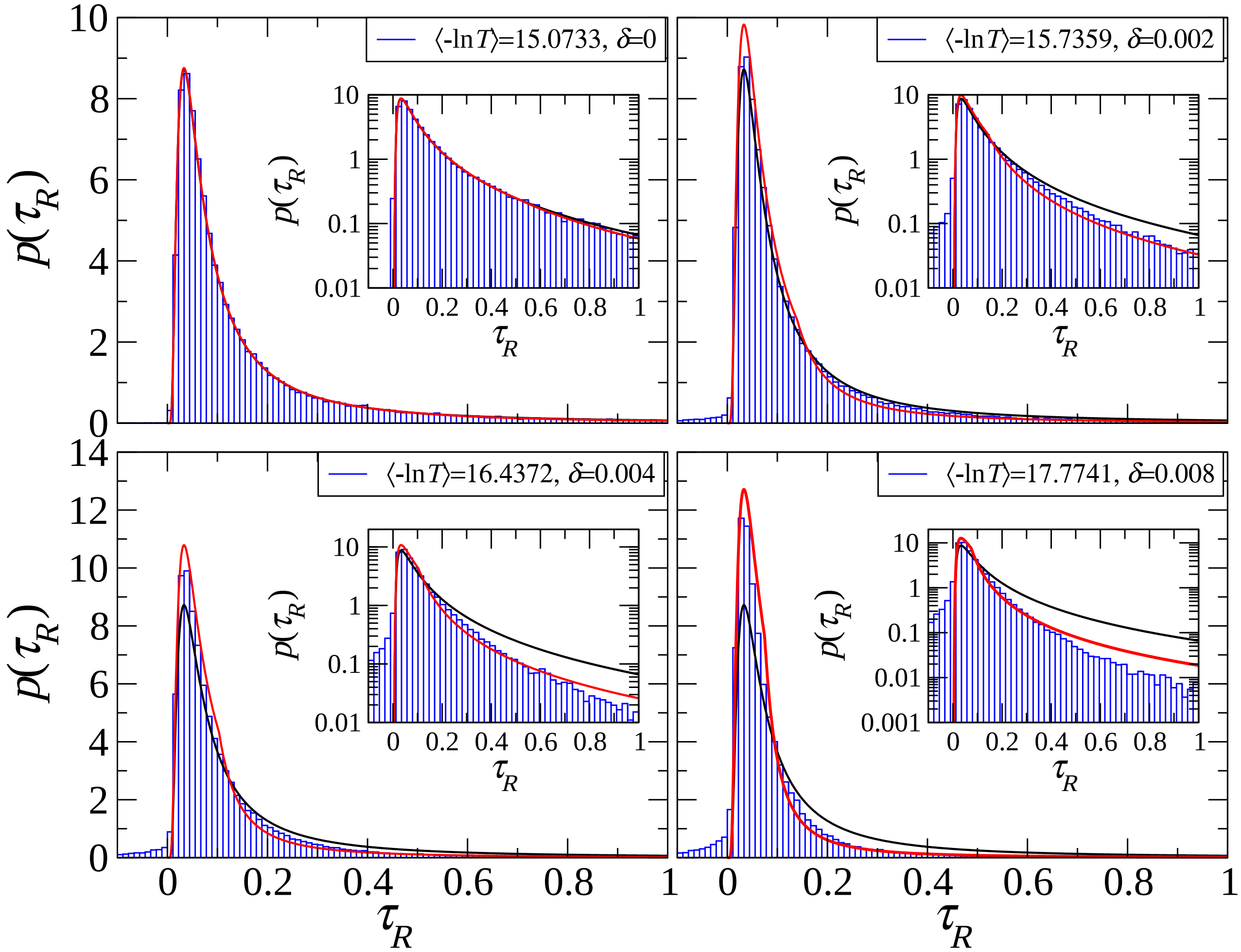

Figure A.2: The probability density function $p(\tau_R)$ for one-dimensional layered structures conformed by two different media with absorption (histograms). The thickness of each layer is given by the absolute value of a Gaussian random variable characterized by $\mu = 0$ and $\sigma = 1$. The parameters are $n_a = 1.4$, $n_b = 2.4$, $\nu = 7.5$ GHz and $\theta = 0$. Both, $\langle T\rangle$ and $\langle -\ln T\rangle$, are shown in each panel in order to identify the transport regime. The inset of each panel presents the same histogram of the main panel in semi-log scale. The solid black [red] line is the theoretical prediction (2.7) [(2.18)] with $\tau_0 = \langle\tau_R\rangle$. Each histogram was calculated using 10^5 ensemble realizations. A good agreement between theory and numerical simulation is observed. Here, we considered the change of variable $v_g\tau_R/2L \Rightarrow \tau_R$.

the average $\langle\tau_R\rangle$, it can be concluded that waves only penetrate until a certain point of the structure without be absorbed. On the other hand, the waves that have not been absorbed and reached the edge of the structure do it in the same way as in systems without absorption.

From the reflection delay time with absorption (upper panels), the average $\langle\tau_R\rangle$ as a function of the size of the system L has been numerically identified as

$$\langle\tau_R\rangle = a_0 + a_1 \ln L, \tag{A.3}$$

where a_0 and a_1 are fitting constants. Also, the corresponding results for r' can be found in Appendix C.

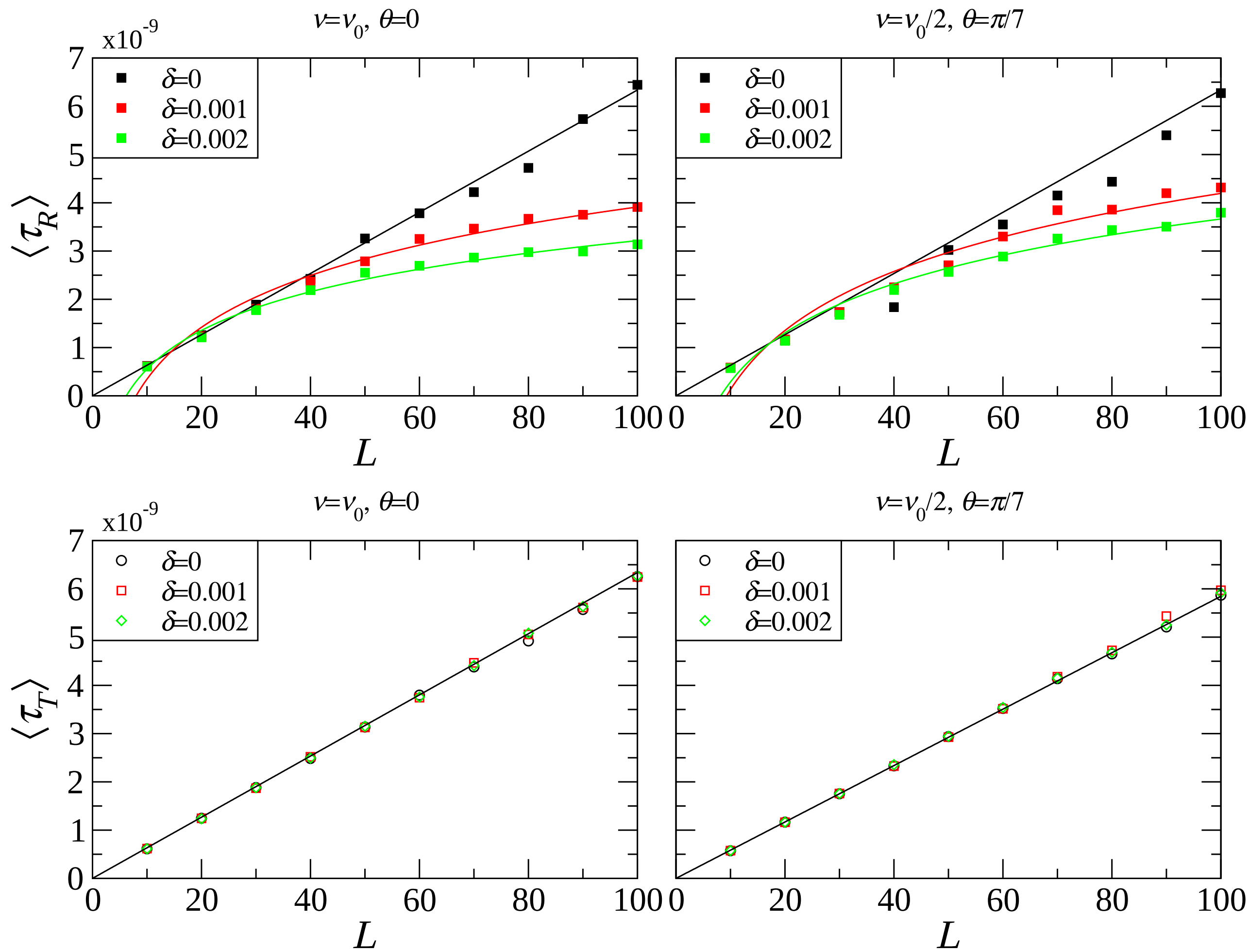

Figure A.3: The averages $\langle \tau_R \rangle$ [upper] and $\langle \tau_T \rangle$ [lower] as a function of the system size L for one-dimensional layered structures conformed by two different media with absorption (symbols). The thickness of each layer is given by the absolute value of a Gaussian random variable characterized by $\mu = 0$ and $\sigma = 1$. The parameters are $n_a = 1.4$, $n_b = 2.4$ and $\nu_0 = 7.5$ GHz. Each panel presents three different values of the absorption for a given frequency and a given incident angle. The solid lines are given by Eq. (2.9) [upper (black)], Eq. (A.3) [upper (red and green)] and Eq. (2.14) [lower]. Each symbol was calculated using 2×10^4 ensemble realizations. This graph does not contain any normalization over τ_R nor over τ_T.

Appendix B

Delay time in the ballistic regime

Licking doorknobs is
illegal on other planets
SpongeBob to Mr. Krabs
(SpongeBob SquarePants)

Abstract

This Appendix presents an approximation for ballistic systems based on the distribution of the corresponding reflection amplitudes. Also, the transmission delay times are briefly discussed numerically.

Gaussian approximation

As we noted in Chapter 2, finding the probability density function of delay times near the ballistic regime can be a difficult task. Also, ballistic reflections have an important property which allows us to understand the behavior of the corresponding delay times. As a first step, it is necessary to know what is the random process that these variables follow. Then, the probability density function of the reflection delay times can be found.

Complex Gaussian random process

Processes determined by a set of complex random variables r are called *complex Gaussian random processess* if the joint distribution of the real and imaginary parts are Gaussian [41]. In addition to this, real and imaginary parts are statistically Gaussian random processes and are independent between them. This kind of process is also called *circular* if $\langle \mathrm{Re}\{r\}\rangle = \langle \mathrm{Im}\{r\}\rangle = 0$. A graph of the reflection amplitude measured in our model is shown in figure B.1, as well as the statistics corresponding to r', which is presented in Appendix C.

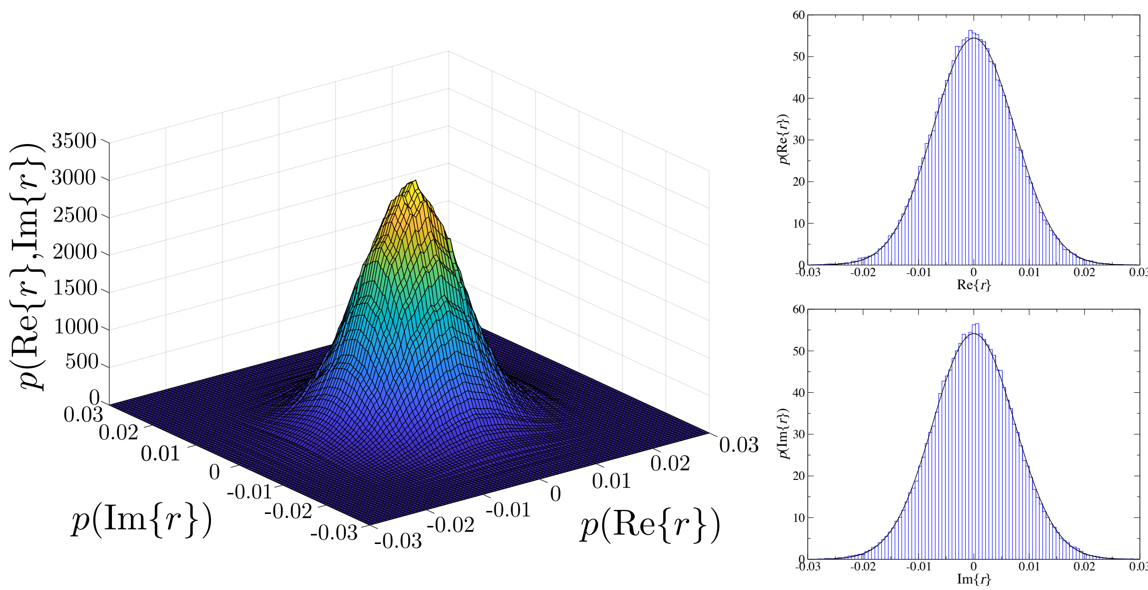

Figure B.1: The probability density functions $p(\mathrm{Re}\{r\}, \mathrm{Im}\{r\})$ [left], $p(\mathrm{Re}\{r\})$ [upper right] and $\mathrm{Im}\{r\}$ [lower right] for one-dimensional layered structures conformed by two different media, one inside another (histograms). The thickness of each layer is given by the absolute value of a Gaussian random variable characterized by $\mu = 0$ and $\sigma = 1$ [distance between two consecutive slabs] or $\mu = 0$ and $\sigma = 0.01$ [slab]. The parameters are $n_a = 1.4$, $n_b = 2.4$, $\nu = 7.5$ GHz, $\theta = 0$ and $\langle -\ln T\rangle = 0.0001$. The solid black lines [right] are fittings of Gaussian curves with $\mu = 0$. Each histogram was calculated using 10^5 ensemble realizations.

It is easy to observe that numerical simulations satisfy the conditions of a Complex Gaussian random process. Also, another important remark is that the transmission amplitude does not have these important properties, thus the probability distribution of its delay time cannot be found in the same way.

Reflection delay time distribution

According to [42, 43, 44], the Gaussian assumption allows computing the phase shift distribution by the integration of the joint distribution. It is written as

$$p(\tau_R) = \frac{Q}{2\langle\tau_R\rangle}\left[Q + \left(\frac{\tau_R}{\langle\tau_R\rangle} + 1\right)^2\right]^{-3/2}, \tag{B.1}$$

where $\langle\tau_R\rangle$ represents the mean of the distribution and Q is a dimensionless parameter related to the standard deviation. The comparison between this probability density function and numerical simulations is shown in figure B.2. Here, Q is considered as a free parameter.

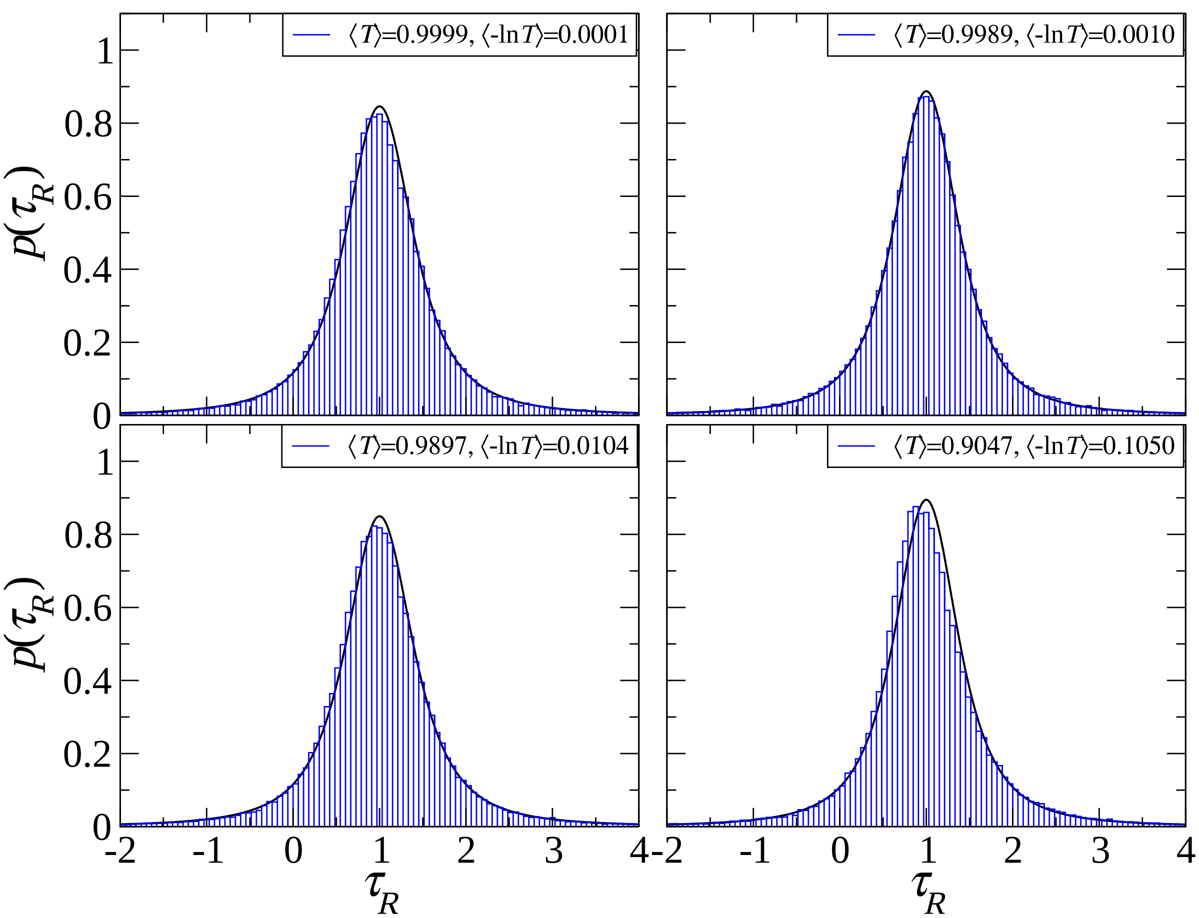

Figure B.2: The probability density function $p(\tau_R)$ for one-dimensional layered structures conformed by two different media, one inside another (histograms). The thickness of each layer is given by the absolute value of a Gaussian random variable characterized by $\mu = 0$ and $\sigma = 1$ [distance between two consecutive slabs] or $\mu = 0$ and $\sigma = 0.01$ [slab]. The parameters are $n_a = 1.4$, $n_b = 2.4$, $\nu = 7.5$ GHz and $\theta = 0$. Both, $\langle T\rangle$ and $\langle -\ln T\rangle$, are shown in each panel in order to identify the transport regime. The solid black lines are Gaussian characterized by $\mu = 0$. Each histogram was calculated using 10^5 ensemble realizations. A good agreement between theory and numerical simulation is observed. Here, we considered the change of variable $\tau_R/\langle\tau_R\rangle \Rightarrow \tau_R$.

As we can observe from figure B.2, the discrepancies between theory and numerical simulations increase when the dimensionless length s grows. That is because the Gaussian assumption does not work well close to the localized regime. Another problem appears when the size of the structures has the same order of magnitude as the size of the scatterers. To solved this, the dense-weak-scattering limit again should be approached.

Finally, it is important to mention that the convolution method used in Chapters 2 and 3 to find the delay time distribution in the transmission case cannot be applied here because the reflections amplitudes r and r' are strongly correlated in this regime.

Gaussian delay time

Despite this problem have not been solved analytically, a numerical characterization was developed. Our main numerical results are shown in figure B.3 without free parameters. Similarly to the reflection case, here the discrepancies increase near the localized regime.

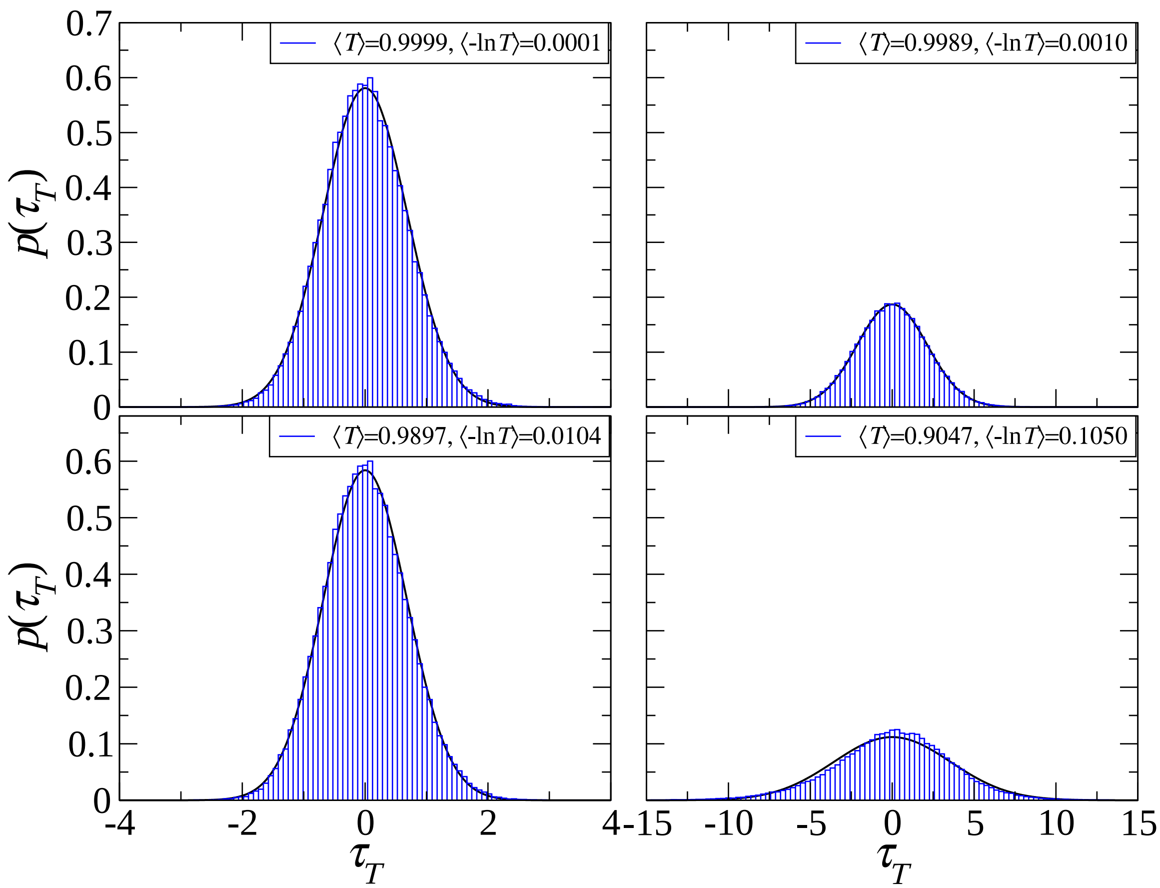

Figure B.3: The probability density function $p(\tau_T)$ for one-dimensional layered structures conformed by two different media, one inside another (histograms). The thickness of each layer is given by the absolute value of a Gaussian random variable characterized by $\mu = 0$ and $\sigma = 1$ [distance between two consecutive slabs] or $\mu = 0$ and $\sigma = 0.01$ [slab]. The parameters are $n_a = 1.4$, $n_b = 2.4$, $\nu = 7.5$ GHz and $\theta = 0$. Both, $\langle T \rangle$ and $\langle -\ln T \rangle$, are shown in each panel in order to identify the transport regime. The solid black lines are Gaussian curves. Each histogram was calculated using 10^5 ensemble realizations. A good agreement between the Gaussian curves and numerical simulation is observed. Here, we considered the change of variable $\tau_T - \langle \tau_T \rangle \Rightarrow \tau_T$.

Appendix C

Complementary results

Nos amaremos después, la vida nos matará,
seremos polvo otra vez, la tierra nos beberá,
muy lejos de este lugar tal vez te vuelva a encontrar,
nada será como es, tal vez seamos polvo estelar.
Monocordio (Siempre te busqué)

Abstract

In this Appendix, a set of complementary graphs is presented. First, results corresponding to the delay time of r' for the Anderson localization are shown. Then, the probability density functions of the transmission and the delay times, as well as curves of $\langle T\rangle$, $\langle -\ln T\rangle$ and $\langle\tau\rangle$ as functions of the parameters in Lévy-disordered system are presented.

Delay time for r' (Anderson localization)

This section is divided into three parts. The first one presents results for the localized regime which was discussed in Chapter 2. The second one shows the results of the absorption case from Appendix A. In the last part, some plots related to the ballistic regime presented in Appendix B can be found.

Localized regime

In figure C.1, a comparison between equation (2.13) and numerical simulations is shown. Figure C.2 shows the average $\langle \tau_{R'} \rangle$ as functions of the size of the system L. A comparison between numerical simulations and equations (2.7) and (2.18) can be observed in figure C.3.

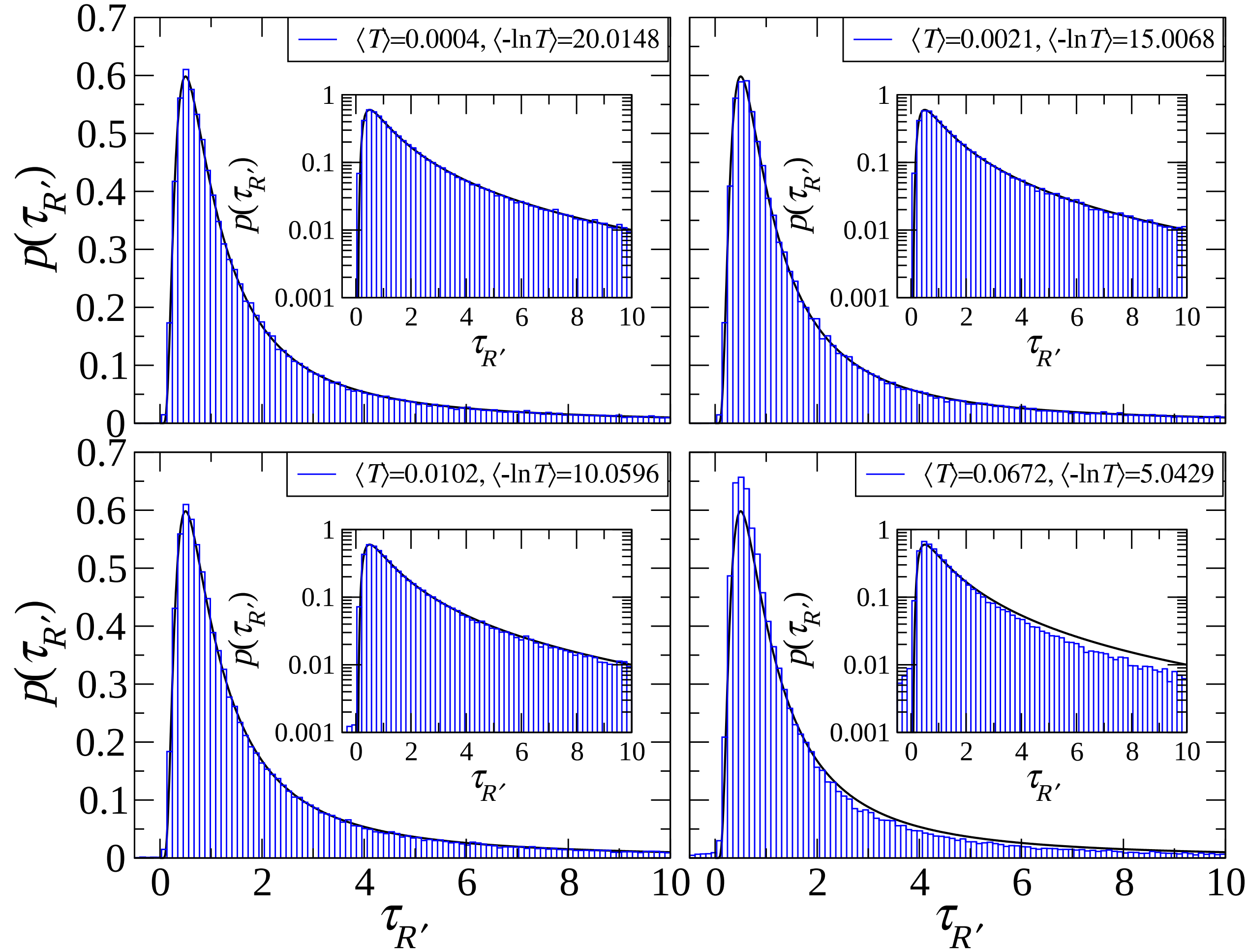

Figure C.1: The probability density function $p(\tau_{R'})$ for one-dimensional layered structures conformed by two different media (histograms). The thickness of each layer is given by the absolute value of a Gaussian random variable characterized by $\mu = 0$ and $\sigma = 1$. The parameters are $n_a = 1.4$, $n_b = 2.4$, $\nu = 7.5$ GHz and $\theta = 0$. Both, $\langle T \rangle$ and $\langle -\ln T \rangle$, are shown in each panel in order to identify the transport regime. The inset of each panel presents the same histogram of the main panel in semi-log scale. The solid black line is the theoretical prediction (2.7). Each histogram was calculated using 10^5 ensemble realizations. A good agreement between theory and numerical simulations is observed but the discrepancies increase when s decreases. Here, we considered the change of variable $\tau_{R'}/\gamma \Rightarrow \tau_{R'}$.

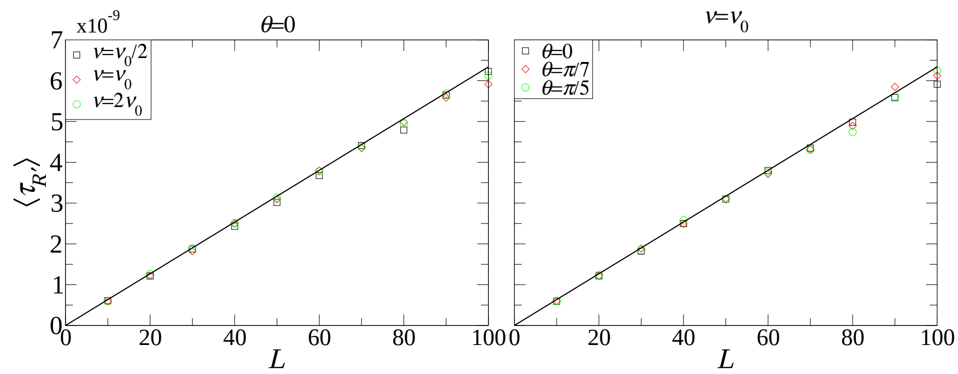

Figure C.2: The average $\langle \tau_{R'} \rangle$ as a function of the system size L for one-dimensional layered structures conformed by two different media (symbols). The thickness of each layer is given by the absolute value of a Gaussian random variable characterized by $\mu = 0$ and $\sigma = 1$. The parameters are $n_a = 1.4$, $n_b = 2.4$ and $\nu_0 = 7.5$ GHz. In the right [left] panel we keep the frequency [incident angle] constant while the incident angle [frequency] changes. The solid lines are given by Eq. (2.9). Each symbol was calculated using 2×10^4 ensemble realizations. This graph does not contain any normalization over $\tau_{R'}$.

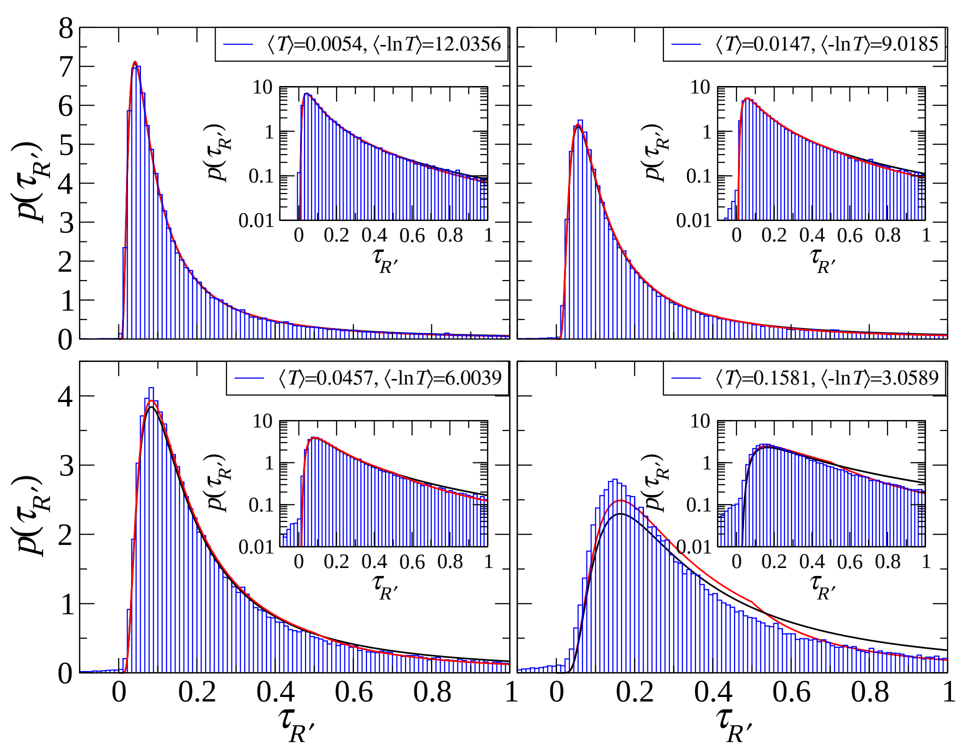

Figure C.3: The probability density function $p(\tau_{R'})$ for one-dimensional layered structures conformed by two different media (histograms). The thickness of each layer is given by the absolute value of a Gaussian random variable characterized by $\mu = 0$ and $\sigma = 1$. The parameters are $n_a = 1.4$, $n_b = 2.4$, $\nu = 7.5$ GHz and $\theta = 0$. Both, $\langle T \rangle$ and $\langle -\ln T \rangle$, are shown in each panel in order to identify the transport regime. The inset of each panel presents the same histogram of the main panel in semi-log scale. The solid black [red] line is the theoretical prediction (2.7) [(2.18)] with $\tau_0 = \langle \tau_R \rangle$. Each histogram was calculated using 10^5 ensemble realizations. A good agreement between theory and numerical simulation is observed. Here, we considered the change of variable $v_g \tau_{R'}/2L \Rightarrow \tau_{R'}$.

Absorption case

Here, two figures corresponding to absorption systems are presented. Figure C.4 shows a comparison between equations (2.7) and (2.18) numerical simulations. Then, in figure C.5 the average $\langle \tau_{R'} \rangle$ versus the system size L is plotted.

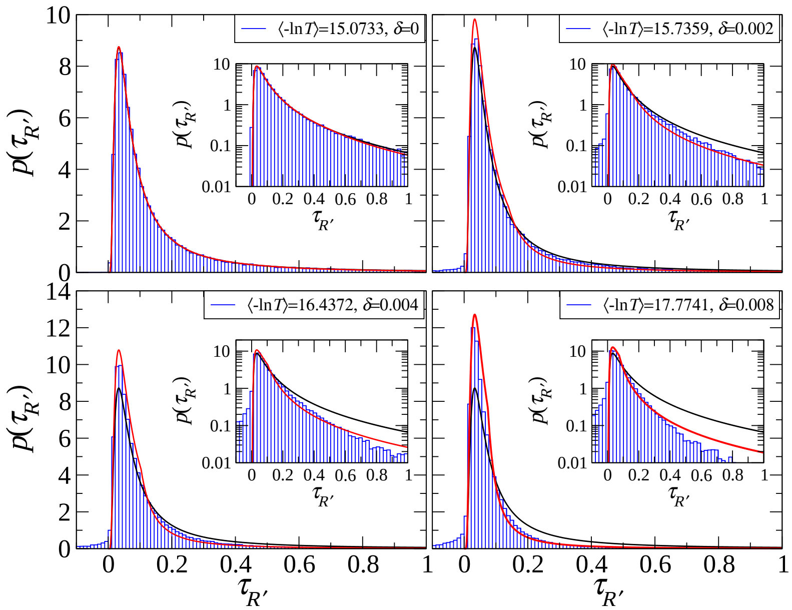

Figure C.4: The probability density function $p(\tau_{R'})$ for one-dimensional layered structures conformed by two different media with absorption (histograms). The thickness of each layer is given by the absolute value of a Gaussian random variable characterized by $\mu = 0$ and $\sigma = 1$. The parameters are $n_a = 1.4$, $n_b = 2.4$, $\nu = 7.5$ GHz and $\theta = 0$. Both, $\langle T \rangle$ and $\langle -\ln T \rangle$, are shown in each panel in order to identify the transport regime. The inset of each panel presents the same histogram of the main panel in semi-log scale. The solid black [red] line is the theoretical prediction (2.7) [(2.18)] with $\tau_0 = \langle \tau_R \rangle$. Each histogram was calculated using 10^5 ensemble realizations. A good agreement between theory and numerical simulation is observed. Here, we considered the change of variable $v_g \tau_{R'}/2L \Rightarrow \tau_{R'}$.

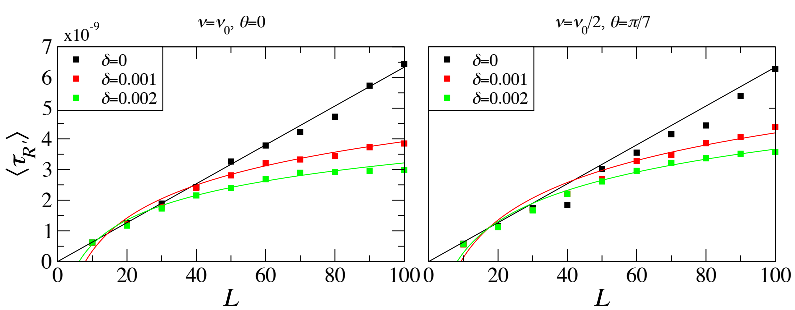

Figure C.5: The averages $\langle \tau_{R'} \rangle$ as a function of the system size L for one-dimensional layered structures conformed by two different media with absorption (symbols). The thickness of each layer is given by the absolute value of a Gaussian random variable characterized by $\mu = 0$ and $\sigma = 1$. The parameters are $n_a = 1.4$, $n_b = 2.4$ and $\nu_0 = 7.5$ GHz. Each panel presents three different values of the absorption for a given frequency and a given incident angle. The solid lines are given by Eq. (2.9) (black) and Eq. (A.3) (red and green). Each symbol was calculated using 2×10^4 ensemble realizations. This graph does not contain any normalization over $\tau_{R'}$.

Ballistic regime

Here we present two figures related to the ballistic regime. First, a figure of the distribution of the reflection amplitude r', real and imaginary parts, is shown in figure C.6. Then, the statistics of the corresponding delay times appear in figure C.7.

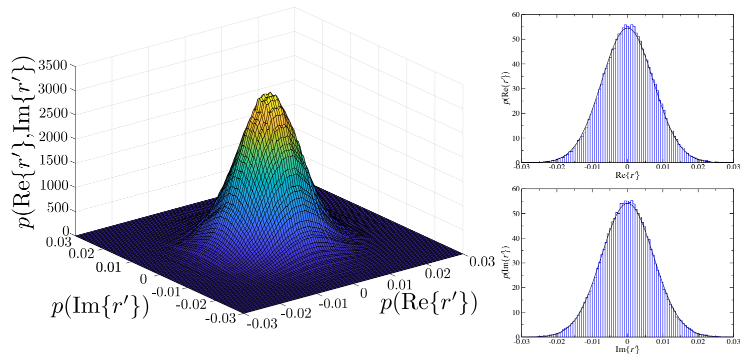

Figure C.6: The probability density functions $p(\mathrm{Re}\{r'\}, \mathrm{Im}\{r'\})$ [left], $p(\mathrm{Re}\{r'\})$ [upper right] and $\mathrm{Im}\{r'\}$ [lower right] for one-dimensional layered structures conformed by two different media, one inside another (histograms). The thickness of each layer is given by the absolute value of a Gaussian random variable characterized by $\mu = 0$ and $\sigma = 1$ [distance between two consecutive slabs] or $\mu = 0$ and $\sigma = 0.01$ [slab]. The parameters are $n_a = 1.4$, $n_b = 2.4$, $\nu = 7.5$ GHz, $\theta = 0$ and $\langle -\ln T\rangle = 0.0001$. The solid black lines [right] are fittings of Gaussian curves with $\mu = 0$. Each histogram was calculated using 10^5 ensemble realizations.

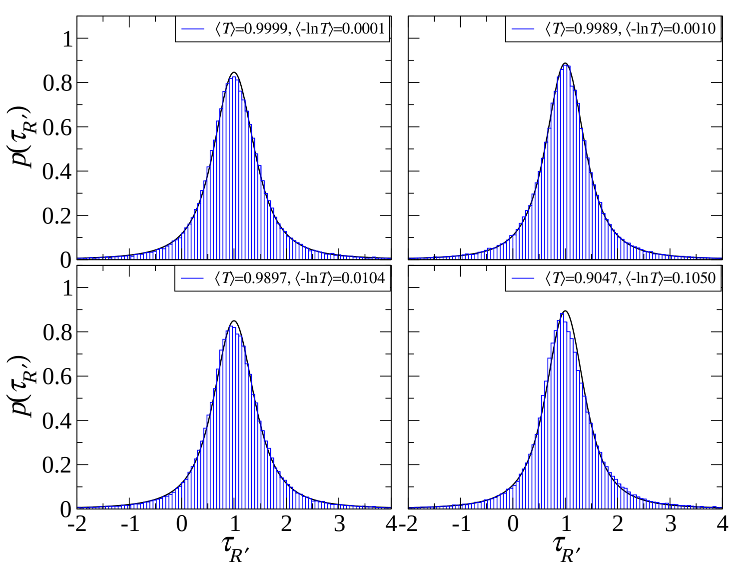

Figure C.7: The probability density function $p(\tau_{R'})$ for one-dimensional layered structures conformed by two different media, one inside another (histograms). The thickness of each layer is given by the absolute value of a Gaussian random variable characterized by $\mu = 0$ and $\sigma = 1$ [distance between two consecutive slabs] or $\mu = 0$ and $\sigma = 0.01$ [slab]. The parameters are $n_a = 1.4$, $n_b = 2.4$, $\nu = 7.5$ GHz and $\theta = 0$. Both, $\langle T\rangle$ and $\langle -\ln T\rangle$, are shown in each panel in order to identify the transport regime. The solid black lines are Gaussian characterized by $\mu = 0$. Each histogram was calculated using 10^5 ensemble realizations. A good agreement between theory and numerical simulation is observed. Here, we considered the change of variable $\tau_{R'}/\langle\tau_{R'}\rangle \Rightarrow \tau_{R'}$.

Transport through a Lévy structure

This section presents a set of graphs corresponding to Chapter 3. The first subsection presents results of the transmission distribution through Lévy disordered structures. The second subsection shows plots of delay times for $\alpha = 3/4$ and the r'.

Transmission coefficient quantities

First, a figure showing the average $\langle -\ln T \rangle$ as a function of the system size L appears in figure C.8. The change of the average $\langle T \rangle$ respect the size of the system L is observed in figure C.9. Finally, figures C.10, C.11 and C.12 show different comparisons between Lévy localization, Anderson model and their corresponding theoretical predictions.

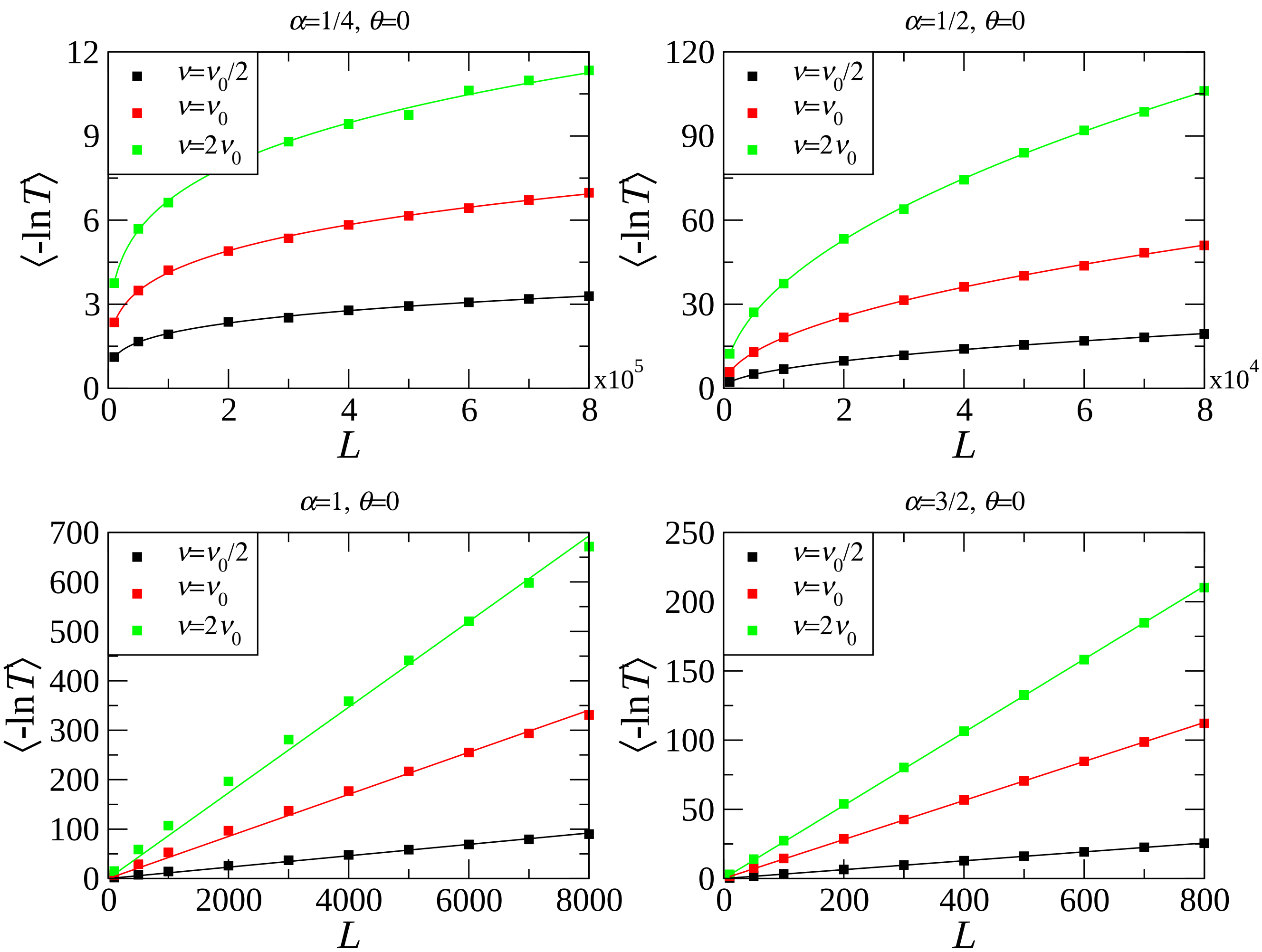

Figure C.8: The average $\langle -\ln T \rangle$ as a function of the system size L for one-dimensional layered structures conformed by two different media, one inside another (symbols). The thickness of the layers is $l_b = 0.25$ cm while the distance between them is given by the absolute value of a Lévy random variable characterized by α and $\beta = 0$. The parameters are $n_a = 1$, $n_b = \sqrt{4.4}$ and $\nu_0 = 8.5$ GHz. In each panel we keep the incident angle constant while the frequency changes. The solid lines are fittings of the data with Eq. (3.3). Each symbol was calculated using 10^4 ensemble realizations.

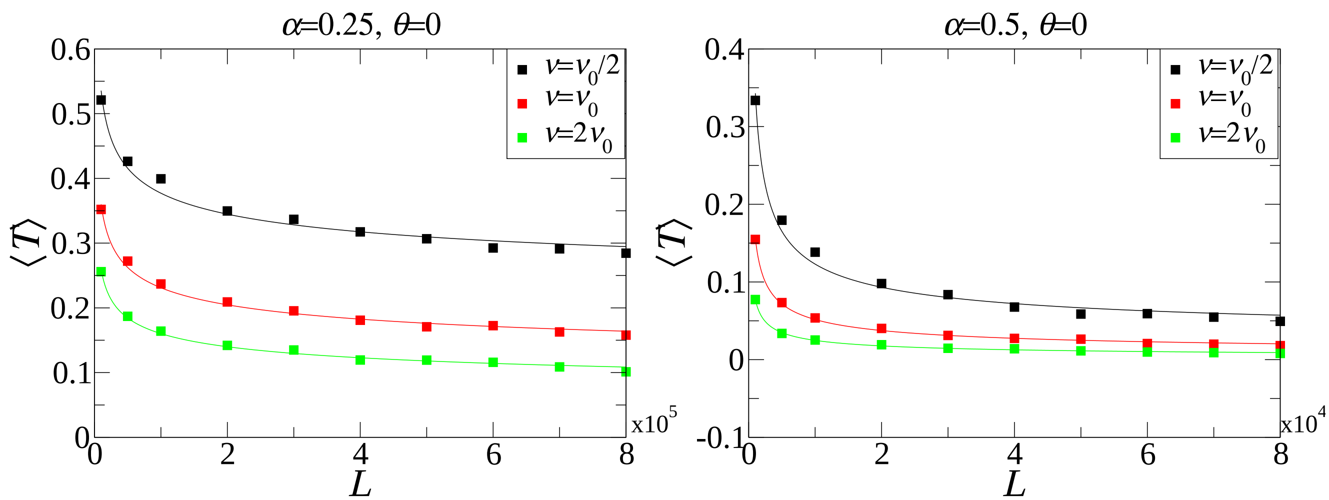

Figure C.9: The average $\langle T\rangle$ as a function of the system size L for one-dimensional layered structures conformed by two different media, one inside another (symbols). The thickness of the layers is $l_b = 0.25$ cm while the distance between them is given by the absolute value of a Lévy random variable characterized by α and $\beta = 0$. The parameters are $n_a = 1$, $n_b = \sqrt{4.4}$ and $\nu_0 = 8.5$ GHz. In each panel we keep the incident angle constant while the frequency changes. The solid lines are fittings of the data with Eq. (3.5). Each symbol was calculated using 10^4 ensemble realizations.

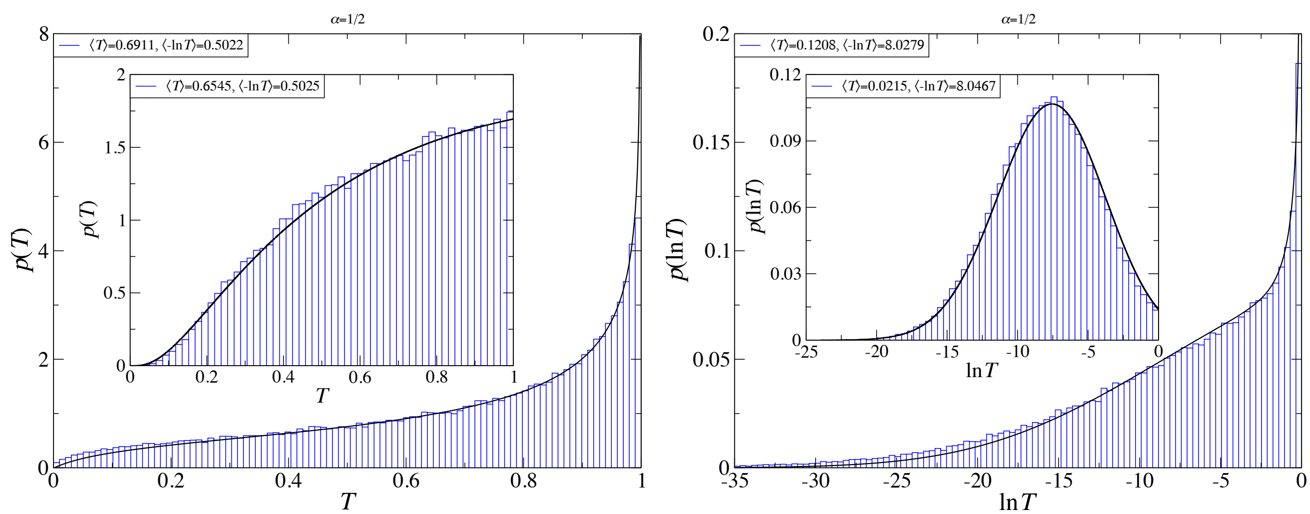

Figure C.10: The probability density functions $p(T)$ [left] and $p(\ln T)$ [right] for one-dimensional layered structures conformed by two different media, one inside another (histograms). The thickness of the layers is $l_b = 0.05$ cm [left] and $l_b = 0.5$ cm [right] while the distance between them is given by the absolute value of a Lévy random variable characterized by $\alpha = 1/2$ and $\beta = 0$. The parameters are $n_a = 1.4$, $n_b = \sqrt{4.4}$, $\nu = 7.5$ GHz and $\theta = 0$. Both, $\langle T\rangle$ and $\langle -\ln T\rangle$, are shown in each panel in order to identify the transport regime. The solid black line is the theoretical prediction (3.4) with $p_s(T)$ the PDF (2.3). Inset: The probability density functions $p(T)$ [left] and $p(\ln T)$ [right] for one-dimensional layered structures conformed by two different media (histograms). The thickness of each layer is given by the absolute value of a Gaussian random variable characterized by $\mu = 0$ and $\sigma = 1$. The parameters are $n_a = 1.4$, $n_b = 2.4$, $\nu = 7.5$ GHz and $\theta = 0$. The solid black line is the theoretical prediction (2.3). Each histogram was calculated using 10^5 ensemble realizations. A good agreement between theory and numerical simulations is observed.

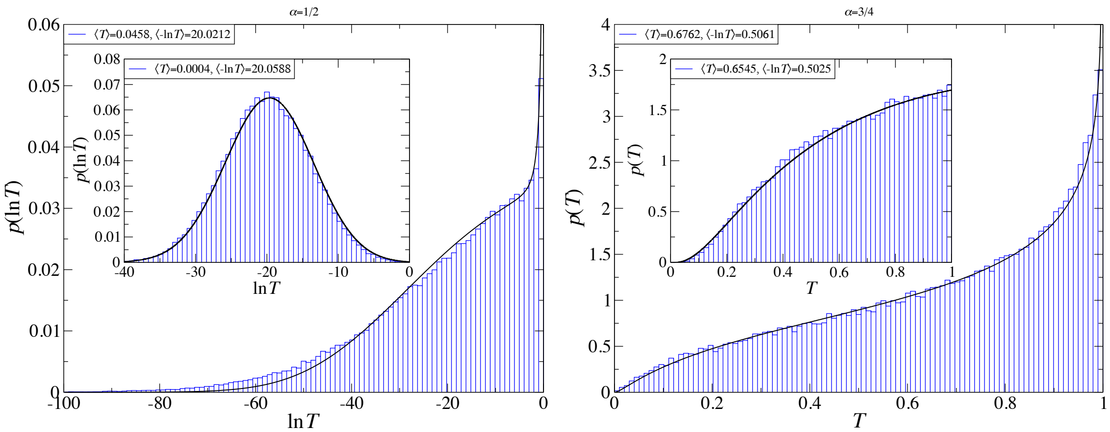

Figure C.11: The probability density functions $p(T)$ [left] and $p(\ln T)$ [right] for one-dimensional layered structures conformed by two different media, one inside another (histograms). The thickness of the layers is $l_b = 0.05$ cm [left] and $l_b = 0.5$ cm [right] while the distance between them is given by the absolute value of a Lévy random variable characterized by $\alpha = 1/2$ [left], $\alpha = 3/4$ [right] and $\beta = 0$. The parameters are $n_a = 1.4$, $n_b = \sqrt{4.4}$, $\nu = 7.5$ GHz and $\theta = 0$. Both, $\langle T \rangle$ and $\langle -\ln T \rangle$, are shown in each panel in order to identify the transport regime. The solid black line is the theoretical prediction (3.4) with $p_s(T)$ the PDF (2.3). Inset: The probability density functions $p(T)$ [left] and $p(\ln T)$ [right] for one-dimensional layered structures conformed by two different media (histograms). The thickness of each layer is given by the absolute value of a Gaussian random variable characterized by $\mu = 0$ and $\sigma = 1$. The parameters are $n_a = 1.4$, $n_b = 2.4$, $\nu = 7.5$ GHz and $\theta = 0$. The solid black line is the theoretical prediction (2.3). Each histogram was calculated using 10^5 ensemble realizations. A good agreement between theory and numerical simulations is observed.

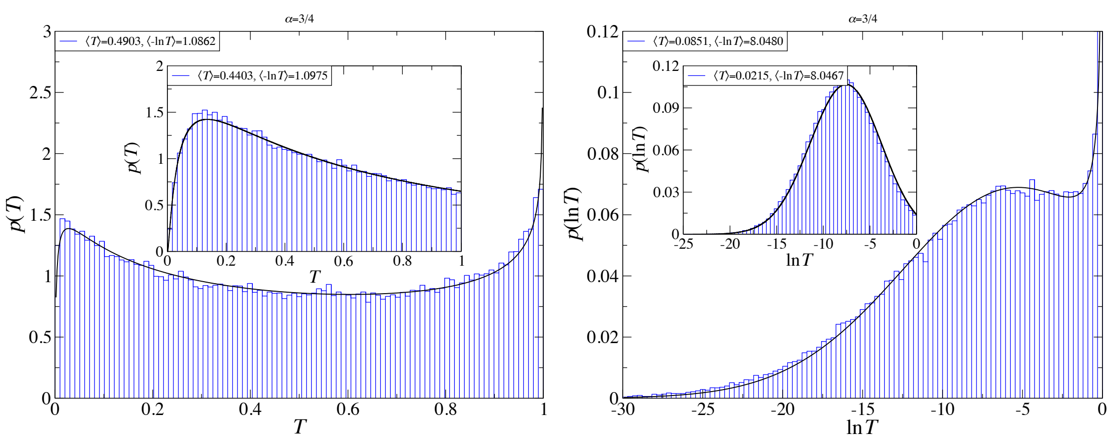

Figure C.12: The probability density functions $p(T)$ [left] and $p(\ln T)$ [right] for one-dimensional layered structures conformed by two different media, one inside another (histograms). The thickness of the layers is $l_b = 0.05$ cm [left] and $l_b = 0.5$ cm [right] while the distance between them is given by the absolute value of a Lévy random variable characterized by $\alpha = 3/4$ and $\beta = 0$. The parameters are $n_a = 1.4$, $n_b = \sqrt{4.4}$, $\nu = 7.5$ GHz and $\theta = 0$. Both, $\langle T \rangle$ and $\langle -\ln T \rangle$, are shown in each panel in order to identify the transport regime. The solid black line is the theoretical prediction (3.4) with $p_s(T)$ the PDF (2.3). Inset: The probability density functions $p(T)$ [left] and $p(\ln T)$ [right] for one-dimensional layered structures conformed by two different media (histograms). The thickness of each layer is given by the absolute value of a Gaussian random variable characterized by $\mu = 0$ and $\sigma = 1$. The parameters are $n_a = 1.4$, $n_b = 2.4$, $\nu = 7.5$ GHz and $\theta = 0$. The solid black line is the theoretical prediction (2.3). Each histogram was calculated using 10^5 ensemble realizations. A good agreement between theory and numerical simulations is observed.

Delay times

Figure C.13 shows a comparison of the statistics of delay times for two Lévy structures and an Anderson system. Figure C.14 presents a comparison for an inhomogeneous system in contrast with an homogeneous structure for $\alpha = 3/4$. Statistics of reflection delay times $\tau_{R'}$ with $\alpha = 1/2$ is shown in figure C.15. The behavior of the average of $\tau_{R'}$ with the length of the system is presented in figure C.16. Then, figures C.17, C.18 and C.19 present the statistics of τ_R, $\tau_{R'}$ and τ_T for $\alpha = 3/4$.

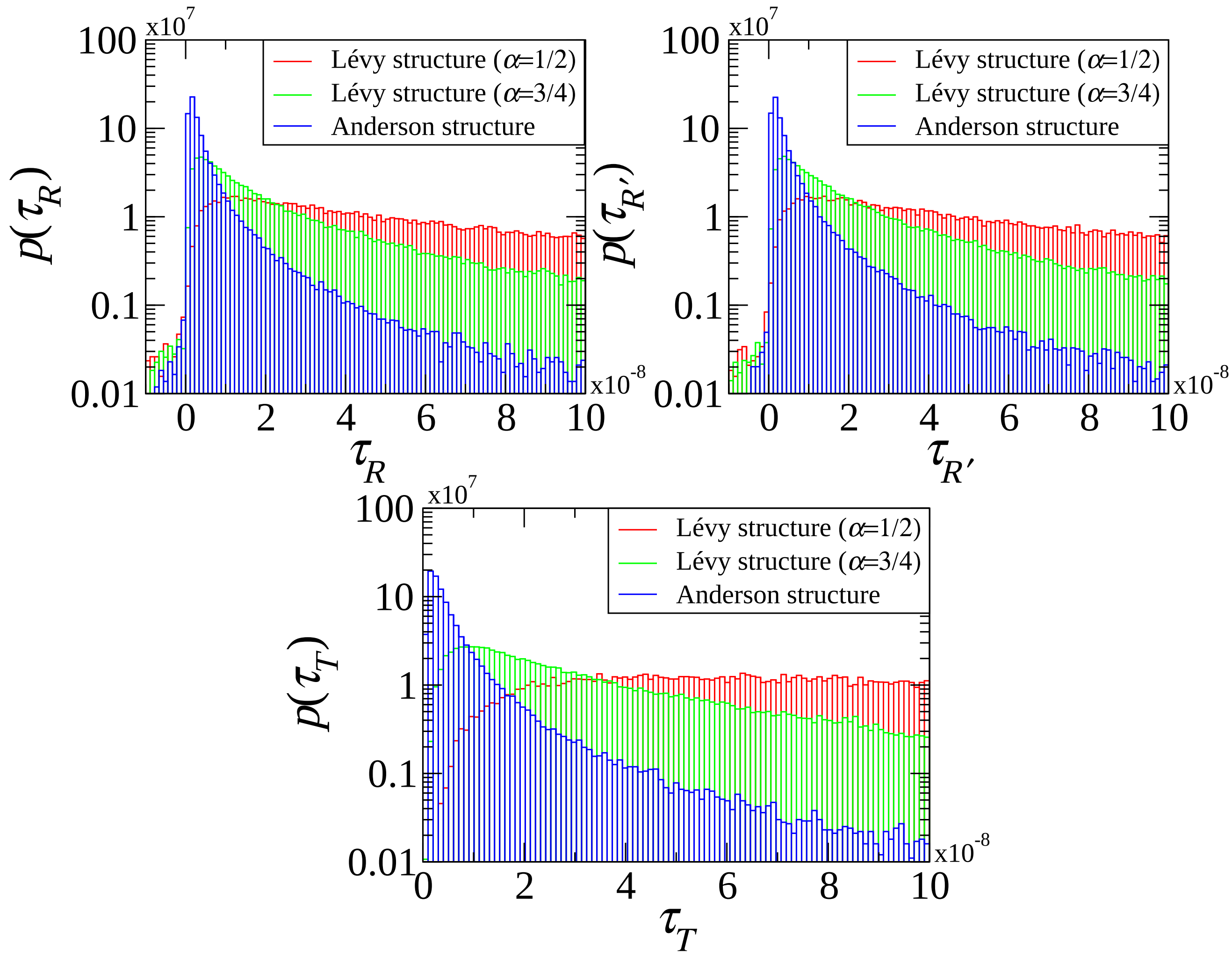

Figure C.13: The probability density function $p(\tau_R)$ [upper left], $p(\tau'_R)$ [upper right] and $p(\tau_T)$ [lower] for one-dimensional layered structures conformed by two different media, one inside another (histograms). The thickness of the layers is $l_b = 0.25$ cm while the distance between them is given by the absolute value of a Lévy random variable characterized by $\alpha = 1/2$ (red histogram), $\alpha = 3/4$ (green histogram) and $\beta = 0$ and by the absolute value of a Gaussian random variable characterized by $\mu = 0$ and $\sigma = 1$ (blue histogram). The parameters are $n_a = 1.4$, $n_b = \sqrt{4.4}$, $\nu = 7.5$ GHz, $\theta = 0$ and $\langle -\ln T \rangle \sim 10$. Each histogram was calculated using 10^5 ensemble realizations.

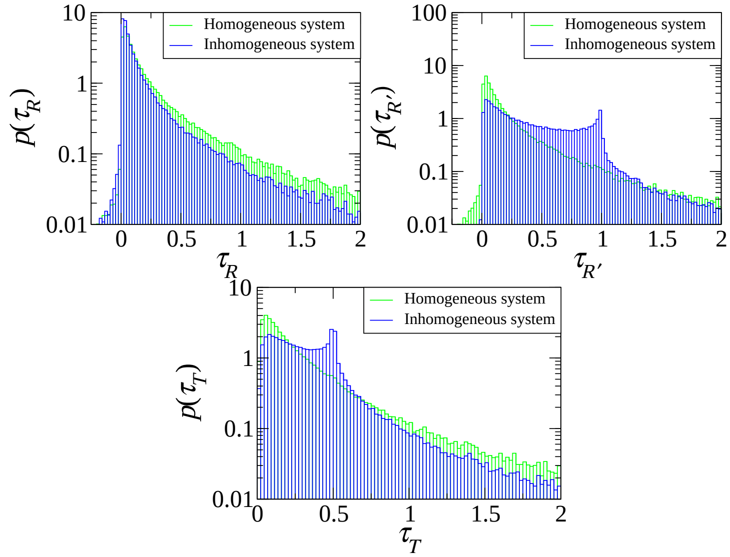

Figure C.14: The probability density function $p(\tau_R)$ [upper left], $p(\tau'_R)$ [upper right] and $p(\tau_T)$ [lower] for one-dimensional layered structures conformed by two different media, one inside another (histograms). The thickness of the layers is $l_b = 0.25$ cm while the distance between them is given by the absolute value of a Lévy random variable characterized by $\alpha = 3/4$ and $\beta = 0$ for both systems, homogeneous (green histograms) and inhomogeneous (blue histograms). The parameters are $n_a = 1.4$, $n_b = \sqrt{4.4}$, $\nu = 7.5$ GHz, $\theta = 0$ and $\langle -\ln T\rangle \sim 10$. Each histogram was calculated using 10^5 ensemble realizations.

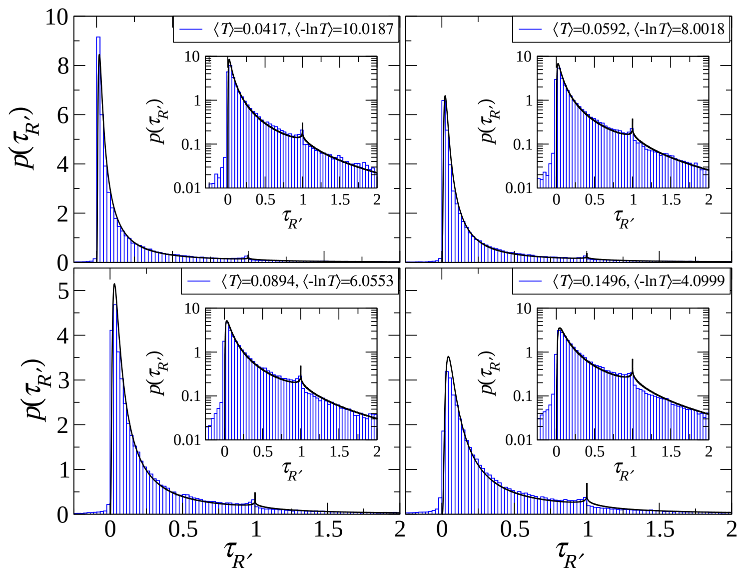

Figure C.15: The probability density function $p(\tau_{R'})$ for one-dimensional layered structures conformed by two different media, one inside another (histograms). The thickness of the layers is $l_b = 0.25$ cm while the distance between them is given by the absolute value of a Lévy random variable characterized by $\alpha = 1/2$ and $\beta = 0$. The parameters are $n_a = 1$, $n_b = \sqrt{4.4}$, $\nu = 7.5$ GHz and $\theta = 0$. Both, $\langle T\rangle$ and $\langle -\ln T\rangle$, are shown in each panel in order to identify the transport regime. The inset of each panel presents the same histogram of the main panel in semi-log scale. The solid black line is the theoretical prediction (3.6) with $p_s(\tau_R)$ the PDF (3.7) and $a = \alpha$. Each histogram was calculated using 10^5 ensemble realizations. A good agreement between theory and numerical simulation is observed. Here, we considered the change of variable $v_g\tau_{R'}/2L \Rightarrow \tau_{R'}$.

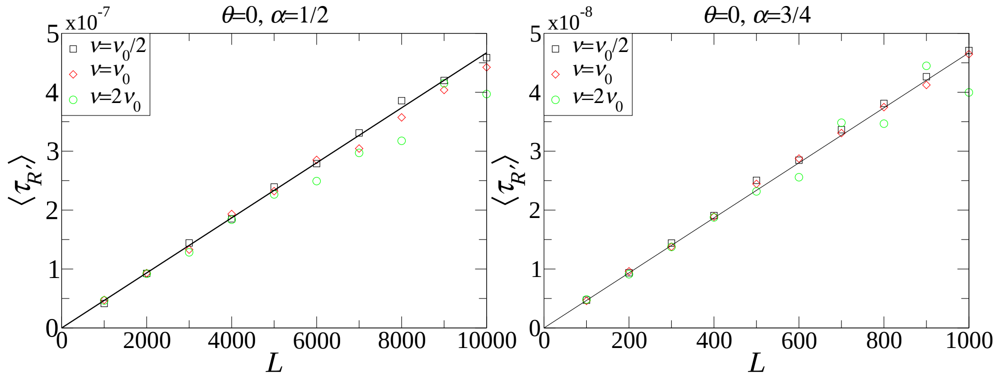

Figure C.16: The average $\langle \tau_{R'} \rangle$ as a function of the system size L for one-dimensional layered structures conformed by two different media, one inside another (symbols). The thickness of the layers is $l_b = 0.25$ cm while the distance between them is given by the absolute value of a Lévy random variable characterized by $\alpha = 1/2$ [left], $\alpha = 3/4$ [right] and $\beta = 0$. The parameters are $n_a = 1.4$, $n_b = \sqrt{4.4}$, $\nu_0 = 7.5$ GHz and $\theta = 0$. We keep the incident angle constant while the frequency changes. The solid lines are given by Eq. (3.8). Each symbol was calculated using 2×10^4 ensemble realizations. This graph does not contain any normalization over $\tau_{R'}$.

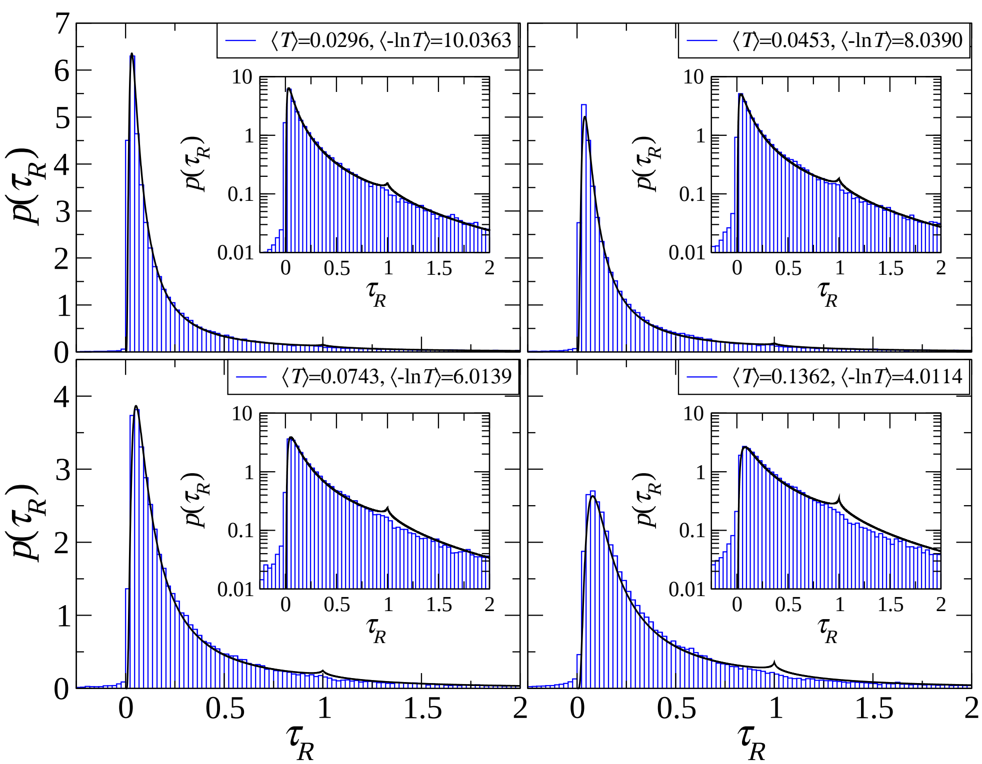

Figure C.17: The probability density function $p(\tau_R)$ for one-dimensional layered structures conformed by two different media, one inside another (histograms). The thickness of the layers is $l_b = 0.25$ cm while the distance between them is given by the absolute value of a Lévy random variable characterized by $\alpha = 3/4$ and $\beta = 0$. The parameters are $n_a = 1$, $n_b = \sqrt{4.4}$, $\nu = 7.5$ GHz and $\theta = 0$. Both, $\langle T \rangle$ and $\langle -\ln T \rangle$, are shown in each panel in order to identify the transport regime. The inset of each panel presents the same histogram of the main panel in semi-log scale. The solid black line is the theoretical prediction (3.6) with $p_s(\tau_R)$ the PDF (3.7) and $a = \alpha$. Each histogram was calculated using 10^5 ensemble realizations. A good agreement between theory and numerical simulation is observed. Here, we considered the change of variable $v_g \tau_R / 2L \Rightarrow \tau_R$.

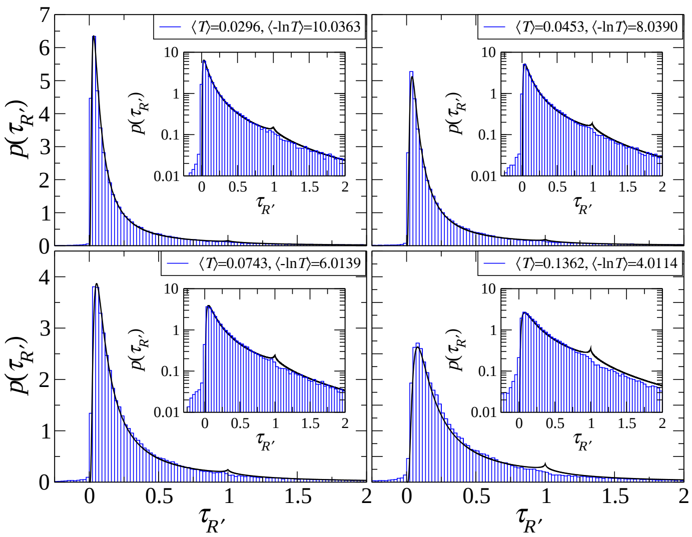

Figure C.18: The probability density function $p(\tau_{R'})$ for one-dimensional layered structures conformed by two different media, one inside another (histograms). The thickness of the layers is $l_b = 0.25$ cm while the distance between them is given by the absolute value of a Lévy random variable characterized by $\alpha = 3/4$ and $\beta = 0$. The parameters are $n_a = 1$, $n_b = \sqrt{4.4}$, $\nu = 7.5$ GHz and $\theta = 0$. Both, $\langle T \rangle$ and $\langle -\ln T \rangle$, are shown in each panel in order to identify the transport regime. The inset of each panel presents the same histogram of the main panel in semi-log scale. The solid black line is the theoretical prediction (3.6) with $p_s(\tau_R)$ the PDF (3.7) and $a = \alpha$. Each histogram was calculated using 10^5 ensemble realizations. A good agreement between theory and numerical simulation is observed. Here, we considered the change of variable $v_g \tau_{R'}/2L \Rightarrow \tau_{R'}$.

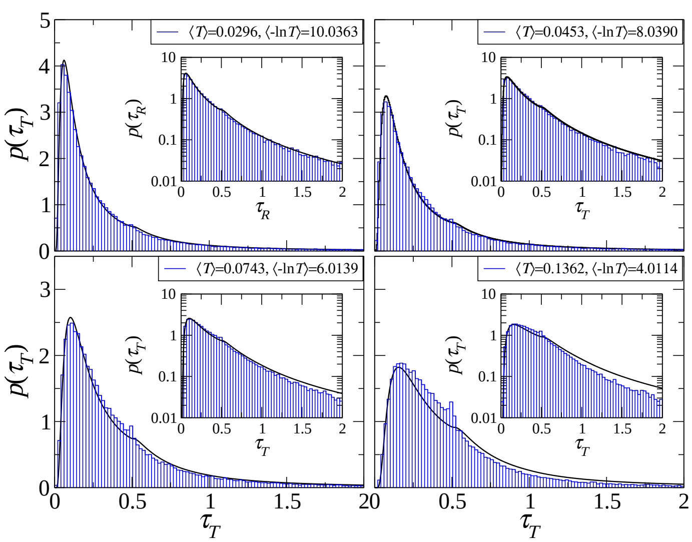

Figure C.19: The probability density function $p(\tau_T)$ for one-dimensional layered structures conformed by two different media, one inside another (histograms). The thickness of the layers is $l_b = 0.25$ cm while the distance between them is given by the absolute value of a Lévy random variable characterized by $\alpha = 3/4$ and $\beta = 0$. The parameters are $n_a = 1$, $n_b = \sqrt{4.4}$, $\nu = 7.5$ GHz and $\theta = 0$. Both, $\langle T \rangle$ and $\langle -\ln T \rangle$, are shown in each panel in order to identify the transport regime. The inset of each panel presents the same histogram of the main panel in semi-log scale. The solid black line is the theoretical prediction (2.12) with $p(\tau_R)$ and $p(\tau_{R'})$ the PDF (3.6) considering $p_s(\tau_R)$ and $p_s(\tau_{R'})$ as (3.7) and $a = \alpha$. Each histogram was calculated using 10^5 ensemble realizations. A good agreement between theory and numerical simulation is observed. Here, we considered the change of variable $v_g \tau_T/2L \Rightarrow \tau_T$.

Bibliography

[1] P. W. Anderson. Absence of diffusion in certain random lattices. *Phys. Rev.*, 109:1492–1505, 1958.

[2] E. Abrahams, P. W. Anderson, D. C. Licciardello, and T. V. Ramakrishnan. Scaling theory of localization: Absence of quantum diffusion in two dimensions. *Phys. Rev. Lett.*, 42:673–676, 1979.

[3] P. W. Anderson, D. J. Thouless, E. Abrahams, and D. S. Fisher. New method for a scaling theory of localization. *Phys. Rev. B*, 22:3519–3526, 1980.

[4] P. Barthelemy, J. Bertolotti, and D. S. Wiersma. A lévy flight for light. *Nature*, 453:495 EP –, 05 2008.

[5] R. Burioni, L. Caniparoli, and A. Vezzani. Lévy walks and scaling in quenched disordered media. *Phys. Rev. E*, 81:060101, 2010.

[6] F. Falceto and V. A. Gopar. Conductance through quantum wires with lévy-type disorder: Universal statistics in anomalous quantum transport. *EPL (Europhysics Letters)*, 92(5):57014, 2010.

[7] A. Eisfeld, S. M. Vlaming, V. A. Malyshev, and J. Knoester. Excitons in molecular aggregates with lévy-type disorder: Anomalous localization and exchange broadening of optical spectra. *Phys. Rev. Lett.*, 105:137402, 2010.

[8] A. A. Fernández-Marín, J. A. Méndez-Bermúdez, and V. A. Gopar. Photonic heterostructures with lévy-type disorder: Statistics of coherent transmission. *Phys. Rev. A*, 85:035803, 2012.

[9] I. Kleftogiannis, I. Amanatidis, and V. A. Gopar. Conductance through disordered graphene nanoribbons: Standard and anomalous electron localization. *Phys. Rev. B*, 88:205414, 2013.

[10] A. A. Fernández-Marín, J. A. Méndez-Bermúdez, J. Carbonell, F. Cervera, J. Sánchez-Dehesa, and V. A. Gopar. Beyond anderson localization in 1d: Anomalous localization of microwaves in random waveguides. *Phys. Rev. Lett.*, 113:233901, 2014.

[11] V. V. Uchaikin and V. M. Zolotarev. *Chance and Stability. Stable distributions and their applications.* Wiley, 1998.

[12] A. M. Reynolds and N. T. Ouellette. Swarm dynamics may give rise to lévy flights. *Scientific Reports*, 6:30515, 2016.

[13] R. N. Mantegna and H. E. Stanley. Scaling behaviour in the dynamics of an economic index. *Nature*, 376(6535):46–49, 1995.

[14] E. P. Wigner. Lower limit for the energy derivative of the scattering phase shift. *Phys. Rev.*, 98:145–147, 1955.

[15] A. Comtet and C. Texier. On the distribution of the wigner time delay in one-dimensional disordered systems. *Journal of Physics A: Mathematical and General*, 30(23):8017–8025, 1997.

[16] C. Texier and A. Comtet. Universality of the wigner time delay distribution for one-dimensional random potentials. *Phys. Rev. Lett.*, 82:4220–4223, May 1999.

[17] C. W. J. Beenakker. *Dynamics of localization in a waveguide*, pages 489–508. Springer Netherlands, 2001.

[18] H. Schomerus. Transmission delay times of localized waves. *Phys. Rev. E*, 64:026606, 2001.

[19] C. Texier. Wigner time delay and related concepts: Application to transport in coherent conductors. *Physica E: Low-dimensional Systems and Nanostructures*, 82:16–33, 2016.

[20] P. Markos and C. M. Soukoulis. *Wave Propagation: From Electrons to Photonic Crystals and Left-Handed Materials*. Princeton University Press, 2008.

[21] E. Merzbacher. *Quantum Mechanichs*. VSP, 1999.

[22] J. D. Jackson. *Classical electrodynamics*. Wiley, 3rd edition, 1999.

[23] F. T. Smith. Lifetime matrix in collision theory. *Phys. Rev.*, 119:2098–2098, 1960.

[24] P. Mello and N. Kumar. *Quantum Transport in Mesoscopic Systems: Complexity and Statistical Fluctuation*. Oxford University Press, 2004.

[25] V. I. Mel'kinov. Distribution of resistivity probabilities of a finite, disordered system. *Pis'ma Zh. Eksp. Teor. Fiz*, 32:259–262, 1980.

[26] V. I. Mel'kinov. The effect of the discrete nature of a finite disordered system on the distributionof resistances. *Pis'ma Zh. Eksp. Teor. Fiz*, 34:471–474, 1981.

[27] O. N. Dorokhov. Transmission coefficient and the localization length of an electron in n bound disordered chains. *Pis'ma Zh. Eksp. Teor. Fiz*, 36:259–262, 1982.

[28] C. W. J. Beenakker. Random-matrix theory of quantum transport. *Rev. Mod. Phys.*, 69:731–808, 1997.

[29] C. G. B. Garrett and D. E. McCumber. Propagation of a gaussian light pulse through an anomalous dispersion medium. *Phys. Rev. A*, 1:305–313, 1970.

[30] S. Chu and S. Wong. Linear pulse propagation in an absorbing medium. *Phys. Rev. Lett.*, 48:738–741, 1982.

[31] K. E. Oughstun and Constantinos M. Balictsis. Gaussian pulse propagation in a dispersive, absorbing dielectric. *Phys. Rev. Lett.*, 77:2210–2213, 1996.

[32] A. Comtet, C. Monthus, and M. Yor. Exponential functionals of brownian motion and disordered systems. *Journal of Applied Probability*, 35(2):255–271, 1998.

[33] C.W.J. Beenakker and P.W. Brouwer. Distribution of the reflection eigenvalues of a weakly absorbing chaotic cavity. *Physica E*, 9(3):463–466, 2001. Proceedings of an International Workshop and Seminar on the Dynamics of Complex Systems.

[34] A. Comtet and C. Monthus. Diffusion in a one-dimensional random medium and hyperbolic brownian motion. *Journal of Physics A: Mathematical and General*, 29(7):1331–1345, 1996.

[35] R. Pierrat, P. Ambichl, S. Gigan, A. Haber, R. Carminati, and S. Rotter. Invariance property of wave scattering through disordered media. *Proceedings of the National Academy of Sciences*, 111(50):17765–17770, 2014.

[36] C. W. J. Beenakker, J. C. J. Paasschens, and P. W. Brouwer. Probability of reflection by a random laser. *Phys. Rev. Lett.*, 76:1368–1371, 1996.

[37] G. E. P. Box and M. E. Muller. A note on the generation of random normal deviates. *Ann. Math. Statist.*, 29(2):610–611, 06 1958.

[38] C. W. J. Beenakker, C. W. Groth, and A. R. Akhmerov. Nonalgebraic length dependence of transmission through a chain of barriers with a lévy spacing distribution. *Phys. Rev. B*, 79:024204, 2009.

[39] T. Sh. Misirpashaev, J. C. J. Paasschens, and C. W. J. Beenakker. Localization in a disordered multi-mode waveguide with absorption or amplification. *Physica A*, 236:189–201, 1997.

[40] J. C. J. Paasschens, T. Sh. Misirpashaev, and C. W. J. Beenakker. Localization of light: Dual symmetry between absorption and amplification. *Phys. Rev. B*, 54:11887–11890, 1996.

[41] J. W. Goodman. *Statistical optics*. Wiley, 2000.

[42] B. A. van Tiggelen, P. Sebbah, M. Stoytchev, and A. Z. Genack. Delay-time statistics for diffuse waves. *Phys. Rev. E*, 59:7166–7172, 1999.

[43] H. Schomerus, K. J. H. van Bemmel, and C. W. J Beenakker. Coherent backscattering effect on wave dynamics in a random medium. *Europhysics Letters (EPL)*, 52(5):518–524, 2000.

[44] A. Z. Genack, P. Sebbah, M. Stoytchev, and B. A. van Tiggelen. Statistics of wave dynamics in random media. *Phys. Rev. Lett.*, 82:715–718, 1999.

BUAP

MEMORANDUM

Para:	**Dr. Luca Giuseppe Celardo, Presidente.** **Dr. Alfredo Díaz de Anda.** **Dr. Juan Mauricio Torres González.** **Dr. Víctor A. Gopar, Asesor. Vía Skype.**
De:	Dra. Antonio Méndez Blas, Secretario Académico.
Asunto:	Se cita al examen de grado de Maestría en Ciencias (Física) del Fís. Luis Alberto Razo López
Fecha:	10 de enero de 2020
Ccp	Dr. José Antonio Méndez Bermúdez, Asesor

Me permito informarles que el Comité Académico del IFUAP, los ha designado integrantes del Comité para el **EXAMEN DE GRADO DE MAESTRÍA EN CIENCIAS (FÍSICA)** de ***Fís. Luis Alberto Razo López,*** con su tesis titulada: ***"Propiedades de transporte en estructuras con desorden de Lévy",*** que presentará el próximo día: **Martes 14 de enero de 2020 a las 10:00 horas en el Auditorio del IFUAP.**

Dr. Antonio Méndez Blas
Secretario Académico

Instituto de Física
"Luis Rivera Terrazas"

Av. San Claudio esq. 18 sur, edif 110 A, B y C.
Ciudad Universitaria, Col. San Manuel,
Puebla, Pue. C.P. 72570
01(222) 2295610, Fax: ext. 5611

/LAEmhr